sCO2-4-NPP: Innovative sCO2-Based Heat Removal Technology for an Increased Level of Safety of Nuclear Power Plants

Deliverable 1.2

Report on the validation status of codes and models for simulation of sCO2-HeRo loop

Work programme topic addressed: NFRP-2018-10: Encouraging innovation in nuclear safety for the benefit of European citizen

Type of action: Innovation action

Grant Agreement number: 847606

Start date of project: 1 September 2019 Duration: 36 months

Lead beneficiary of this deliverable: USTUTT

Due date of deliverable: 31/05/2020 Actual submission date: 29/05/2020

Version #: R1.0

Type		
R	Document, report excluding the periodic and final reports	X
DEM	Demonstrator, pilot, prototype, plan designs	
DEC	Websites, patents filing, press & media actions, videos, etc.	
OTHER	Software, technical diagram, etc.	
Dissemination level		
PU	PUBLIC, fully open, e.g. web	X
CO	CONFIDENTIAL, restricted under conditions set out in Model Grant Agreement	

This project has received funding from the Euratom research and training programme 2014-2018 under grant agreement No 847606. This document and its contents remain the property of the beneficiaries of the sCO2-4-NPP Consortium and may not be distributed or reproduced without the express written approval of the Coordinator, EDF.

Revision History

Release	Date	Reason for Change	Author	Distribution
R0.1	21/05/2020	First Draft	USTUTT	All partners
R1.0	29/05/2020	Final version	USTUTT	Public
R1.1	19/08/2020	Figure 34 corrected	USTUTT	Public

Deliverable Contributors

Authors

Partner	Name
USTUTT	M.HOFER
USTUTT	M. BUCK
EDF	A. CAGNAC
EDF	T. PRUSEK
EDF	N. SOBECKI
CVR	P.VLCEK
CVR	D. KRIZ
GfS	F. HECKER
UDE	A. HACKS

Contributors

Partner	Name
EDF	F. DAVID

Internal Reviewers

Partner	Name
EDF	A. CAGNAC
USTUTT	J. STARFLINGER

Table of contents

List of Tables

List of Figures

1 List of Acronyms

Abbreviation / Acronym	Description / meaning
ATHLET	Analysis of THermalhydraulics of LEaks and Transients (system code of GRS)
CATHARE	Code for Analysis of Thermalhydraulics during an Accident of Reactor and safety Evaluation
CEA	Commisariat à l'énergie atomique et aux énergies alternatives
CHX	Compact Heat Exchanger
ClaRaPlus	Component library in Modelica
CV	Control Volume
CVR	Centrum výzkumu Řež
DN xx	Nominal Diameter (in mm)
Dymola	Dynamic modelling laboratory, modelling and simulation environment
EDF	Électricité de France SA, French utility
EOS	Equation of State
EXCEL	Microsoft© sheet calculation program
FFT	Fast Fourier Transformation (algorithm based on samples with 2^n data points)
FRAMATOME	France based NPP supplier
GCSM	General Control Simulation Module
GfS	Gesellschaft für Simulatorschulung (company)
GRS	Gesellschaft für Anlagen- und Reaktorsicherheit GbmH (German TSO)
HCO	Heat Conduction Object
HeRo	Heat Removal (labelling the loop in Essen from the sCO2-HeRo project)
IAEA	International Atomic Energy Agency
IKE	Institut für Kernenergetik und Energiesysteme
IRSN	Institut de Radioprotection et de Sûreté Nucléaire, expert organisation
MODELICA	Standardized object oriented modelling language
NCG	Non Condensable Gas
NEPTUNE CFD	Multiphase flows solver (CEA, EdF, Framatome and IRSN)

Abbreviation / Acronym	Description / meaning
NIST	National Institute of Standards and Technology (USA based)
NPP	Nuclear Power Plant
PP	Piston Pump
PV	Pressure Vessel
PWR	Pressurized Water Reactor
P&I	Piping and Instrumentation (diagram)
REFPROP	NIST Reference Fluid Thermodynamic and Transport Properties database
SBO	Station Black Out
sCO2	Supercritical carbon dioxide
SEH	Slave Electrical Heater
SWAGELOK	US based company, named after the leak tight fitting swage used
TAC	Turbo Alternating Compressor
TFO	Thermo-Fluiddynamic Object
THETIS	Code library for CATHARE
TRL	Technology Readiness Level
TS Media	Library in Modelica for thermodynamic properties
UDE	Universität Duisburg-Essen
UHS	Ultimate Heat Sink
USTUTT	Universität Stuttgart
3D-CAD	3-dimensional Computer Aided Design

2 Executive Summary

One of the main challenges of the sCO2-4-NPP project is to integrate the Heat Removal system (developed in the sCO2-HeRO project) into various thermal-hydraulic codes and to simulate its behaviour in case of an accidental situation on the nuclear power plant (NPP). The objective of the work presented in this report is to provide an overview of the development and validation status of each code (CATHARE, ATHLET, MODELICA) used in the sCO2-4-NPP project concerning the simulation of the sCO2-HeRo loop.

Therefore, this report first describes the experimental basis for the validation of the codes. This includes the description of the cycle as well as the components and the related challenges which need to be solved by the modellers. Since the cycle is operated close to the critical point and shows some interesting transient behaviour, e.g., mass flow rate oscillations, it is quite challenging to model the cycle. As a next step, the modelling status of the different codes is presented in terms of the whole cycle and single components. Due to the complexity of the turbomachinery modelling, it was decided to focus on the other components first. A cycle configuration including the piston pump and the heat exchangers was chosen for a blind benchmark test. Selected simulation results are presented showing some interesting characteristics of the modelled components, like the remarkable change in the air-side heat transfer coefficient at low fan speeds and the high sensitivity of the cycle to changes in the cooling power. The results of the benchmark simulations show that the different codes can catch the cycle behaviour with varying degrees of accuracy mainly due to the differences in development status of the codes. Thus, the test highlights the different challenges of modelling the small-scale HeRo cycle which are relevant to the large-scale heat removal system of the nuclear power plant, too. While some challenges were already solved within the scope of this deliverable, others are identified but require further investigation. By the validation of the simulations presented in this deliverable D1.2 the implementation of supercritical CO_2 in the codes ATHLET, CATHARE and MODELICA moved a big step ahead. Therefore, the confidence level for designing and simulating the heat removal cycle for the nuclear power plant is gradually increased and the goals of deliverable D1.2 are attained.

3 Introduction

One of the main challenges of the sCO2-4-NPP project is to integrate the Heat Removal system (developed in the sCO2-HeRo project) into various thermal-hydraulic codes and to simulate its behaviour in case of an accident in a nuclear power plant (NPP). Since supercritical CO_2 (sCO2) cycles are a novel technology, the application of sCO2 is new to this codes and validation against measurement data is required. The validated codes will be used to simulate the sCO2 heat removal system in combination with different actually working power plants and accident scenarios. The successful release of decay heat to the ultimate heat sink will proof that the sCO2 heat removal system is at TRL 5.

The scope of this deliverable is the validation of three thermal-hydraulic system codes (ATHLET, CATHARE and MODELICA) against measurement data from the HeRo cycle which was designed and built within the sCO2-HeRo project. The cycle is especially designed to experimentally investigate the concept of the sCO2-HeRo heat removal concept (Benra, et al., 2016). It was utilized to run several test cases and produce the measurements used in this deliverable. The HeRo cycle consist of three heat exchangers, a piston pump and a turbomachine as well as several other components. The three heat exchangers are a compact one connecting the CO_2 cycle to the steam cycle of the reactor glass model, an additional electrical heater and a plate-and-fin CO_2 to air heat exchanger. The flow can be either driven by the compressor or by the volumetric displacement pump of piston type. Normally, the turbine attached to the compressor allows to run the cycle without using additional electrical energy. Tests were performed in the cycle for various configurations. From all measurements a set of data for a certain configuration was chosen for a blind model benchmark. The configuration is extensively described in chapters 4 and 7.1. It represents a simplified cycle layout with circulation of CO_2 by the pump and heat transfer in the heater and cooler. This configuration allows effective validation of the three thermal-hydraulic system codes involved in this project. The HeRo cycle was modelled in all three codes according to specifications given by deliverable D1.1 and Hacks et al. (2019). Information related to the different components is supplemented by reports from the sCO2-HeRo project and related publications e.g. Strätz et al. (2018) and Vojáček et al. (2019). The results of a steady state simulation serve as a starting point to the blind benchmark test. The later relates to a transient case with an increase of cooling power. Comparing the model results with the experiments reveals the different challenges in the applied codes. Therefore, this deliverable not only reports about the current status of the different models but also discusses the future modelling steps and challenges.

In Chapter 4 the experimental basis is provided, including the cycle layout, the description of the components and the required correction of the measurement data. Chapter 5 gives an overview of the modelling approaches in the different codes. In Chapter 6 selected simulation results for components and the whole cycle are presented. Finally, in Chapter 7, the blind benchmark is described and conducted.

4 Experimental basis

The chapter on the experimental basis is separated into two parts. The first describes the HeRo loop and explains its general purpose and functionality. The description of the loop is to a large extent copied from the publication of Hacks et al. (2019). Another focus is the description of components and the challenges for modelling them. Further, Appendix B introduces the cycle layout represented by the piping and instrumentation diagram (P&I diagram). This P&I diagram is simplified to the configuration for the benchmark test in Figure 8 in chapter 4.2.6.

Secondly, section 4.3 explains the measurement uncertainties and required corrections of the measured data. Further, oscillations of fluid properties were observed during the tests and pose a challenge for simulations. They are analysed in section 4.3.6. The description of the benchmark experiment and the corresponding experimental results used for code validation are presented together with the simulation results in chapter 7.

4.1 Description of the sCO2-HeRo loop

The general description of the loop is based on the publication of Hacks et al. (2019). It provides a generalized description of sCO2-HeRo cycle function and layout. The sCO2-HeRo cycle is attached to the glass model according to the scheme in Figure 72 Appendix A with the components depicted in Figure 1. Here, in the 3D-CAD model on the left, the components of the glass model are coloured in grey and the components of the sCO2-HeRo cycle are marked with different colours. The height scheme on the right indicates the positions of the components on the three levels: the ground floor, the basement and the outdoor area. The corresponding detailed description of all components is provided chapter 4.2.

In case of postulated accident scenario with sCO2-HeRo operation, valve 1 (in Figure 72), connecting the steam generator of the glass model to the heat sink, is closed and valve 2 opens establishing a natural circulation driven cooling loop on the steam side of the PWR glass model. Driven by natural convection, the steam flows upwards into the compact heat exchanger (CHX, pink), where the heat is transferred to the sCO2 side by condensation heat transfer. The condensate can be observed in a glass tube depicted in shaded blue below the CHX in Figure 1. Through this tube, it flows downwards driven by gravity and re-enters the steam generator through the feedwater line, which results in continuous heat removal from the primary circuit via the u-tubes. In the sCO2-HeRo loop downstream of the CHX a slave electrical heater (SEH, red) is installed in the basement. It provides predetermined inlet conditions to the turbine and enables transient experiments and operation of the sCO2-HeRo loop in off-design conditions. Such flexible conditions allow for operation of the sCO2-cycle close to operation boundaries without any negative feedback effect to the glass model. Downstream of the SEH, the turbine of the turbomachine (TAC, green), which consists of turbine, alternator and compressor, expands the sCO2. It then flows outside into the gas coolers of the ultimate heat sink (UHS, light blue), from which it is delivered to the CHX by the compressor. In the design point of the system the turbine provides more power than required for the compression leading to a self-sustaining system with excess electricity at the alternator. In the nuclear power plant, this electricity will be used for the electrical driven fans of the UHS and for different kinds of auxiliary devices. Additional to the previously mentioned components, Figure 1 also contains the piston pump (PP, yellow) for circulation and leakage feedback and the pressure vessels, designed as piston accumulators, for the start-up procedure and compensating fluid expansion (PV, dark blue).

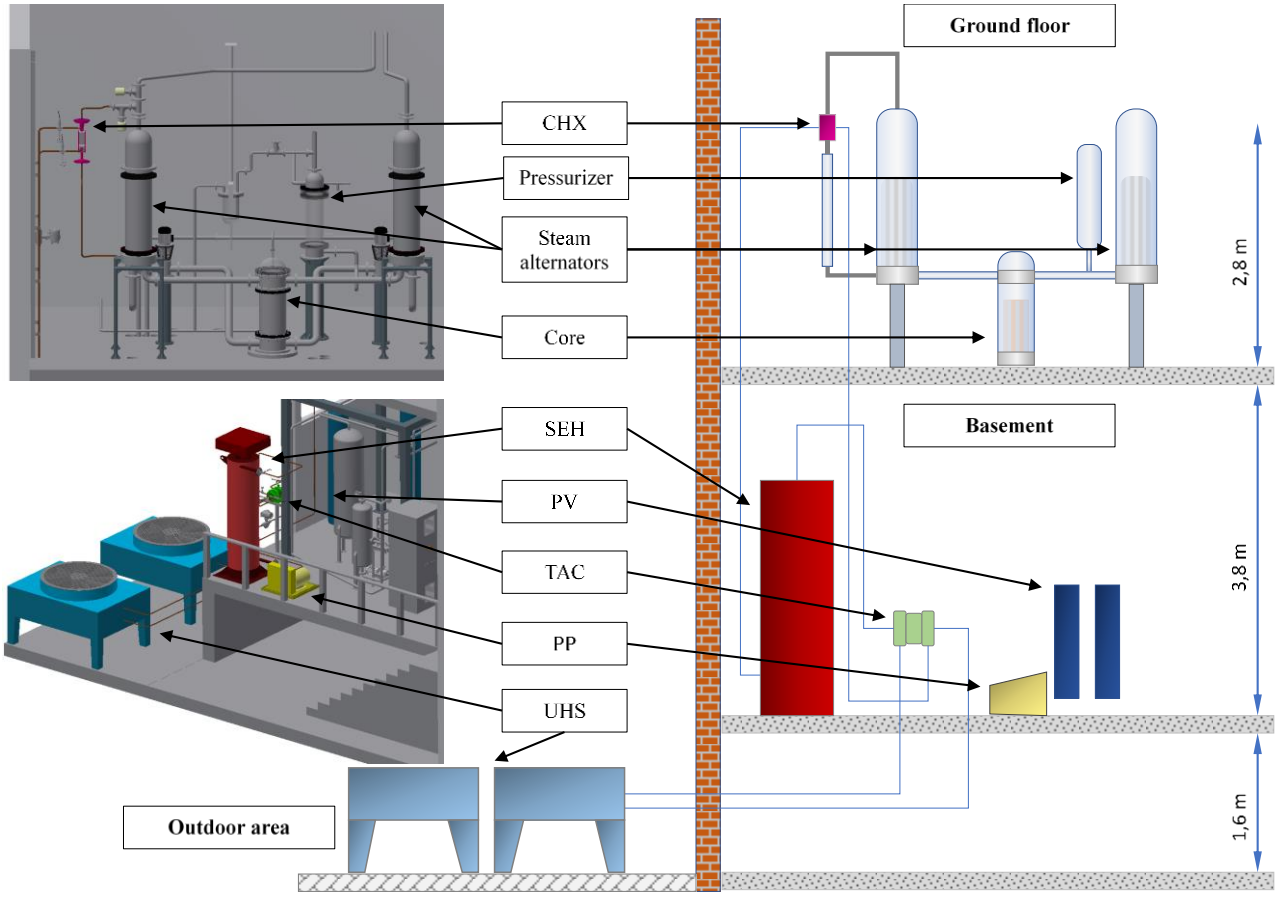

Figure 1 : CAD-Drawing and component position of the sCO2-HeRo cycle (Hacks, et al., 2019)

4.1.1 Piping and instrumentation diagram of the sCO2-HeRo cycle

The P&I diagram in Figure 73 in Appendix B represents the base of the cycle models. It includes all components of the main sCO2-HeRo system, components for start-up, as well as the measurements at each location. Furthermore, it can be divided into 8 sections, which are described in the following. Another reduced P&I diagram for the benchmark test is displayed and described in Figure 8 in chapter 4.2.6 about the piping.

Section 1 is marked with red (high pressure) and blue (low pressure) pipes and depicts the components of the main sCO2-HeRo cycle, like the compressor, CHX, SEH, turbine and UHS. Furthermore, temperature (T), pressure (p), density (ρ), load (M), revolution (n), vibration (f), voltage (U), current (I) and mass flow rate (F) measurement devices as well as different kind of valves are installed.

The region marked with number 2 shows the TAC system with the frequency converter as well as the PP. The TAC is the heart of the cycle as it is the component inducing the flow and thus transporting the decay heat from the core via the CHX to the UHS. Furthermore, the turbine produces the driving force for the compressor and for the alternator from the decay heat. Therefore, it makes the system self-sustaining. The frequency converter controls the mechanical load, the revolution speed, the excess electricity and the temperature at the alternator. To reduce friction losses at the alternator and to prevent any kind of damage in the bearings of the TAC, the PP independently reduces the pressure at the alternator and bearings by drawing a defined CO_2 leakage flow from the housing of the TAC. The leakage flow and pressure are adjusted by recirculating a part of the flow rate and adjusting the speed of the PP. Another purpose of the PP is the circulation of CO_2 in the cycle when the TAC is not used.

The SEH (in section 3) is required because the heat provided by the glass model via the CHX is insufficient to operate the sCO2-cycle at conditions of nuclear power plants. The heat input into the sCO2 is realized either as a constant electrical heating power or via a master slave control. Thus, the SEH allows a decoupling of the sCO2-HeRo cycle from the PWR glass model cycle for certain test cases because its heating power is sufficient to operate the sCO2 cycle without the CHX. On the other hand, in the master slave configuration, the heating power is adjusted according to the heat input from the compact heat exchanger.

The UHS is numbered with 4 in Figure 73. Since electrical driven fans support the heat removal to the UHS, voltage and current values can be adjusted and monitored to regulate the airflow and thus cooling power.

Section 5 shows the CHX. Measurement devices for measuring the pressure and temperature at the inlet and outlet of the CHX as well as for measuring the steam mass flow rate at the inlet of the CHX are installed. The two needle valves on the steam side of the CHX at the inlet and outlet are used for connecting or disconnecting the CHX from the glass model and regulating the steam flow.

The two PV are in Section 6. They are required for the sCO2-HeRo cycle to be able to start via a pressure surge. Additionally, PV II has the function of maintaining a constant compressor inlet pressure. It is assumed that in case of start-up procedure valves 2, 4, 15, 25, 28 and 29 are open. Then, valve 11 at the bottom of PV I will be opened, and due to the adjusted pressure difference between the main cycle and PV I, the inventory is forced to flow into the sCO2-HeRo cycle. With valve 6 closed, it is heated up in the CHX and SEH before entering the turbine, where it forces the shaft to start rotating. Following on the expansion in the turbine, it flows through the UHS and through in the lower chamber of PV II. After reaching the breakeven point, when the compressor outlet pressure exceeds the pressure in PV I and the turbine provides more power than needed for the compressor, the start-up procedure is finished by closing the compressor bypass valve 2 to open valve 6. Then, the sCO2-HeRo system is self-sustaining closed loop operation.

Before the entire sCO2-HeRo cycle can start operation, it has to be evacuated and filled with CO2. The vacuum pump unit for evacuation is numbered with 8 while the filling-unit consisting of a heated gas bottle and a valve is in section 7.

4.1.2 Piping and instrumentation diagram – Benchmark test

For the benchmark test, the TAC is excluded by closing valves TK01 S103, TK01 S201 and TK01 S403. This results in a simplified layout which is presented together with the description of components in the next chapter. Figure 8 in section 4.2.6 presents the simplified P&I diagram.

4.2 Description of components for the benchmark test

The specifications of the components in the cycle, given in this section, define the capabilities of the sCO2-HeRo cycle. The descriptions and main parameters are also available in the publication of Hacks et al. (Hacks, et al., 2019). Here, only components required for the benchmark test (see chapter 7) are shown. For the description of the TAC please refer to the paper of Hacks et al. (Hacks, et al., 2019). The descriptions in the paper are complemented by knowledge from testing in the HeRo cycle regarding both geometry and challenges for modelling in general. Other detailed information regarding design and testing of the components can be found in the referenced papers.

4.2.1 Compact heat exchanger (CHX)

The compact heat exchanger, manufactured by the Institute of Nuclear Technology and Energy Systems (IKE) at the University of Stuttgart, provides heat transfer from steam to CO_2. It is connected to the steam generator of the glass model as presented in Figure 2. No heat transfer occurred in the benchmark test described in chapter7. But its pressure drop has to be modelled. Detailed descriptions on the CHX design and experimental investigations of the heat transfer and pressure losses are presented by Strätz et al. (2017) and Strätz et al. (2018) .

Figure 2 : Compact heat exchanger with pressure and temperature sensors

The CHX consists of several plates with milled channels stacked on each other. There is an inlet chamber and an outlet chamber, distributing and collecting the CO_2 to and from the 210 channels of 1 mm x 2 mm cross section. The length of each channel is about 221.6 mm. The channels have Z-shape and thus there are 2 rectangular corners in the flow path.

With the larger inlet and outlet chamber and a total channel cross section of 4.2 cm², the flow speed in the CHX will be reduced compared to the lines.

4.2.2 Slave Electrical Heater (SEH)

The SEH is a tubular heater, manufactured by ELMESS, with a rated electrical power of 240 kW. The heating tube elements are grouped in a vertical cylinder near the central axis, casted in aluminium. The aluminium provides the heat transfer to a noble steel coil with 29 ½ windings, an outer pipe diameter of 60.3 mm and a wall thickness of 5.54 mm. The distance of the windings is 71 mm between the centre axis of the pipe. The distance of about 1 cm in between the pipes' surfaces allows heat flux through the aluminium towards the outer side of the coil. Total length of the winded part is about 46.5 m. Straight end joints at both ends have 60

cm each. The heating power can be controlled in small steps. The percentage value for the controller is proportional to 240 kW.

The insulation, visible in Figure 3**,** prevents heat losses, which in consequence can be neglected.

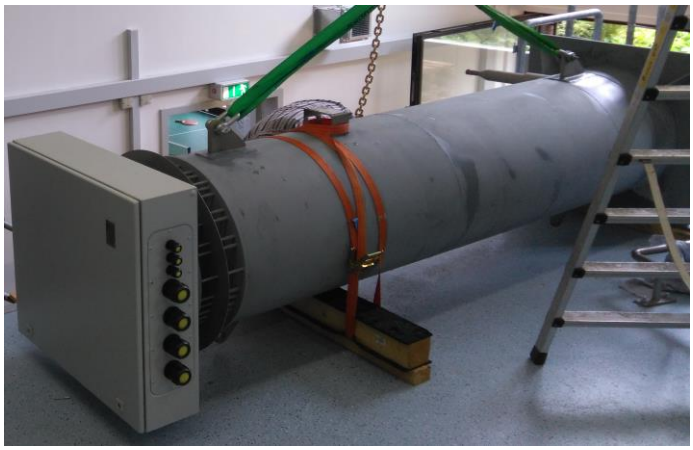

Figure 3 : SEH with (right) and without insulation and aluminium cast visible (left)

The pipe cross section is about 6 ½ times the cross section of the general pipe work, so the flow velocity will reduce on entering the SEH. At subcritical conditions some phase separation is to be expected in the slightly sloped pipes along the helix. Gaseous phase will flow with higher speed. This phase slip makes it complicated to calculate the mass stored in the SEH and to reproduce the correct phase mixture and enthalpy at the outlet of SEH. This effect is well known for water steam systems and is regularly demonstrated at the glass model in Essen. If overheating is reached at the outlet the problem shifts to the length of the “wetted” pipe section, because heat transfer is improved by phase change, and hampered from dry out. Therefore the phase slip will result in a deviation for the presence of liquid at the heating surface from a simple mixture assumption based on enthalpy balance. The wetted pipe section may be significantly shorter than expected, with the denser liquid phase collecting at the bottom of the heated coil.

Therefore, heat transfer will be better from metal to fluid at the bottom, especially if the fluid temperature reaches saturation point and phase change improves the heat transfer. From this, a much smaller temperature span is needed to provide the heat flux density there.

If heat flux from electrical heating coils is assumed to be uniform along the axis of the aluminium cast cylinder, the temperature along that axis will develop a distinct profile, with higher temperature on top, with a clear

difference to the “dried” fluid temperature, whereas this difference will be smaller in the “wetted” region. The contribution to the profile from heat transfer conditions comes on top to the temperature profile of the fluid itself along flow path from inlet to outlet.

The temperature profile in the aluminium cast will be smoothed by heat conduction along the axial direction of the aluminium cast cylinder.

As a consequence of the axial profile of temperature, the temperature on top of the pipe in a winding will be higher than at the bottom, e.g. for a total temperature span of 15 K the average difference for a winding will be about 0.5 K. Furthermore, temperature at inlet will be higher than at the outside, from the quite narrow aluminium bridges of less than 1 cm between the windings. With phase separation between top and bottom, and with centrifugal force driving the denser phase to the outside flowing through the helix, separation related effects will be amplified by temperature profile, keeping the gaseous phase in slightly overheated, unless there is some mixing along the cross section of the two phase flow.

Such a mixing will be forced by increase of flow speed at the inlet of the SEH. This can be enabled by an increased mass flow, e.g. changing PP mass flow by PP inlet density, or density decrease with the same mass flow, e.g. from changed thermodynamic parameters at the UHS outlet. The increase of flow speed will push forward the saturated liquid phase into regions of hotter wall temperature. This is especially pronounced if liquid comes forward into formerly dried out sections of the helix. The increase in volume from boiling will increase flow speed at the outlet further. By throttling or capacity limit of the PP, a pressure surge will occur. Calculated from inlet and outlet conditions, more enthalpy transfer would be obtained compared to the electrical heating balance. This gain in enthalpy is real, because it is fed from the heat stored in the aluminium of the heater. From this, such a “boil up” will be seen from thermodynamic parameters in the whole CO2-Loop. With respect to the length of the helix, the effect can be stretched over several minutes, while the windings are slowly filled with denser fluid, cooling down the aluminium cast along the vertical axis of the cylinder, shifting the temperature profile towards the top.

In supercritical fluid the shift in heat transfer conditions from density will be pronounced to a lesser extent. Nevertheless, operating near the critical point means to have well pronounced density changes for comparably small temperature differences, as characterised above in the two-phase mode as the reason for separation in between high enthalpy gas and low enthalpy fluid. From this, deviations in outlet conditions against homogeneous assumptions regarding specific enthalpy and temperature, as well as long term oscillations could be explained.

4.2.3 Ultimate Heat Sink (UHS)

There are two units of air cooled heat sink (type No. GGHV CD 090.1QF/11E-31) at the sCO2-HeRo-Loop in Essen, manufactured by Güntner GmbH & Co. KG. Figure 4 displays both units and the related piping which is closely described in section 4.2.6. For each unit the finned pipes are mounted into a rectangular box with about 1.4 m x 2.2 m inner side length. The cooling package has a thickness of about 15 cm, where the box height has 52 cm. The tube pitch in the package is 50 mm x 25 mm. The pipes have got an outer diameter of 12 mm and a wall thickness of 1 mm. For each unit there are 2 strains, each consisting of 4 parallel pipes. Each pipe is divided in 32 consecutive sections, finned over the length of 1.4 m inside the box. The tubes are connected outside by welding with short bends. Such a connection outside (without fins) has a length of about 20 cm. More detailed description of the geometry is provided by Vojáček et al. (2019).

Fluid side

Summing up the pipes, headers and collectors, a total volume results on CO2-side of about 17 l per strain, meaning 68 l for both units together. Total length of each of the 16 pipes between header and collector is about *L*= 51 m.

A certain time delay has to be considered for the response at the outlet to a change of a thermal parameter like density or heat capacity at the inlet.

Pressure changes in contrast will act almost immediately with speed of sound. So considering speed of sound *c* in CO_2 of about 175 - 200 m/s near critical point, the travel time of pressure fluctuations is about a quarter of a second. For wave propagation the first natural-frequency *f* for a wave number k = ½ will be about 1.24 Hz.

$$f = \frac{c}{\pi\, L} = \frac{200\,\frac{m}{s}}{3{,}14 * 51\ m} \approx 1.24\ Hz \tag{1}$$

From this, the space in the heat sink has the potential for some resonance in higher harmonics to a PP frequency of 3 *3.6 Hz (at 600 rpm motor speed). On the other hand, the volume of the heat sink was considered sufficiently large to buffer the strokes of the PP and to damp the waves by dissipation of energy in the phase mixture and supercritical fluid.

Figure 4 : Piping at the UHS

Air side

The fin pitch is 2.4 mm, with fin thickness of about 0.5 mm (Figure 5). There is some profiling from manufacturing, for stability reasons and fluid mixing, so the thickness at the edge is visibly smaller.

Figure 5 : Pipes and fins inside the UHS

The total heat exchange surface for one of two strains per unit is given with 180.4 m², so 721.6 m² (4 x 180.4 m²) is the total heat transfer surface for both units.

The stainless steel pipes are stuck through the aluminium fin plates, with a base at the fin ring. The distance between plates is kept by thin aluminium rings with a joint to the fins, this way connecting the tube surface between fin bases with the fin plate. These rings slightly increase the effective outer diameter of the pipe section in between the fins.

The characteristics of the air flow can be assumed to be in between cross flow and counter flow principle. The pipe sections are divided into 6 levels, each having 5 or 6 sections lined up. Hottest level is on top, coolest at the bottom. The air flow enters from below, leaving the cooler package on top. Thus, the order of 6 levels top down against the air flow provides the counter flow, whereas in each single level there is cross flow.

The heated air is being collected at the suction side of the 900 mm diameter fan. The air flow pattern in between the fins is laminar and may be considerably influenced by natural convection at very low fan speed.

Balancing the density in the UHS is crucial for mass balance and thus pressure control in the cycle. Therefore, the speed of the fans can be controlled between 10 % and 100 %, with full speed at 560 rpm. Some basic properties, e.g. air flow, were investigated during the sCO2-HeRo project by Vojáček et al., (2019). From this, the volume flow at 100 % is about 3.9 m³/s. Some linear characteristics may be assumed, confirmed by measurements at 75% and 50% of full speed. However, the linear characteristics have to be discussed for slow fan speed, because the effects of natural convection will have a significant role.

4.2.4 Piston pump (PP)

The PP is of the type P72/225-80 III and supplied by Speck-Triplex-Pumpen GmbH & Co. KG (Figure 6). It has a design power of 3.8 kW at a flow rate of 120 l/min. It provides the driving force for the circulation in the benchmark test.

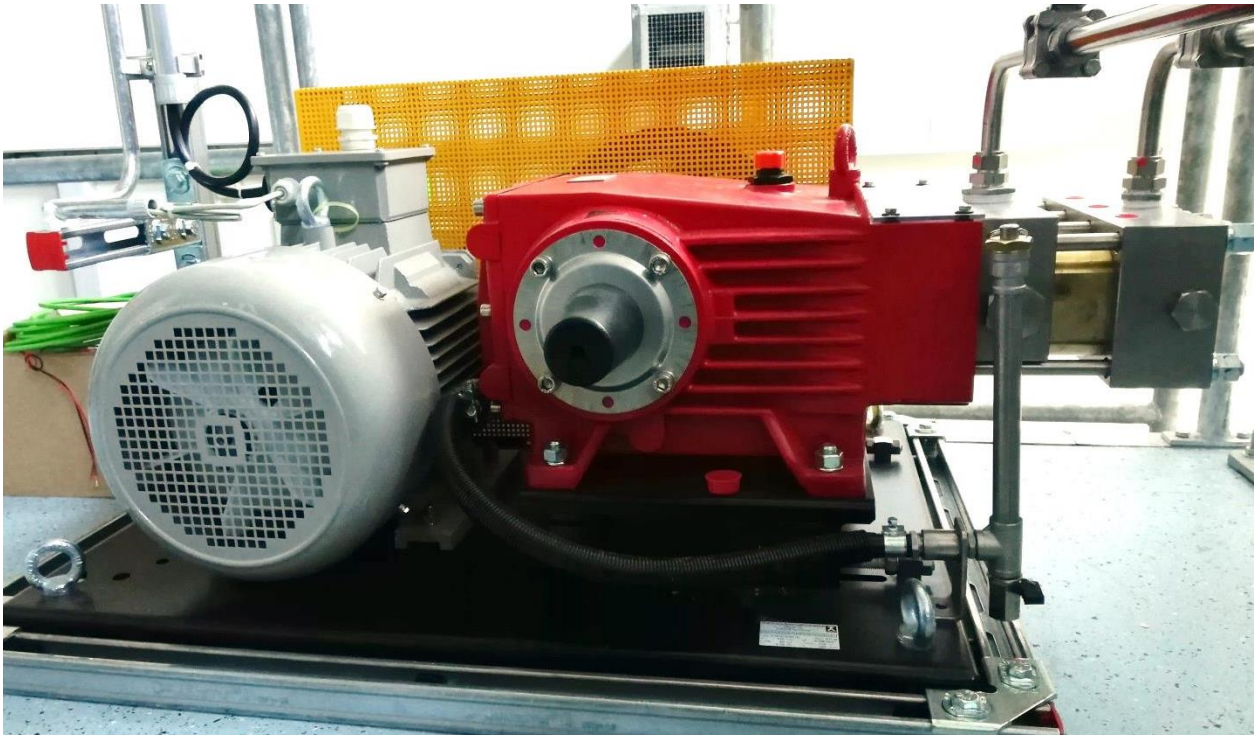

Figure 6 : Piston Pump (PP)

Under operation conditions, the pump is needed to keep the casing and bearings of turbo alternating compressor (TAC) on subcritical pressure during operation. Flow is controlled by the speed of the motor from a frequency converter. During the reference case, the speed of the motor was adjusted to 600 rpm of 720 rpm (about 83%). Via the belt gear pump rotational speed was reduced from 260 rpm (according to 720 rpm motor speed) to 217 rpm respectively. A rated speed of 83 % means 3.6 rounds per second or 10.8 piston strokes per second.

As generally valid for a PP, pressure head will be determined by pressure losses and counteracting pressure from the system. So the volume flow is the relevant parameter to describe the pump, with pressure difference contributing to the enthalpy transferred to the fluid. For a volume flow of about 1.6 l/s with an adiabatic pressure gain of 18 bar a power influx of about 3 kW has to be taken into account.

Mass flow is mainly determined by density and compressibility of the fluid. The flow at full speed is given as 2 l/s for “cold water”, referring the piston motion. This number neglects compressibility of the fluid and any dead space in the piston chamber (Figure 7). With changing density at the inlet, the mass flow will follow in proportion to the density.

Figure 7 : View into the open piston chamber of the triplex pump

Further considerations have to be accounted for in modelling:

- Throttling the supercritical CO_2 via valve 24 (TK02 S104) to subcritical conditions at the suction side of the pump, which comes from the pump's purpose, will decrease density and increase volume flow. Pressure drop to the pump inlet will add. Density and pressure will have to be calculated from conditions before throttling and assuming a thermodynamic process, e.g. isenthalpic throttling, to estimate the conditions at the pump inlet.
- With the density known, simply multiplying with the volume movement of the pistons will lead to systematic overestimation, because the compressible, expanding CO_2 from the dead space (which size is not known) will already fill a part of the piston chamber, before the fluid from suction side can flow in. This effect is proportional to the dead space size. Hence a discount on the expected volume flow has to be considered. Keeping the circuit closed, with no bypass for the referred situation (e.g. via TK02 S105), the mass flow through the flow meter before CHX can be used to estimate this discount. Minor losses can be considered through leakage along the piston rings. These would be covered by the discount from dead space too.

4.2.5 Pressure vessel (PV)

The two piston accumulators are supplied by Roth Hydraulics GmbH. The product number is AK 100-220-36. They have a nominal volume of 100 l of CO_2 each, with a design pressure of 220 bar. A piston accumulator consists of two chambers inside a cylinder, separated from each other by a sliding piston with here 360 mm diameter. Two piston accumulators are attached to the sCO2-HeRo loop, one for the high-pressure part and one for the low-pressure part. They are intended to buffer pressure and density changes during operation of the loop, as well to be a possible start up option. For the described benchmark test, the minimum pressure of PV 1 is kept above 90 bar while PV 2 was filled with nitrogen to come into action at slightly above 70 bar. Unfortunately, there is no position indicator of the piston. Therefore its actual position and the enclosed CO_2 volume in the pressure vessels is not recorded. The piston behaviour is modelled using ideal gas laws for the N_2 gas buffer over the piston, the initial assumption is adiabatic, later becoming isothermal. The initial pressure

can be observed from change of temperature from ambient room temperature towards fluid temperature at the PV inlet (meaning that CO_2 from the cycle flows into the PV). This was used to check the influence of the PV to former transients and during start up for the benchmark data, and a pressure of 72.3 bar (absolute) was identified. With a pressure up to 81 bar, a total volume of 7.1 l in adiabatic case will be stored. In isothermal case it will be about 10.6 l. With the density of about 550 kg/m³, a mass of 3.9 to 5.8 kg could be stored over time. During short term transient, only a fraction of these will be activated. For benchmark conditions, i.e. for transient in between 80 to 75 bar, the influence from adiabatic compression or expansion is expected to be about 3.8 l (2 kg), so it may be neglected, being only 3 % of the total mass of 65 to 70 kg of CO_2 in the whole cycle.

4.2.6 Piping & instrumentation

The piping for the circulation cycle used in the benchmark test is described in this section. Figure 8 presents a simplified P&I diagram for this test case. It strongly reduces the complexity of the HeRo-cycle by reducing the number of components involved and refers to category 1 validation approach proposed in deliverable D1.1.

Pipework is made from SWAGELOK noble steel pipes, with an outer diameter of ¾ inches (1.91 cm) and a wall thickness of 1.6 mm. Hence an inner diameter of 1.59 cm results, with a cross section area of 1.97 cm².

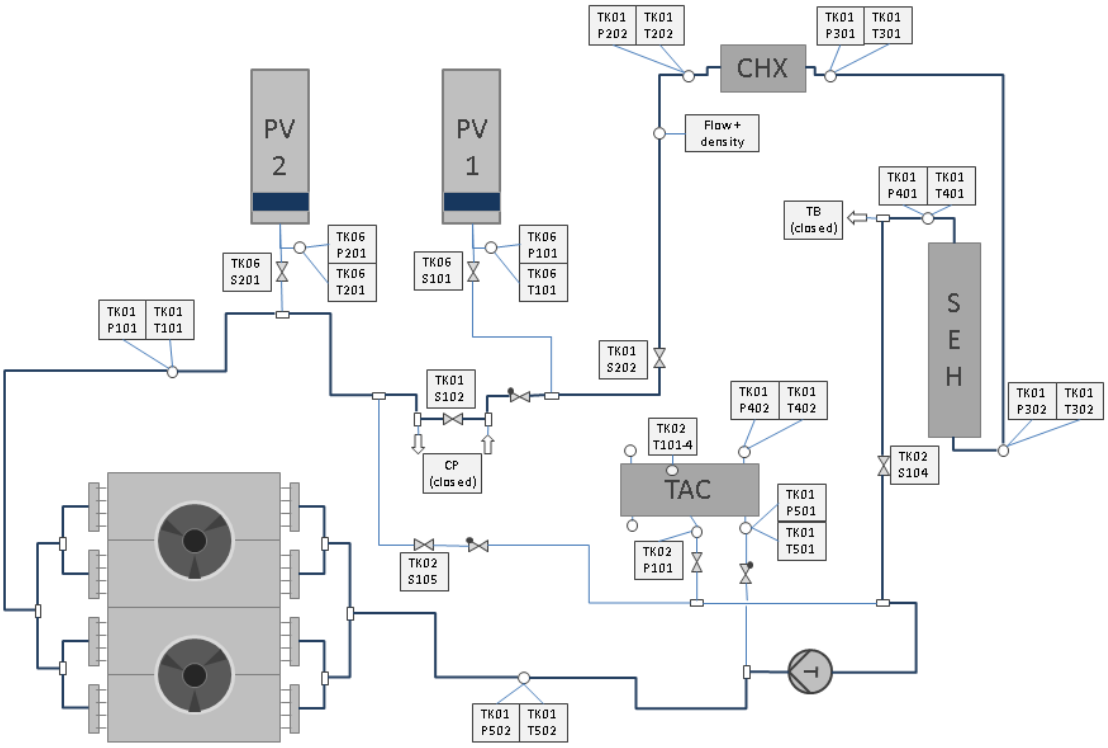

Figure 8 : P&I diagram – Benchmark test

As a general rule, the number of elbow fittings were minimized in the cycle because of their loss factors; the only ones used connect the pipes to the CHX. However, T-junctions were used for branches, e.g. in the flow path bypassing the compressor, increasing the flow resistance. Further T-junctions were used for flow distribution and collection before and after the UHS. Other bends with a larger radius only contribute to overall

pressure loss with moderate loss factors. Because of their length, straight pipes will contribute to pressure losses in turbulent flow.

Each code has its library to calculate the losses according to proven models and correlations. With the flow path modelled, varying some parameters like surface roughness may be used to reproduce the data obtained from experiment. For this the knowledge of the flow path is needed as a base. This data was provided in the sCO2-HeRo project and updated during the project.

From this, the relevant flow path for the benchmark test can be described between the inlet measurement of UHS, TK01 P502/T502 and SEH outlet, TK01 P401/T401 as follows:

From TK01 P502/ T502 to pressure and temperature sensors TK01 P101/ T101 the connection is as follows:

- A short pipe goes to a 90 ° bow outside the building, continuing to branch with a T-junction into 2 lines to both UHS. Length of the pipe up to the T-junction is 165 cm. From this, the flow path can be taken symmetrically:
    - From T-junction to a T-junction branch into first UHS section: Pipe length 55 cm.
        - This branch enters the header at the UHS after about 50 cm
        - Second branch goes into the other header after a wide 90 ° bend and has a length of 195 cm.
        - Length of each header is 90 cm. Its inner diameter is about 2.5 cm. 4 branches from each header enter the UHS.
            - Each of these 4 branches consists of 32 straight tube sections with U-bends at the end. The inner diameter 1 cm and total length of the tubes is about 51 m.
        - At the outlet, each collector unites 4 branches from UHS. Its size matches the previously described header.
        - Two pipes from the collectors join another T-junction behind one unit of the UHS. The first pipe has a length of 238 cm and 2 wide 90° bends. The second has one bend and about 60 cm length.
    - The flow through both units joins after another 55 cm of pipe in another T-junction
- About 375 cm of pipe with 3 wide 90° bends connect the T-junction with the measurement position of TK01 T101 and P101.

This first section is considered “the UHS”, because all data known for pressure drop, inlet and outlet temperatures result from the measuring TK01 P/T 502 and TK01 P/T 101.

From TK01 T101 the line goes in a 90° bend upwards, after 20 cm it passes the T-junction branch to the UHS bypass in a straight line.

Passing the T-junction to PV2 in a straight line, after about 95 cm and a 90 ° bend the T-junction to the compressor bypass with valve TK01 S102 comes (Figure 9). Here the flow takes the sharp curve, goes through the (fully open) needle valve TK01 S102 and via a T-junction from the side back into the main flow. Inlet and outlet of the manual needle valve are connected to the T-junctions with short pipes of about 15 cm.

Figure 9 : Piping at compressor bypass

After about 40 cm and a 90 ° bend the check valve TK01 S204 is passed. Now some information about pressure is available from the branch to PV1, TK06 P101.

With a 45 ° bow, the pipe goes after 30 cm into (fully open) needle valve TK01 S202.

From there, the pipe goes straight upwards for 340 cm to the Coriolis meter in the glass model room.

From the Coriolis meter, a pipe with 140 cm length and a 90° bow goes to TK01 T202.

After a 40 cm section with a small hosepipe and a sharp 90° bend, the flow goes into the CHX.

After CHX, a similar configuration (sharp bend, hosepipe, 40 cm) leads to TK01 T301.

Now the flow goes directly downwards to the machine room to the SEH inlet. Length of pipe is about 860 cm, and five 90° bends are on the way, before it comes to TK01 P302/ T302. With a further 90° bend and about 50 cm it goes directly into the SEH.

The SEH itself is a coil of about 46.5 m length in 29 ½ windings, with 71 mm step size, with an inner diameter of 49.22 mm and two end joints of 60 cm each.

Directly after SEH, after 10 cm, the outlet temperature measuring TK01 T401 with pressure TK01 P401 follows.

This is the path for the supercritical fluid during benchmark calculation.

To close the cycle, the pump needs the flow from the SEH outlet to its suction side from the sideway of a T-junction, down to the needle valve TK02 S104, with 180 cm pipe length.

After TK02 S104, with a 90 ° bow and a T-junction, where the line from TAC casing and UHS bypass comes in, the flow goes via two 90° bends to the suction side of the PP. Pipe length for this is about 205 cm.

After PP, the flow goes for about 250 cm via two 90° bends, the sharp bend of a T-junction and another 90° bend, now in the main line from the turbine, to TK01 P502/ T502. So the cycle is closed.

4.2.7 Needle Valves, Check Valve

The characteristics of needle valves were investigated for Deliverable 1.1. The supplier SWAGELOK gives a linear characteristics from 0 to 5 rounds opening of Kv = 0 to 1.57, valid for cold incompressible fluids, which the conical valve piston and seat are designed for. Because of different properties, as viscosity and compressibility, a different characteristic was expected and obtained for CO_2. Figure 10 shows the measured characteristic with a rapid increase of Kv at lower valve positions and slightly higher Kv at 100 % opening compared to the suppliers value (here: 100 % open = 5 rounds open). The fully open position for the valve used varies between 6 and 6.25 rounds.

For benchmark testing, a number of valves could be left in open position. Only TK02 S104 had been throttled to about 13% of the fully open position of 6.25 rounds. The position had to be taken by vision of the angle of the handle compared to the closed position. It has to be noted that at the throttled position the flow reacts sensitively to the slightest change of valve position.

In order to adapt the Kv value to a corresponding value for ζ in a pipe network with a given pipe cross section area (given as A = 1.97 cm² for the pipes described above) the following formula is used:

$$\zeta = \frac{2\,A^2 * 3.6^2}{K_v^2 *\ 10^{-8}\,m^4} \tag{2}$$

From this, for a check valve with Kv = 4.07 (given from the supplier SWAGELOK), ζ ≈ 6.1 is obtained.

For a fully open needle valve with Kv ≈ 1.9, the corresponding ζ≈ 28 results. The original value Kv = 1.57 from the supplier would result in ζ≈ 41.

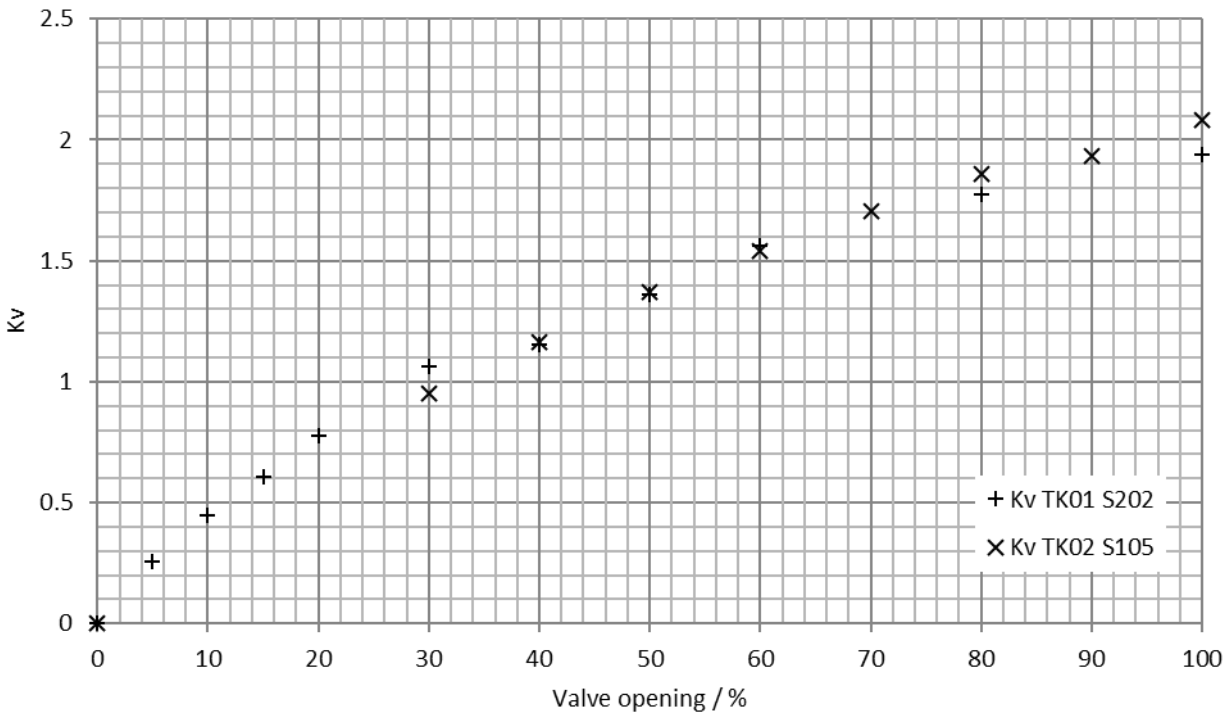

Figure 10 : Measured characteristics of the needle valves (from D1.1)

Finally, a value for the throttled TK02 S104 will be about ζ≈ 332 (from Kv ≈ 0.55), but even slightest error in position or characteristics assumed would result in ζ≈ 280 (from Kv ≈ 0.6) or ζ≈ 402 (from Kv ≈ 0.5) as visible in Figure 10.

4.3 Measurement data correction

4.3.1 Temperature sensors

Platinum resistance thermometers are used for temperature measuring. The Class A sensors have a normed preciseness of fractures of Kelvin in the range of interest, and the 3 wire configuration compensates for resistance of the signal cable. This preciseness is not supported by the rest of the measuring process. The Analog Input card SM331 gives an overall preciseness of 0.6% of operable range during use for processing of the resistance thermometers signal. Range goes from -50 °C to 250 °C, so deviation can be expected to be up to 1.8 K.

For some temperature measurements in the direct flow line, a simple method could be applied to get some calibration in the field: the measured temperature was compared to the saturated temperature at the valid pressure, when two-phase fluid was circulated through the loop. This is demonstrated as an example for TK01 T401 in Figure 11. The grey line describes the difference from temperature measured to saturated temperature, with values on the right hand side axis. Reaching saturation from formerly overheated, gaseous state, temperature difference is to be expected zero, hence the remaining difference gives the bias. Further on the right hand side, a regular change between overheated and saturated conditions can be seen, with about 4 min distance between 2 peaks. This may support the explanation about phase effects in the SEH. (see chapter 4.2.2)

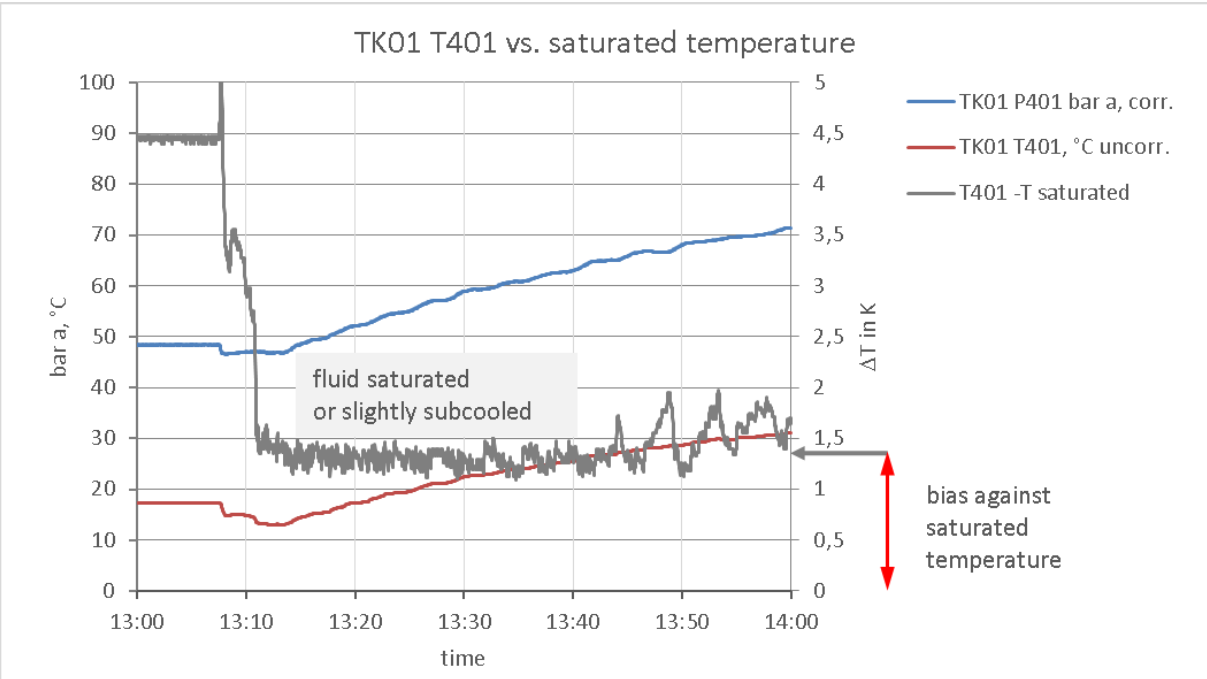

Figure 11 : Example for correction of temperature against saturation

Preciseness of the pressure sensors was taken into account, but was of little importance for the intended preciseness. So a constant bias was obtained for all temperature sensors relevant for benchmark testing. The data were collected and published already for D1.1, but verified and completed from an additional run the day

before the run for benchmark data. So for discussion, the temperature will already be corrected by value given in Table 1, if not stated otherwise.

Table 1: Bias of temperature measurement from saturation point

Temperature Sensor	Location	Bias in K
TK01 T101	after UHS	1.4
TK01 T202	before CHX	1.17
TK01 T301	after CHX	1.3
TK01 T302	before SEH	1.45
TK01 T401	after SEH	1.35
TK01 T502	before UHS	0.19
TK04 T201	inlet UHS, Air	0.7 -1.3
Correction: Subtract bias from measured value		

4.3.2 Flow and density measurement

Two Coriolis type flow meters are used, PromassFP (CNGmass DCI) from Endress&Hauser. In industry, theses transmitters are designed for the use with natural gas. A mass flow between 0-1.33 kg/s can be measured in the DN15 lines. By measuring principle from phase shift between oscillations in between the two branches of the device, mass flow is measured independently from density. The flow meters are also used to measure the density, which is especially important at the compressor inlet, which is close to the critical point, because determining the fluid properties via REFPROP is less prone to density uncertainties than temperature uncertainties. Precision relies on calibration. Deviation from calibrated values is given with 0.5 %.

For benchmark test, only the Coriolis measurement before CHX is in the flow path, labelled TK01 M201 for density and TK01 F201 for mass flow. No correction was used, because there was no indication of bias.

4.3.3 Pressure sensors

Piezo resistive sensors are used for pressure measurements at the sCO2-loop. The overall preciseness given by the vendor is 0.5 % of the range of 0…160 bar. From this a deviation of +/- 0.8 bar results. As marked early during first experiments at the loop, and as generally stated from various suppliers, this does not cover the deviation coming from temperature influence at the sensor, which could be handled by several ways:

- For many processes, there is only little change in temperature, so a simple calibration to typical ambient temperature may hold. For this purpose sensors are offered, limited to about 85 °C fluid temperature, due to stress to the measuring membrane and the electronics in the head of the sensor.
- Processes with higher temperatures need a separation from fluid and membrane, mostly done with a hydraulic fluid in a surface cooled coil.
- For temperature stability, the influence of temperature on the resistors in the Wheatstone bridge will be compensated to a certain extent with an electronic circuit.

- For high quality measurements there may be a protocol for calibration with a quite sophisticated profile with polynomial approximation.

Establishing the sCO_2 Loop during sCO2-HeRo project, the sensors were purchased from a vendor, who was not a supplier for these sensors himself. So limited information is available about the characteristics. Two classes of sensors were ordered, following the temperature expected in the fluid:

- Short shafted budget sensors with limited temperature range for systems sections with temperatures well below 80 °C. These sensors are prone to deviation from temperature influence and show up no compensation.
- Long shafted pricier sensors with a temperature range up to 250 °C and, obviously from data, some temperature compensation.

For D1.1, the quality of the sensors was assessed, and the sensors at TK01 P302/ P401/ P402/ P501/ P502 and TK02 P101 were found to be reliable, with some constant bias for the latter.

Whereas there was a need to find some compensation method regarding the budget sensors for the evaluation of pressure drop over components and pipes for D1.1, the assessment of benchmark calculation in D1.2 could be executed based at the set of reliable pressure sensors. So the resistance ζ of the loop from UHS inlet to SEH inlet can be reproduced from TK01 P502 and TK02 P302, confirming a calculated value from analysis of valves, pipes, fittings and bends of about $\zeta \approx 130$ in the supercritical region.

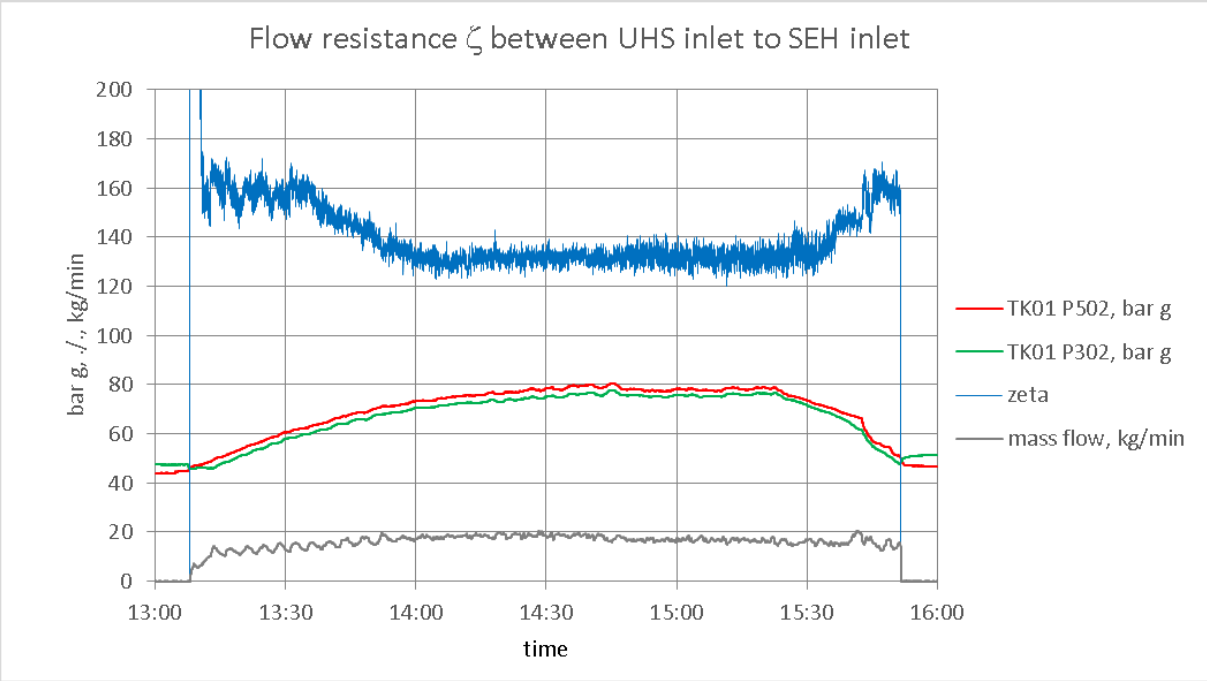

Figure 12 : Example for a result from reliable class of pressure sensors

As a result of D1.1, the pressure drop over UHS, CHX and SEH was found to vanish within the error margins, even if the signal stability for statistical error is typically 0.05 % (1 σ) of the range. Thus, the pressure signal typically fluctuates with ± 0.08 bar for 63 % of data, so 99 % of data will be within ±0.25 bar (3 σ). This statistical noise was found to be valid for long-term measurements with no flow and temperatures almost in equilibrium with ambient. As known for statistical error, a difference from two pressure sensors will be hampered by the geometrical sum (simply Pythagoras) so such a calculated result will be affected by a noise of about ±0.12 bar (1 σ).

4.3.4 Development of a correction for pressure sensors

To get some usable trend data from more pressure sensors despite of temperature related deviation, a method was developed to correct the raw data. Because this was a work in progress, the final results were not available at the beginning of the benchmark process, so the models had to rely basically on the data from the better class of sensors. The comparing of the results was finally done with the corrected data.

First, a temperature and pressure influence on deviation of pressure sensors was observed, as well as a constant bias. Data were based on shutdown state of the loop, where no dynamical pressure drop will occur, and difference in pressure should only result from density of fluid and different vertical position of sensor.

A reference pressure was defined from the average of the pricier sensors in the loop, stating that TK01 P502 in first order, and TK01 P302 as well, were stable over a wide range of temperature and pressure, with nearly no constant bias from calculated saturation pressure. Hence, it was concluded that these two sensors could be used as a norm for calibration. Because of the check valve TK01 S204 (valve 6), during shutdown, there may be two different pressure states in the system, before and after check valve. Therefore, TK01 S502 represents the pressure on low-pressure side with the UHS, TK01 S302 the possibly higher pressure at CHX and SEH. During shutdown, with closed block valves, TAC mostly follows the low-pressure side via the slightly leaking check valve TK01 S502 (valve 26).

Data were collected for long-term stable situations at different pressures and temperatures with no changes of ambient temperature and system temperature observed. So the nearby temperature sensors could be used as reference for the sensor's temperature. For convenience, the uncorrected temperature was used, to avoid influence of improper compensation, assuming a constant shift only (see section about temperature measurement error).

The result were pressure deviations for all pressure sensors representing a function

$$\Delta p = p_{sensor} - p_{reference} = \Delta p\ (T_{sensor}, p) \tag{3}$$

First attempt was carried out for D1.1, but with little success for dynamic situations outside the parameter range covered from the data set. Therefore, some improvement was strived for.

Based on the principle of balance of a Wheatstone bridge, the following parametrized function was assumed

$$\Delta p = a * (T - T_0) + b + c * (p_{sensor} - p_0) * (T - T_0) \tag{4}$$

The term with the product from pressure and temperature was supported by an article of Yan Liu et al (Liu, Wang, Zhao, Qin, & Fang, 2016).

Temperature and pressure T_0, p_0 may be taken for convenience as 0 °C and atmospheric pressure. A constant bias from improper choice or some shift in the Wheatstone bridge will be covered in the constant term *b*. From this, *b* sometimes may need some readjustment on a daily base.

Regression was done with EXCEL©. As a result, a set of coefficients was established for each of the sensors, so that all measured data for the equilibrium state could be corrected down to the statistical error of about 0.05% (1 σ).

4.3.5 Balance model of sensor's temperature

During transients it became obvious, that using fluid temperature directly as sensor's temperature in the correction will lead to overcompensation, rendering the result useless. From this, a time delay model was tried to damp the temperature influence over time, but it failed. Therefore, a balance model of sensor's temperature as a result of fluid temperature, metal temperature and ambient temperature was established.

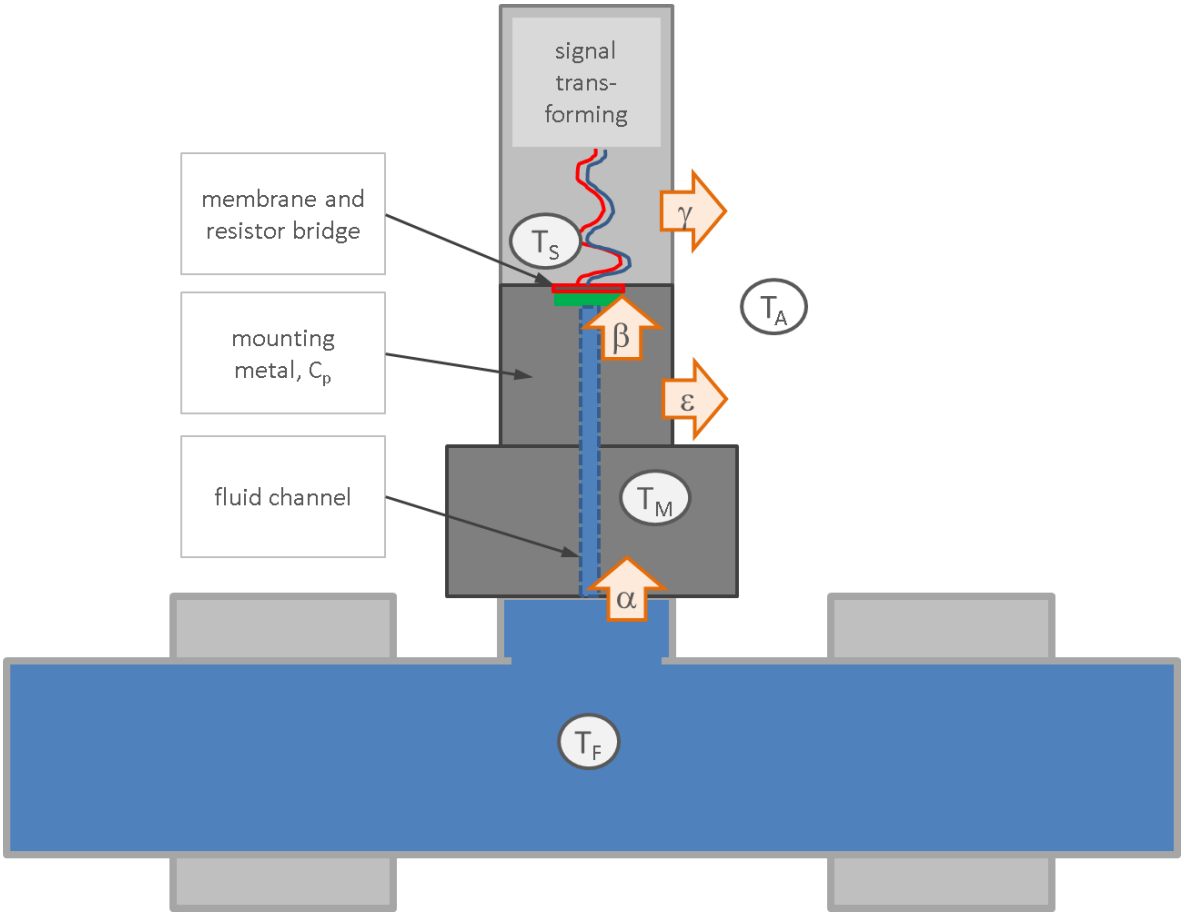

Figure 13 : Model of heat balance in the pressure sensor

The model is based on the balance of the following temperatures:

- Fluid temperature in contact with the metal of the sensor T_F
- Surface outside temperature T_O in a small layer with unspecified thickness, relevant for heat transfer
- Metal temperature (averaged) T_M, relevant for storage of heat
- Sensor's temperature T_S, relevant for the correction above
- Ambient temperature T_A for heat loss from metal and sensor, for simplicity as one lumped value.

For heat transfer, the following parameters were defined:

- From fluid to metal surface $Q_{in} = \alpha(T_F - T_O)$
- From surface layer to metal $Q_{in} = \delta(T_O - T_M)$. No heat storage was assumed in the layer. So Q_{in} is valid for both.
- From metal to sensor $Q_{M,S} = \beta(T_M - T_S)$
- From sensor to ambient $Q_{S,A} = Q_{M,S} = \gamma(T_S - T_A)$. No heat capacity was assumed for the sensor, so there has to be a balance of heat flow.

- From metal body to the ambient $Q_{M,A} = \varepsilon(T_M - T_A)$.
- For heat storage in the metal body, increasing metal temperature: $Q_{M,M} = C_p \, \Delta T_M$

The contact of the fluid via the narrow channel to the sensor is neglected because the stagnating fluid is assumed to be in close connection to the metal temperature. In some transient situations, when the channel may be purged, some deviations are to be expected.

Furthermore, the direction of the channel matters: in horizontal orientation (as for TK06 P101/201), some circulation may cause different characteristics for heat transfer to the metal.

Finally, ambient conditions matter. TK01 P101 (with the black plastic head) is located near to the window plate to the outside, with a continuous inflow of cold air. Therefore, the upper metal part will be kept colder than comparable sensors at the glass model presentation room (see Figure 2).

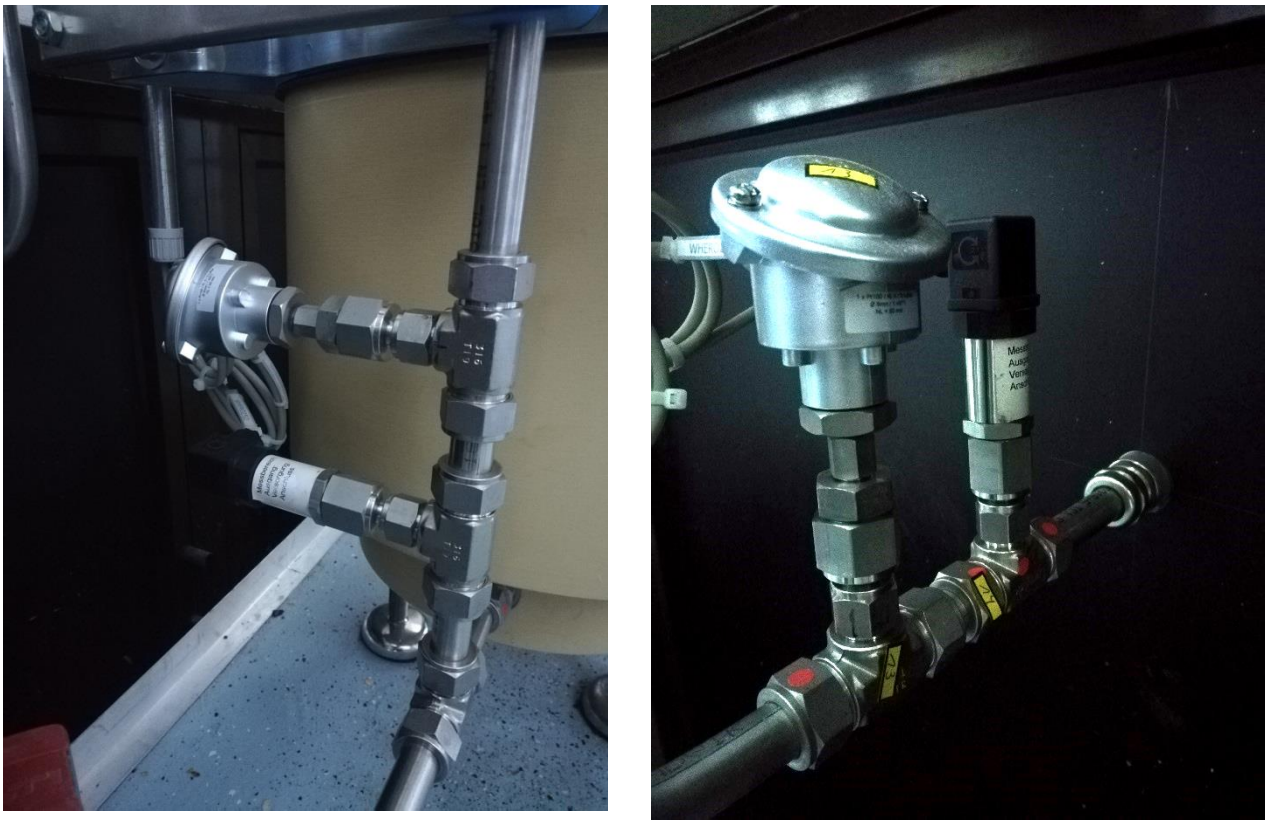

Figure 14 : Different orientation, position and ambient conditions for pressure sensors TK06 P201, TK01 P101

From balancing the heat, the following relations were derived:

$$Q_{in} = \alpha(T_F - T_O) = \delta(T_O - T_M) = \alpha\left[T_F\left(1 - \frac{\alpha}{\alpha+\delta}\right) - \frac{\delta}{\alpha+\delta}T_M\right] \tag{5}$$

For simplicity, the thickness of the surface layer handling the heat transfer can be adjusted virtually to a size the thickness will cause a $\delta = \alpha$. From this, the heat influx can be simplified to

$$Q_{in} = \frac{\alpha}{2}\,(T_F - T_M) \tag{6}$$

A similar relation is valid for the sensor's balance. The following equations can be established:

$$Q_{M,S} = Q_{S,A} = \beta(T_M - T_S) = \gamma(T_S - T_A) \tag{7}$$

From this follows

$$T_S = \frac{\beta T_M + \gamma T_A}{\beta + \gamma} \tag{8}$$

$$Q_{M,S} = \beta\left[\left(1 - \frac{\beta}{\beta+\gamma}\right)T_M - \frac{\gamma}{\beta+\gamma}\,T_A\right] \tag{9}$$

Now the heat balance for the metal of the pressures sensor can be written

$$Q_{M,M} = Q_{in} - Q_{M,A} - Q_{M,S} \tag{10}$$

$$C_p\,\Delta T_M = \frac{\alpha}{2}\,(T_F - T_M) - \varepsilon(T_M - T_A) - \beta\left[\left(1 - \frac{\beta}{\beta+\gamma}\right)T_M - \frac{\gamma}{\beta+\gamma}\,T_A\right] \tag{11}$$

So ΔT_M can be written in two ways. First:

$$\Delta T_M = \frac{\alpha}{2C_p}\left\{(T_F - T_M) - \left[\frac{2\,\beta}{\alpha}\left(1 - \frac{\beta}{\beta+\gamma}\right) + \frac{2\,\varepsilon}{\alpha}\right]T_M + \left[\frac{2\,\varepsilon}{\alpha} + \frac{2\,\beta}{\alpha}\cdot\frac{\gamma}{\beta+\gamma}\right]T_A\right\} \tag{12}$$

Here $\frac{\alpha}{2C_p}$ can be interpreted as an inverse time constant τ^{-1} for temperature changes from fluid temperature to metal temperature. Further, all other parameters can be seen relative to α, therefore for tuning purpose it can be set to unity. All other parameters may be balanced to this to fit the sensor's properties regarding temperature delay.

Second, the formula can be regrouped to give ΔT_M a simple relation to the temperatures:

$$\Delta T_M = -\left[\frac{\alpha}{2C_p} + \frac{\beta}{C_p}\left(1 - \frac{\beta}{\beta+\gamma}\right) + \frac{\varepsilon}{C_p}\right]T_M + \frac{\alpha}{2C_p}\,T_F + \left[\frac{\varepsilon}{C_p} + \frac{\gamma}{C_p}\cdot\frac{\beta}{\beta+\gamma}\right]T_A \tag{13}$$

So three coefficients can be calculated beforehand for solving the differential equation by

$$T_M(t + \Delta t) = T_M\,(t) + \Delta T_M(T_M\,(t), T_F(t), T_A(t)) \tag{14}$$

An initial temperature $T_M(t_0)$ has to be set for the initial value problem.
For fitting of the parameters some simple assumptions can be used, such as bringing all pressure differences to zero at no flow (taking geodetics into account), keep a constant pressure drop at stable flow conditions a.s.o. For parameters like γ, ε air flow from fans or air conditioning may be considered. Parameters like C_p, β will differ for different size of measurement, but should be widely similar for the same type.
Table 2 gives an overview for the fitting parameters used for pressure data in the benchmark test.

Table 2: Fitting parameters (rounded) for pressure sensors

Sensor	Location	a	b	c	α	β	γ	ε	Cp
TK01 P101	after UHS	0,0637	0,30	-0,00169	1	0,63	0,2	0,28	250
TK01 P202	before CHX	-0,0952	3,32	-0,000833	1	1	0,075	0,1	250
TK01 P301	after CHX	0,172	-2,49	-0,00115	1	1	0,075	0,1	250
TK01 P302	before SEH	0,0297	-0,64	-9,63E-05	1	0,1	0,1	0,8	400
TK01 P401	after SEH	-0,00239	0	-0,000188	1	0,1	0,1	0,8	400
TK01 P402	TAC in	-0,0154	0,36	0,000201	1	0,1	0,1	0,8	400
TK01 P501	TAC out	-0,0390	0,50	0,000317	1	0,1	0,1	0,8	400
TK01 T502	before UHS	0,0102	0,1	-8,45E-05	1	0,1	0,1	0,8	400
TK02 P101	TAC leakage	-0,111	2,0	0,00109	1	0,1	0,1	0,8	400
TK06 P101	PV1	0,0488	0,341	-0,000598	1	1	0,01	0,08	150
TK06 P201	PV2	-0,304	6,94	0,000598	1	1	0,01	0,08	150

The example in Figure 15 demonstrates the impact of temperature on pressure sensor, here TK06 P201, when taking the warm fluid at the moment PV2 piston is slowly lifted from pressure.

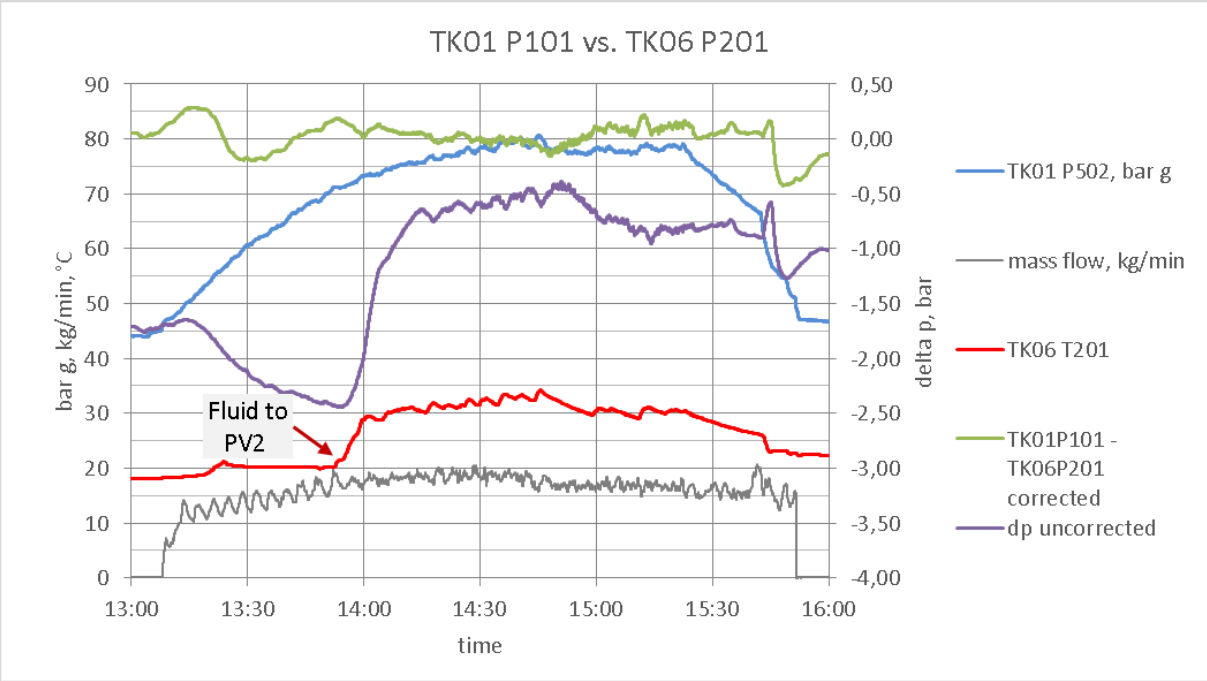

Figure 15 : Compensation of temperature effect on TK06 P201

The correction compensates the deviation, caused by the rapid warm up of the sensor, as can be seen from the purple curve of pressure difference, nearly completely for the corrected pressured difference (green curve). Basically, with no flow, pressure difference should be zero.

4.3.6 Oscillations

With regard to stationary conditions in classic sense with constant parameters for flow, temperature and pressure, oscillations clearly posed a problem. This can be seen from density before CHX, plotted over time in Figure 16.

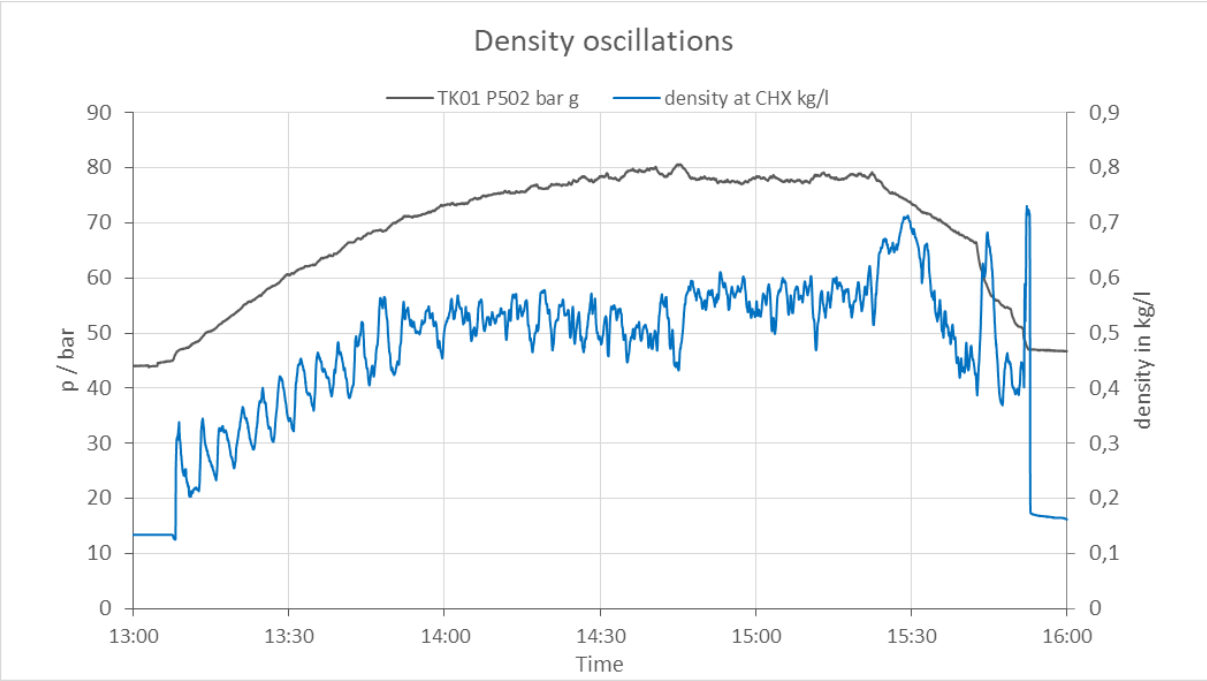

Figure 16 : Density oscillations during the run for benchmark data on 10th of March 2020

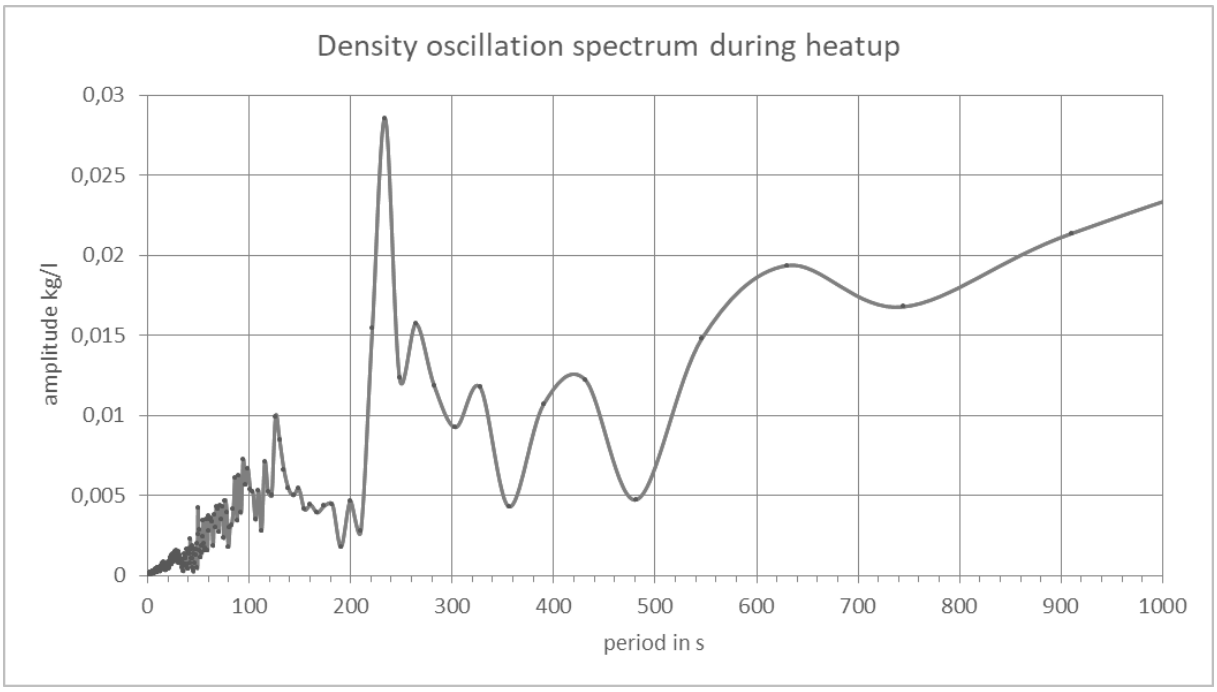

Figure 17 : Amplitude spectrum of density during heat-up into supercritical state (until 14:16)

During slow heat-up as well as with nearly constant pressure and power, clearly pronounced oscillations can be detected, with slightly different characteristics for these two different phase states.

Heating up from 45 bar, the fluid is in dual phase state when coming slowly up to 500 kg/m³ (0.5 kg/l).

From Fast Fourier Transformation (FFT) over 4096 seconds, beginning with the start of PP, the directly visible period of about 240 s can be confirmed as the dominating mode in Figure 17.

If it comes into supercritical phase state, the frequency pattern becomes more complex. The main peak for amplitude is shifting to 280 s, with the peak at 240 s still visible, but in the same size as the peaks from higher frequencies (with shorter period). Signal components with longer period may result from adjustments in power and fan speed, to stabilize pressure and temperature.

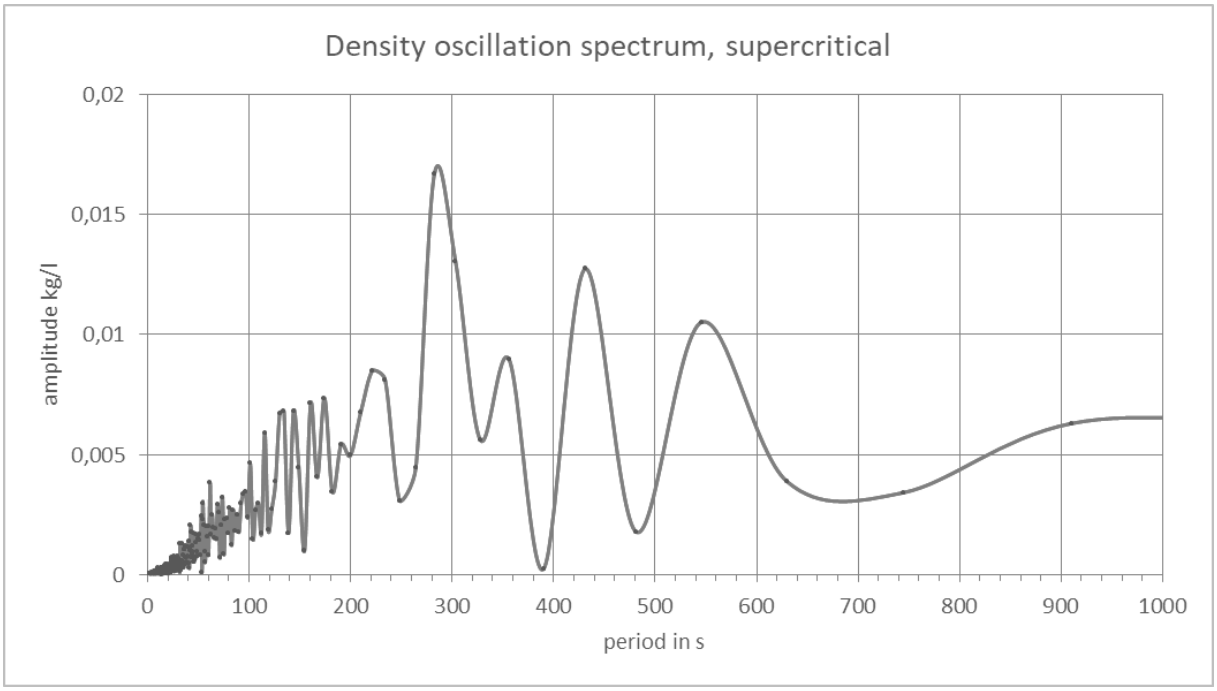

Figure 18 : Amplitude spectrum of density during supercritical state, 14:16-15:24

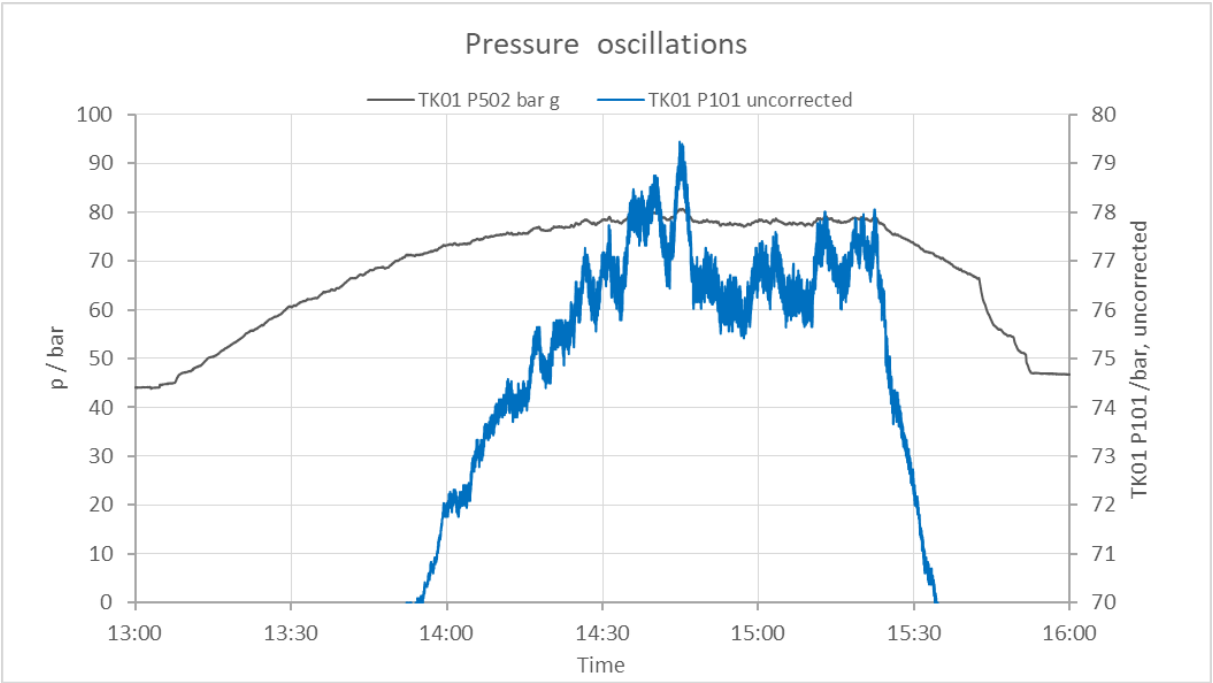

Figure 19 : Pressure oscillations at TK01 P101 in supercritical region

The presence of the oscillation for other parameters of the circuit can be demonstrated by the pressure TK01 P101 (Figure 19, the uncorrected signal was used here), which shows short term noise as well as long term fluctuations. Focused on the same time span as the density analysis for supercritical region, TK01 P101 amplitude spectrum (Figure 20) follows the density with same peaks in 280 s, 430 s and around 550 s.

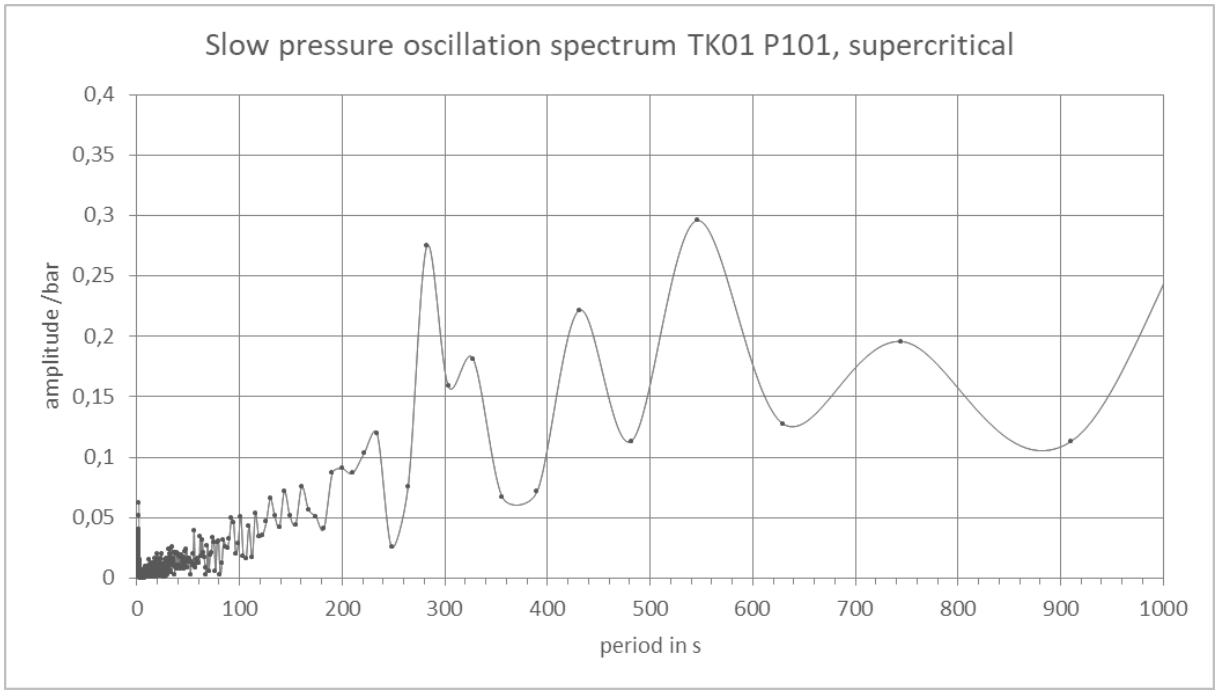

Figure 20 : Amplitude spectrum of TK01 P101 in supercritical region

Such fluctuation in thermal hydraulic cycles are known from boilers, steam generators, nuclear reactors (e.g. neutron flux oscillations, LaSalle-Effect) and have to be avoided or damped, mainly by proper throttling in the denser region of the fluid.

Whereas the mechanism for these oscillations needs further thorough investigation, it is obviously that these instabilities will hamper the effort to get a defined initial state for the benchmark tests and therefore to get comparable results in between the models. Furthermore, models detailed enough to reproduce these instabilities may get difficulties in convergence. Models with less details in density distributions alongside the flow path may not be able to reproduce these oscillations in principle.

A short period oscillation can be observed from the data, too. It comes up near the critical point and may be some resonance in volumes to the PV or in the pipes itself, when speed of sound in gaseous and liquid part of the fluid unifies below 200 m/s. The frequency is higher than 0.5 Hz, as to be seen from the spectrum in Figure 21: the edge on the left hand side marks the cut-off frequency 0.5 Hz with 2 seconds period, according to Shannon's theorem, taking one data point per second. Such oscillations may cause some limited deviations in the measurement, as well as damages during long term operation of a cycle. Therefore, it will be interesting to investigate the mechanism further in the project. For benchmark purpose it can be smoothed out mostly.

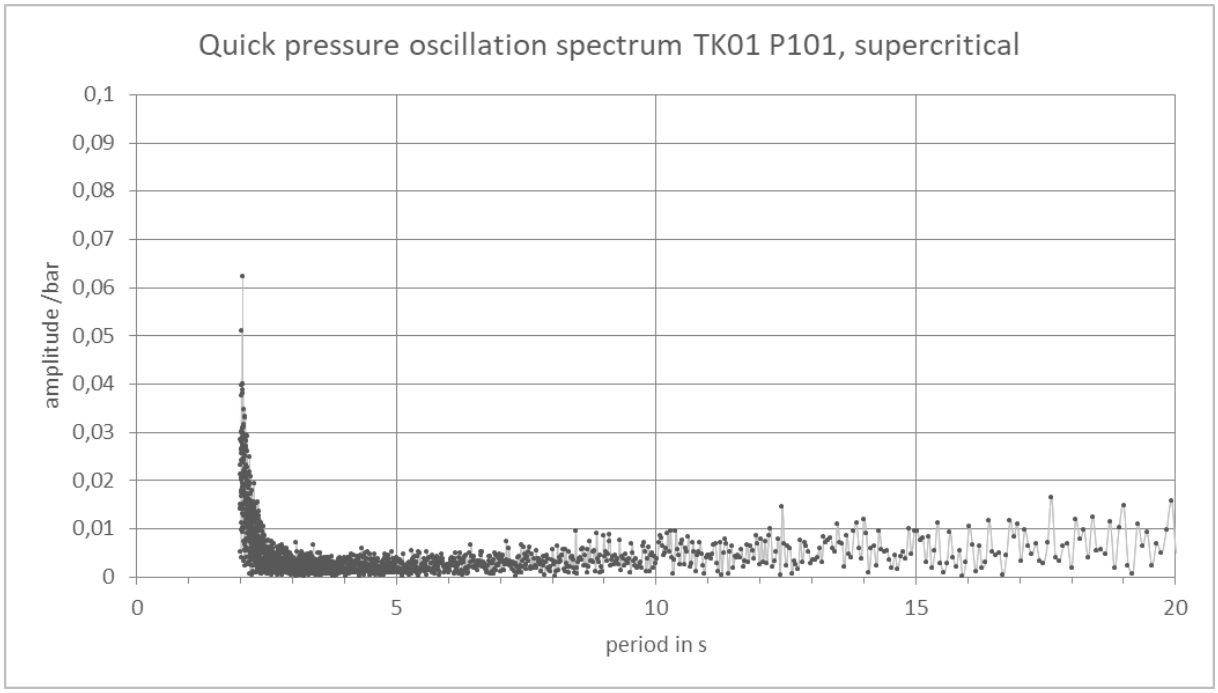

Figure 21 : Amplitude spectrum for TK01 P101 towards shorter period, limited by sampling frequency

5 Modelling of cycle and components

5.1 CATHARE

The work carried out in CATHARE involved several challenges for EDF.

Firstly, only the CATHARE 3 version under development allows to model a cycle running on supercritical CO_2. Some of the assumptions made for the modelling are therefore derived from these constraints and will be further developed as EDF is in contact with the code development team in order to discuss certain modelling features (i.e. the modelling of the turbomachine).

The modelling of a sCO2 cycle in CATHARE is also a challenge for EDF, because EDF had to adapt the characteristics of a cycle that is still unknown (from an operational point of view and on how to model it in CATHARE). The components of the sCO_2 cycle required an innovative approach for their modelling because they are not components usually used in CATHARE datasets and therefore had to be modelled from scratch.

5.1.1 General description of the modelling tools

The CATHARE code is a French thermal-hydraulics system code developed since 1979 and extensively validated in collaboration between CEA, EDF, IRSN and FRAMATOME (Barre F., 1990). It was first devoted to best estimate calculations of thermal-hydraulics transients in nuclear reactors. CATHARE-2 is the current industrial version of the CATHARE code. It is internationally used for nuclear power plant safety analysis and licensing (IAEA, 2001) and in plant simulators (Miettinen, 2008).

CATHARE-3 is the new development version of the code (P. Emonot, 2011). The CATHARE code is based on a two-phase six-equation model (Ishii, 1975) including additional equations for non-condensable gases and radio-chemical components transport. This model is established from the local instantaneous mass, momentum and energy equations. The global non-linear system is solved using a Newton-Raphson iterative method.

These equations are averaged for each phase and make possible representing mechanical and thermal disequilibrium between phases (Faydide & Rousseau, 1980). The six main hydraulic variables are:

- Pressure,
- Void fraction,
- Liquid and gas enthalpies and velocities.

CATHARE code allows the coolant circuits of any reactor to be represented by assembling axial (1-D), volume (0-D) and three D (3-D) hydraulic modules. Thermal and hydraulic sub-modules such as thermal walls, heat exchangers, pumps, valves, turbines, fluid source and sink can be added to these main modules. First developed and qualified for the modelling of pressurized water reactors, the CATHARE code has been adapted to deal also with gas cooled reactor applications. In order to use the code for gas-cooled reactors transient simulation, some specific features and models have been developed in the 2000s:

- First, the standard two-phase fluid model has been adapted to carry very high fraction of ideal non-condensable gas that could be helium, nitrogen or a mixture of both.
- Then, a 0-D turbomachinery sub-module based on the ideal gas assumption has been developed to describe a compressible fluid rotating machinery that is either a gas turbine or a compressor. The model computes the specific head *H* and torque *t* exchanged with the fluid crossing the turbomachine

depending on both rotational speed *u* and fluid flow rate *m*. They are used specifically in CATHARE to deal with two-phase flow in turbomachinery submodules.

- A shaft sub-module enables to slave several turbomachine sub-modules to model a whole turbomachinery. An optional alternator model can also be added to this shaft.
- Finally, friction and heat exchange correlations have been integrated in the code to describe specific heat exchangers and fuel assemblies.

The new CATHARE-3 code must be able to accurately model all reactor transients. However, the current CATHARE transient calculations lead to significant uncertainties related to the use of the ideal gas models. It's because the CATHARE ideal gas model is based on a reference pressure of 1 bar and assuming that the gas properties only depend on temperature as polynomials of degree three. For this reason, new real gas features and models have been developed and integrated in the CATHARE-3 code and are presented in following sections (Mauger, Tauveron, Bentivoglio, & Ruby, 2019).

In the framework of the NEPTUNE project, it was decided to build the NEPTUNE platform on a component architecture (Guelfi, Bestion, Boucker, Boudier, & all, 2007). The same component can be used by different NEPTUNE thermalhydraulics codes such as CATHARE-3 or NEPTUNE-CFD. Especially, the EOS component has been developed to compute the thermodynamic and transport properties of the fluids from several inhouse code libraries such as CATHARE-2, THETIS, FLICA-4, etc. REFPROP (National Institute of Standards and Technology,) has been implemented as a new library in the EOS component in order to use the carbon dioxide equation of state in CATHARE-3. REFPROP core property routines compute thermodynamic and transport properties of many fluids using a Helmholtz energy approach mainly intended for scientific use. Moreover, new methods have been developed in the EOS component to access properties only available in the REFPROP libraries such as speed of sound and entropy.

5.1.2 Main hypothesis for the CATHARE modelling

The main hypothesis which have been used in the CATHARE simulations are as follow:

- The simulated fluid is CO_2.
- The fluid properties are calculated by EOS (Equations of State) and coupled with REFPROP (Reference Fluid Thermodynamic and Transport Properties Database).
- Only a one- phase flow is simulated for the supercritical CO_2 continuous field (without phase change).
- The set of closure relationships is the standard set used in CATHARE for water; at this stage no additional correlation was devolved or adapted to supercritical CO_2 fluid.

5.1.3 Description of the loop modelling

The simplified CATHARE modelling of the loop is made up of pipes and three heat exchangers: the SEH, the UHS and the CHX. They are all modelled by 1D-elements in CATHARE (Figure 22).

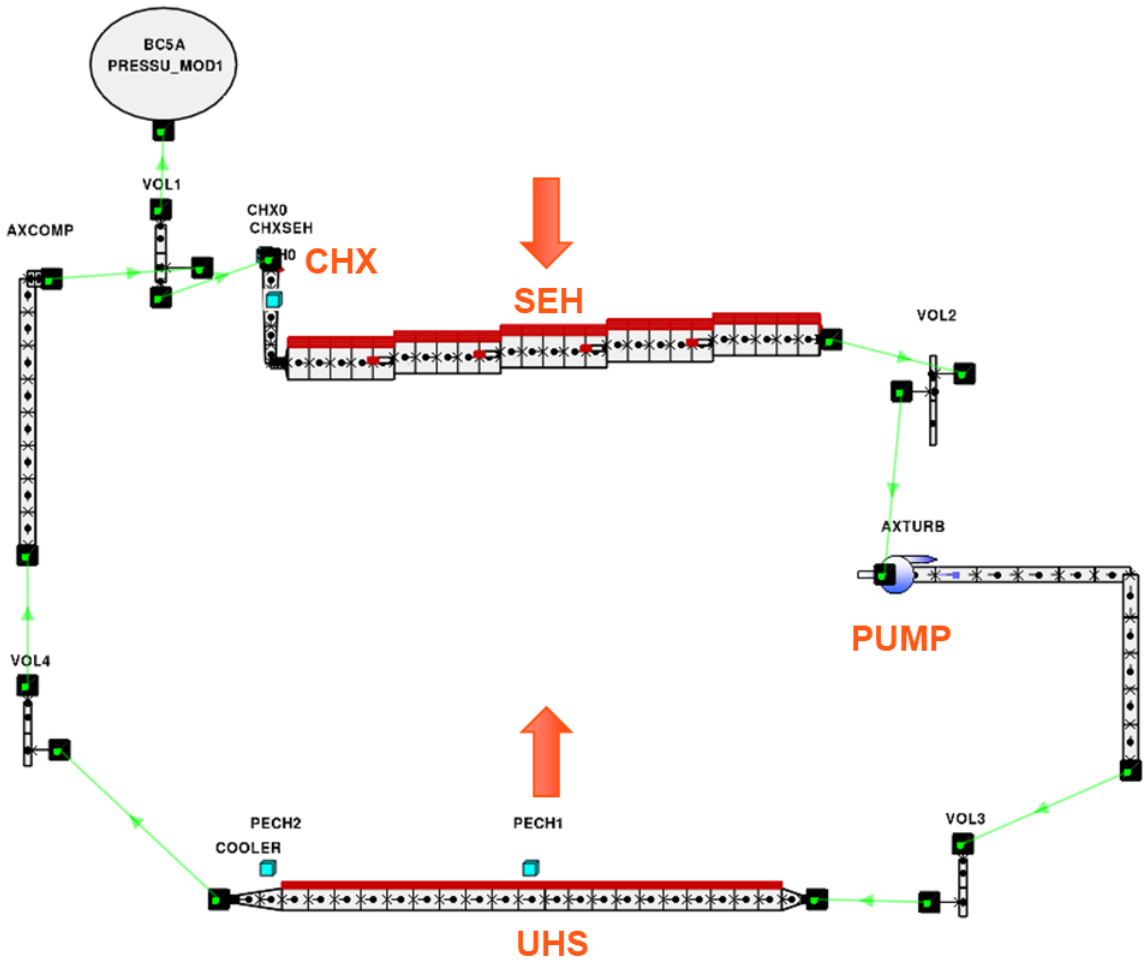

Figure 22 - Simplified CATHARE modelling of the loop

The numerical values adopted in CATHARE for all these components are summarized in Table 3.

The pipes are characterised by their diameter, their perimeter, and their section. Their length is globally respected in term of direction and altitude.

The internal diameter of **SEH** is deduced from its external diameter and the tube thickness. The perimeter and section can be then calculated from this internal diameter. The length represents the total length of the tube with a vertical elevation of 2 meters.

The **UHS** is modelled on the base of the diameter (characteristic dimension) of a single tube. The global perimeter and global section are deduced from this diameter which is multiplied by the 8 tubes for each of the parallel units in the loop that together represent the UHS. The length represents the total length of one tube. On the air side, the fins around the tubes cannot be modelled easily using the current input parameter for plane tubes, therefore their contribution is modelled through a correction factor of the air side heat transfer coefficient.

The perimeter of the **CHX** is determined by the perimeter of one rectangular channel which is multiplied by the 15 channels for one plate, and the 14 plates on the sCO_2 side. The section is determined in the same way. The equivalent diameter is determined by the definition of the hydraulic diameter, which takes into account the perimeter and the section for one channel.

Table 3: Numerical values adopted in the CATHARE modelling

Component	Diameter (m)	Perimeter (m)	Section (m²)	Length (m)	Thickness (m)
Pipes	0.0156	0.049	0.00019	~ 30 m (total)	*Undefined*
SEH	0.0491	0.154	0.0019	46.7	0.0056
UHS (*2)	0.0106	0.533	0.0014	44.8	0.001
CHX	0.00133	1.26	0.00042	0.2016	0.0024

A pump has been integrated in the circuit in order to impose a flow in the loop. We had some difficulties to model this pump in the CATHARE code correctly, and more specifically to accurately determine all the specific input data necessary in the CATHARE modelling options from the real loop characteristics used in the experiments.

Therefore, we have adopted coarse hypothesis in the dataset in order to approximately obtain the same flow rate in the simulations as the experiment. This “adjusted” pump allowed us to obtain preliminary results, especially for the stationary state of the loop. But this is clearly an important limit of our modelling which needs to be improved in the future simulations.

5.1.4 Boundary conditions

In the CATHARE modelling, different boundary conditions have been defined (Table 4).

The pressure is imposed at the top (highest point) of the loop to make the convergence of the calculations easier. In reality and for future non-stationary simulations, this boundary condition seems to be unnecessary because the pressure naturally regulates itself in the loop depending on initial thermal-hydraulic conditions and heat transfers that occur in the heat exchangers. It might possibly be performed in the future by “closing” the boundary condition during the transient simulation in CATHARE.

Table 4: Numerical values adopted for boundary conditions

Boundary conditions	Adopted value
Pressure at the top of the loop (bar)	74
Thermal flux in the SEH (W/m²)	2800
Air temperature on the first UHS part (°C)	14
Air temperature on the second UHS part (°C)	25
Heat transfer coefficient in the air side (W/m²/°C)	75
Steam temperature (°C)	285
Heat transfer coefficient in the steam side (W/m²/°C)	10^{-6} (deactivated)

A constant thermal flux in W/m² is imposed all along the wall of the different cells representing the SEH in order to respect the total power imposed during the experiment.

The air side of the UHS is simply modelled by a temperature for air side and a heat transfer coefficient. In order to take into account the heating of the air along the UHS exchanger, the CATHARE modelling considers a spatially discretized air temperature along the UHS. The air temperature is approximately set to 14 °C on the first part (22.8 m) of the UHS tubes and 25 °C on the second part. The heat transfer coefficient is multiplied by a "correction" factor to take into account the presence of fins on the tubes (air side) which improve the heat exchange.

The CHX is thermally deactivated by imposing a very low value for the heat transfer coefficient.

5.1.5 Loop elements to be modelled later

The CATHARE model needs some improvements for better accuracy regarding the experimental results calibration. The pressure of the circuit must be globally increased by adding singular head losses in the circuit and/or by changing the pressure boundary condition location where the pressure value is higher for example. Furthermore, the SEH heat exchanger modelling in CATHARE is for now too simple to get accurate results. Indeed, the flux calculation considers a constant heat exchange coefficient and air temperature. The air loop must be modelled in the future to get the air temperature variation and some correlations must be used for the heat exchange coefficient calculation. Lastly, the pump modelling in CATHARE is very challenging because volumetric PP are not available. We need to adapt and tune centrifugal pump for example to get the needed flowrate.

5.2 MODELICA

One of the three tools used to numerically simulate the real HeRo loop physical behaviour is MODELICA. Below depicted Figure 23 roughly shows the overall programming environment together with the individual instruments versions. Real gas properties are supported via TS Media library, which is REFPROP compatible concerning CO_2 properties. In this way, the HeRo loop numerical model is characterized by 1D, correlation based environment when taking into account the basic conservations laws of physics for time dependent processes.

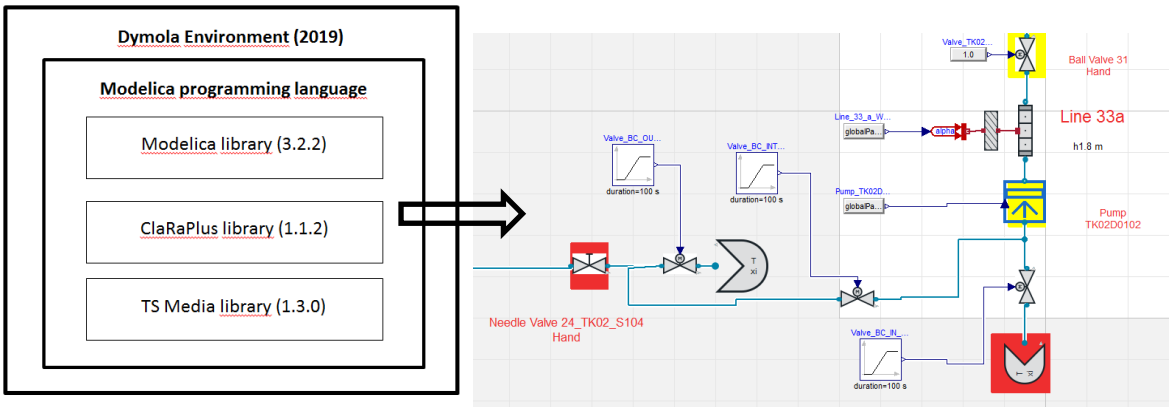

Figure 23: Programming environment

5.2.1 General description of the HeRo loop model

Current benchmark concentrates on the UHS, SEH, PP, valves and piping thermo-fluid behaviour modelling. In the MODELICA model, the CHX heat exchanger is now represented by a pipe element. Also the pressure vessels

number 1 and 2 are not included into the loop model yet. The heat exchange between the CO_2 and ambient air is not included for the indoor piping.

As a basic source of geometrical and performance data following documents were used:

- Data on behaviour of the sCO2-HeRo-loop and the glass model, (Hacks & Hecker, 2019)
- Geometry.xls
- Delivery of sink HX performance maps, (Vojáček A. , 2017)
- Güntner drawings of UHS (400-0000631155)
- 2020_03_10_stable_supercritical_1448_to_1522_form.xls
- Preliminary 3D CAD model of HeRo loop installation
- Photographs of HeRo loop installation including UHS photographs

During the modelling some of the pipe lines were collected together, nevertheless an attention was payed to preserve the length and vertical changes as they are described in the Geometry.xls file.

The modelling approach concerning the main components including UHS, SEH, PP and valves will be discussed in some detail within the next paragraphs.

5.2.2 Ultimate Heat Sink (UHS)

Due to very complex geometry, the symmetry and similarity of sections of the UHS heat exchanger was used for modelling in MODELICA. The UHS was divided into 8 parts according to individual tubes. This is described in Figure 24.

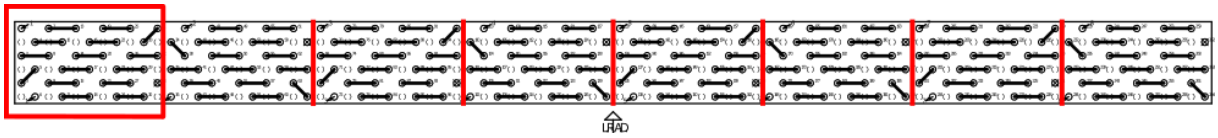

Figure 24: Division of UHS to 8 equivalent sections

Each of 8 pipes has 32 passes through the UHS with flow direction alternation. Because MODELICA is designed for 1-D simulations, alternation in the horizontal direction was neglected and pipe was straightened as you can see in Figure 25.

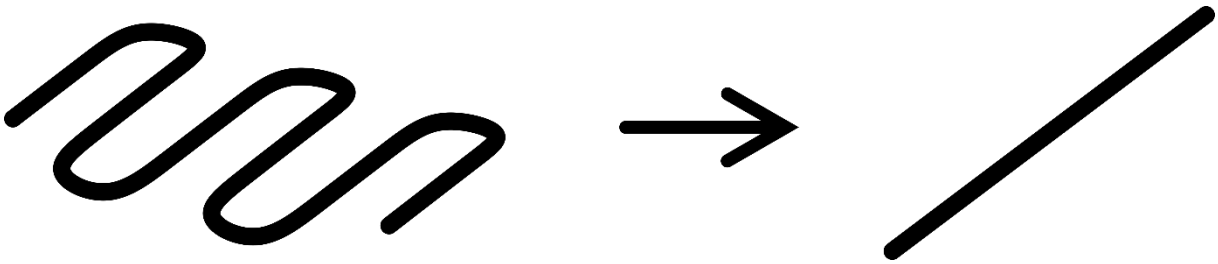

Figure 25: Transformation of curved pipe to straight pipe

This transformation, combined with division of the pipe to six separated pipes, each in one row (stage), converted the geometry of section to long parallel straight pipes (Figure 25), so it is easier to describe it in MODELICA language.

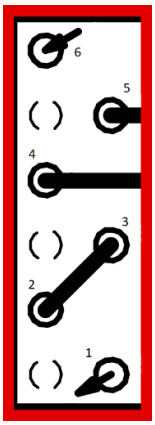

Figure 26: Control Volume section

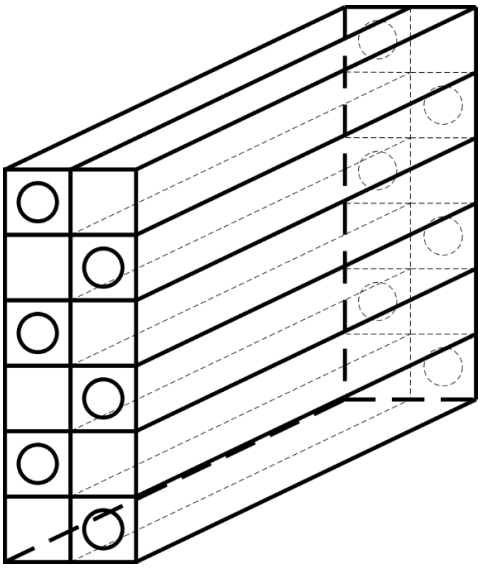

Figure 27: Division of customized UHS section

Figure 28: Air channels bounded by fins

With these customizations it is possible to create the model of the UHS as two perpendicular series of tubes. Vertical series for the air flow and horizontal series for the CO_2. Dimensions of the control volume have been defined, see Figure 26, Figure 27, Figure 28, so the equivalent diameter for the air tubes can be determined. Each of n CO_2 tubes elements is connected to appropriate element of the air tubes, which represents a certain vertical position in the UHS. This is realized by simple "for cycles" in the MODELICA connections, see example below.

```
for i in 1:(co2 tubes row2.N cv) loop
connect(air tubes.heat[5], wall co2 row5.outerPhase[i]) a;
connect(air tubes.heat[3], wall co2 row3.outerPhase[i]) a;
connect(air tubes.heat[2], wall co2 row2.outerPhase[i]) a;
connect(air tubes.heat[1], wall co2 row1.outerPhase[i]) a;
end for;
```

These connections are intended only for the heat transfer. Characteristics of the air flow around the CO_2 is neglected. Parallel air tubes are defined only for mass flow so temperature at individual stages is the same for each of the parallel tubes. Due to this change of geometry in the model, the flow mode of air side is different from the arrangement point of view. But it is possible to calculate the flow modes for real geometry for example in Excel and make some interpolation curves for pressure drop and heat transfer coefficient, which can be used in MODELICA as prescription for the heat transfer and pressure losses for the air side.

Currently, a constant heat transfer coefficient for the air side is used. The correlation from Vojáček (2017), see below, was used for calculations.

$$Nu = 0.23\, Re^{0.63} \cdot Pr^{\frac{2}{3}} \tag{15}$$

$$1500 \frac{d_e}{d_h} Re < 70000 \tag{16}$$

The values of the heat transfer coefficient at the air side for d_e = 0.116m and d_h = 0.00405m are summarized in the following Table 5 as a function of air inlet temperature and the fan speed.

Table 5: Heat transfer coefficient at the air side

		10% RPM		20% RPM		30% RPM		40% RPM		50% RPM	
T_air [°C]	T_air [K]	Re	alpha [W.m^-2.K^-1]	Re	alpha [W.m^-2.K^-1]	Re	alpha [W.m^-2.K^-1]	Re	alpha [W.m^-2.K^-1]	Re	alpha [W.m^-2.K^-1]
20	293,15	218	6	436	9	654	11	872	13	1090	15
22	295,15	212	6	423	9	635	11	847	13	1058	15
24	297,15	209	6	418	9	627	11	837	13	1046	15
26	299,15	207	6	413	9	620	11	827	13	1033	15
28	301,15	204	6	408	9	613	11	817	13	1021	15
30	303,15	202	5	404	8	605	11	807	13	1009	15
32	305,15	199	5	399	8	598	11	798	13	997	15
34	307,15	197	5	394	8	591	11	789	13	986	15
36	309,15	195	5	390	8	585	11	780	13	974	15
38	311,15	193	5	385	8	578	11	771	13	963	15
40	313,15	190	5	381	8	571	11	762	13	952	15
42	315,15	188	5	377	8	565	11	753	13	942	15
44	317,15	186	5	373	8	559	11	745	13	931	15
46	319,15	184	5	368	8	553	11	737	13	921	15
48	321,15	182	5	364	8	546	11	729	13	911	15
50	323,15	180	5	360	8	541	11	721	13	901	15
52	325,15	178	5	356	8	535	11	713	13	891	15
54	327,15	176	5	353	8	529	11	705	13	881	15
56	329,15	174	5	349	8	523	11	698	13	872	15
58	331,15	173	5	345	8	518	11	690	13	863	15
60	333,15	171	5	341	8	512	11	683	13	854	15

		60% RPM		70% RPM		80% RPM		90% RPM		100% RPM	
T_air [°C]	T_air [K]	Re	alpha [W.m^-2.K^-1]	Re	alpha [W.m^-2.K^-1]	Re	alpha [W.m^-2.K^-1]	Re	alpha [W.m^-2.K^-1]	Re	alpha [W.m^-2.K^-1]
20	293,15	1308	17	1526	19	1744	20	1963	22	2181	24
22	295,15	1270	17	1482	19	1693	21	1905	22	2117	24
24	297,15	1255	17	1464	19	1673	20	1882	22	2091	24
26	299,15	1240	17	1447	19	1653	20	1860	22	2066	24
28	301,15	1225	17	1429	19	1634	20	1838	22	2042	23
30	303,15	1211	17	1413	19	1614	20	1816	22	2018	23
32	305,15	1197	17	1396	19	1596	20	1795	22	1995	23
34	307,15	1183	17	1380	19	1577	20	1774	22	1972	23
36	309,15	1169	17	1364	19	1559	20	1754	22	1949	23
38	311,15	1156	17	1349	19	1541	20	1734	22	1927	23
40	313,15	1143	17	1333	19	1524	20	1714	22	1905	23
42	315,15	1130	17	1318	18	1507	20	1695	22	1884	23
44	317,15	1118	17	1304	18	1490	20	1676	22	1863	23
46	319,15	1105	17	1289	18	1473	20	1658	22	1842	23
48	321,15	1093	17	1275	18	1457	20	1639	22	1822	23
50	323,15	1081	17	1261	18	1441	20	1622	21	1802	23
52	325,15	1069	17	1247	18	1426	20	1604	21	1782	23
54	327,15	1058	17	1234	18	1410	20	1587	21	1763	23
56	329,15	1046	17	1221	18	1395	20	1570	21	1744	23
58	331,15	1035	17	1208	18	1380	20	1553	21	1725	23
60	333,15	1024	16	1195	18	1366	20	1536	21	1707	23

The heat transfer coefficient for the air side is one or two orders of magnitude lower than for the CO_2 side, so it determines the overall heat transfer.

To calculate the pressure drop at the air and CO_2 side, constant loss coefficients based on nominal conditions are used.

For CO_2 side, the geometry of model is approximately the same as in the real UHS. Gnielinski correlation for heat transfer and linear pressure drop for pressure losses are used.

$$Nu = \frac{\frac{\zeta}{8} \cdot Re \cdot Pr}{1 + 12{,}7 \cdot \sqrt{\frac{\zeta}{8}\left(Pr^{\frac{2}{3}} - 1\right)}} \left[1 + \left(\frac{d}{L}\right)^{\frac{2}{3}}\right] \tag{17}$$

$$\zeta = (1{,}8 \cdot \log(\mathrm{Re}) - 1.5)^{-2} \tag{18}$$

$$10^4 \leq Re \leq 10^6$$
$$0{,}1 \leq Pr \leq 1000$$
$$\frac{d}{L} \leq 1$$

Model schematics and geometry are depicted in Figure 29. During the modelling following references were used: (Vojáček A. , 2017), (Dostal, Goettelt, Melichar, Rohde, & Vojacek, 2019).

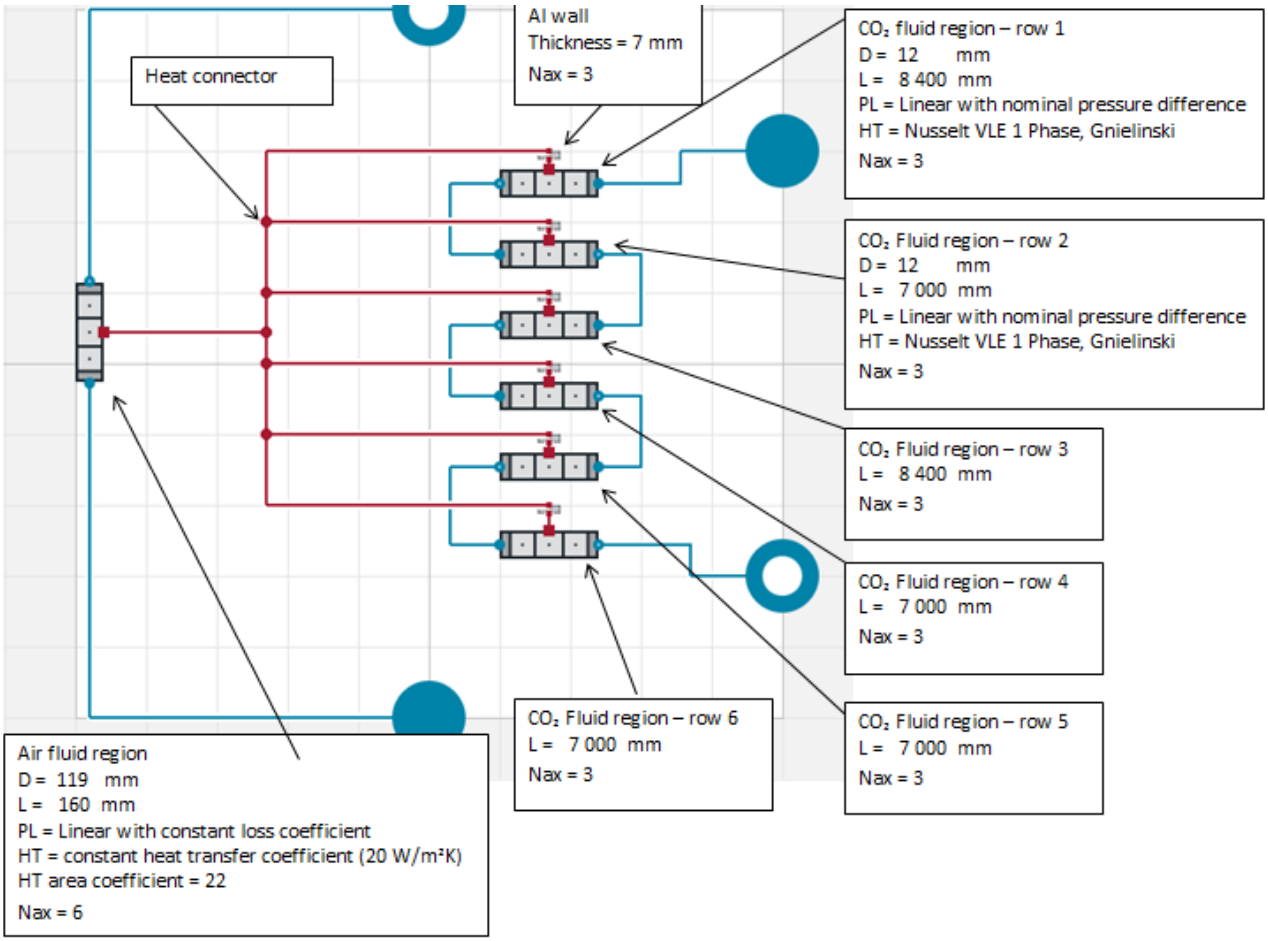

Figure 29: UHS model schematics

5.2.3 Slave Electrical Heater (SEH)

The SEH model structure is depicted in Figure 30 in a form of MODELICA environment print screen. Basic dimensions of the SEH model, **p**ressure **l**oss and **h**eat **t**ransfer models are also shown. *dh* in the figure means

elevation change, *Di* is the inner diameter of the component, *Do* is the outer diameter and *L* is the component length. *Nax* represents number of axial elements used for discretiation of a particular region in the flow direction.

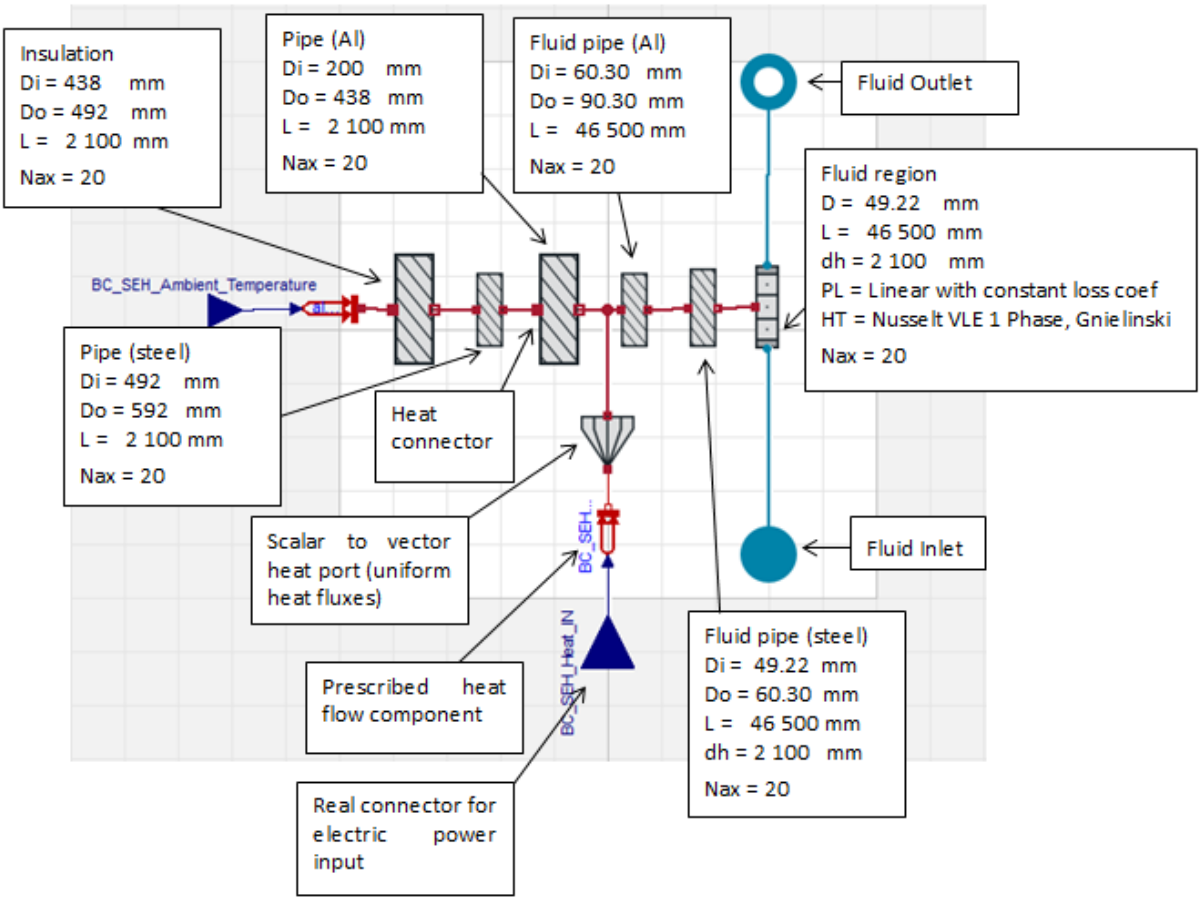

Figure 30: SEH Model

The MODELICA SEH model is composed of the 1 fluid and 5 solid straight concentric pipes of different length. The fluid region is 46.5 m long with diameter of 49.22 mm. Then corresponding steel pipe is attached. The aluminium filling is divided into 2 parts. One is the aluminium pipe attached to the steel pipe with 46.5 m length. The other aluminium part is 2.1 m long and serves as a heat capacitor so that total amount of 1 120 kg of aluminium filling is preserved. Total amount of the steel matter is approximately 1 000 kg. Individual regions are connected via heat connectors. The electrical heating rods are not modelled and are replaced by heat input along the whole aluminium pipe. This electrical heat input is uniformly distributed along the aluminium pipe length during the whole experiment. In this way the total heat flow through the individual heat ports is the result of superposition of this electrical heat input and heat flow arising from temperature differences between the individual regions. This description is visualised in the next Figure 31. As the model is 1D in nature, heat transfer is modelled only in the radial direction. Heat transfer between the fluid and solid is described by the Gnielinski correlation for one phase flow and heat conduction in the solid region is described by the thermal conductivity of the material. Actual pressure loss in the fluid region is mass flow dependent and is approximated by the linear dependency between prescribed nominal pressure loss and nominal mass flow rate.

$$\Delta p = \left(\frac{\Delta p_{nom}}{\dot{m}_{nom}}\right)\dot{m}. \tag{19}$$

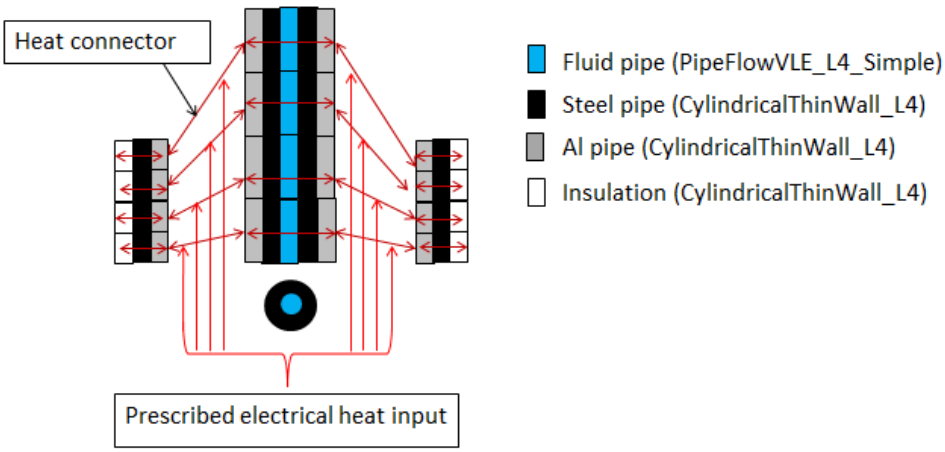

Figure 31: Heat connectors

5.2.4 Piston pump

Simple model of the PP that takes into account only the volumetric flow dependence on driver speed of revolutions and that handles the CO_2 as a real gas (TS Media library) was built. Thus the PP is only characterized by volumetric flow (2 l/s) at full speed (260 rpm).

When tuning the initial state for the subsequent transient benchmark, instead of prescribing the measured speed of revolution, the speed was adopted so that measured flow rate was reached. This is because in the reality there exist some parasitic effects like dead volume that were not modelled, which lead to lower mass flow rates compared to the ideal pump model.

5.2.5 Valves

In order to take into account several valves that are present in the real HeRo loop the ClaRaPlus library components has been utilized and incorporated in this way:

Ball valves

- Reference area 1.948e-4 m^2
- Zeta coefficient at full opening 0.71
- Quadratic Zeta, unchoked, incompressible

Reference area and zeta coefficient used in the model are in agreement with the ball valve characteristics as they are depicted in the geometry specification document. The fact that the pressure loss model does not take into account choking effects and compressibility is reasonable in the sense that ball valves serves like a closing element so the pressure drop over such a valve should be small in the open position.

Needle valves

- Reference area 0.7088e-4 m^2
- Zeta coefficient at full opening 2.2
- Quadratic Zeta, unchoked, incompressible

In this case zeta coefficient used in the model differs from that depicted in the geometry specification document for a given reference area (zeta_spec = 5.37). When using zeta = 5.37 this leads to an excessive pressure drop. In order to start the model zeta value 2.2 is adopted. Using an assumption of unchoked and incompressible flow is probably oversimplification in the case of needle valves. These valves are designated to control the flow by changing the pressure drop in potentially wide range.

Check valves

- Reference area 1.948e-4 m^2
- Zeta coefficient at full opening 1
- Quadratic Zeta, unchoked, incompressible

Also in this case zeta coefficient used in the model differs from that depicted in the geometry specification document file for a given reference area (zeta_spec = 5.95). When using zeta = 5.95 this leads to an excessive pressure drop. In order to start the model zeta value 1 is adopted.

Correct valve parameters and pressure drop model setting requires more examination. This shall be performed in the next stage of modelling effort as the correct pressure drop prediction within the loop for different conditions is crucial for the sustainability evaluation.

5.2.6 Loop elements to be modelled later

At the early stage of the WP 1.2 it was decided not to incorporate to the current benchmark neither the turbomachine set nor the CHX heat exchanger. Here below some short preliminary remarks are presented about their future modelling approach.

Turbomachine

The turbomachine set consists of the turbo-compressor, turbine and generator.

Concerning the turbo-compressor, a new component shall be prepared that shall be based on a set of non-dimensional coefficients representing pressure rise, flow and power. Performance curves shall be specified in a dimensional form as available from the measurements. The question about method of handling parasitic effects must be solved, maybe even leading to the necessity of iterative procedures what should be avoided.

Concerning the turbine it is believed that an existing model within the ClaRaPlus library might be utilized or a similar method compared to the compressor shall be used.

A simple model of the generator is also available within the ClaRaPlus library, but the question about windage losses must be solved.

CHX heat exchanger

One channel shall be modelled with the help of hydraulic diameter and corresponding correlations for heat transfer and pressure loss at the CO_2 side. Then this channel shall be copied as necessary. Modelling of the water condensation heat transfer coefficient in a channel flow is under investigation now, but the fact that heat transfer coefficient at the CO_2 side is determinative might be utilized.

5.3 ATHLET

The following subchapters provide an overview of the current development status of ATHLET concerning the modelling of the CO_2 loop and its components. Most of the points are either described in the ATHLET documentation or in literature in more detail, please refer to the cited publications in the subchapters. For a general description of ATHLET, please also refer to the ATHLET documentation (Austregesilo, et al., 2016) and the Deliverable D2.1. Since, the modelling of the slave electrical heat (SEH) and the ultimate heat sink (UHS) have not been described for ATHLET before and are relevant for the calculation of the benchmark, these components will be described in more detail.

5.3.1 Thermodynamic properties

The implementation of the thermodynamic properties of CO_2 is major challenge for the simulation of the complete system, especially if the liquid, vapour and metastable region and the transition to supercritical states is included. ATHLET mainly needs the thermodynamic properties as a function of temperature and pressure. For utilization of the five and six equation model, the density and the enthalpy as well as their derivatives are necessary. The computation of the thermodynamic properties should be continuous and smooth (Austregesilo, et al., 2016) to minimize the computational time because a major share of the calculation time results from the property calculation (Müller, 1991). The most accurate equation of state (EOS) for CO_2 was developed by Span and Wagner (1996). This EOS is a function of temperature and density and consists of many terms including transcendental functions. Consequently, it is computationally expensive to evaluate this EOS (Hofer, Buck, & Starflinger, 2019). So far, the properties have only been included for the supercritical region as functions of pressure and temperature using bi-cubic spline functions. However, these implementations showed inaccuracies especially close to the critical point. Therefore, a simplified version of the approach presented by Kunick (2017) is used to extend and improve the thermodynamic property data base. Instead of bi-cubic spline functions of pressure and temperature, quadratic splines as function of pressure and enthalpy are used because in these variables the properties can be fitted more accurately. A detailed description of the used approach will be given as soon as the implementation of the thermodynamic properties is finalized and tested extensively. This point is very important since a wrong implementation may lead to unphysical behaviour and instabilities in the simulations.

5.3.2 General description of the loop model

This chapter provides a description of the model of the sCO2-HeRo loop in PP circulation mode. This closed loop model is also used for the benchmark calculations and includes no compressor or turbine and no heat is input via the CHX. In Figure 32, the ATHLET model is shown. For simplicity, the bypass form the outlet of the UHS to the inlet of the pump is excluded (from the end of PIPE1_BY to the start of PIPE4_BY), because it is also not used in the cycle simulations shown in this deliverable and valve 27 was always closed. The air side is at the same height as the CO_2-side of the UHS and only shown higher due to drawing purposes. The loop has been described in detail before, therefore, only the points important for the model are mentioned here. The SEH and the UHS are each divided into 25 subvolumes. The subvolumes of the pipes are selected in a way that the value at the measurement position in the experiment can be extracted. For this, it is important to know, that the pressure in the control volume is the average between inlet and outlet. In general, the number of subvolumes are reduced as far as possible to increase the stability of the simulation. However, for the UHS and the SEH the number of subvolumes should not be decreased too far because then the effect of varying

properties and the temperature profile cannot be caught anymore. The pump is just added to the end junction of PIPE_4_BY. In terms of UHS and CHX only one flow path (pipe or channel) is modelled which means that all paths are treated equally.

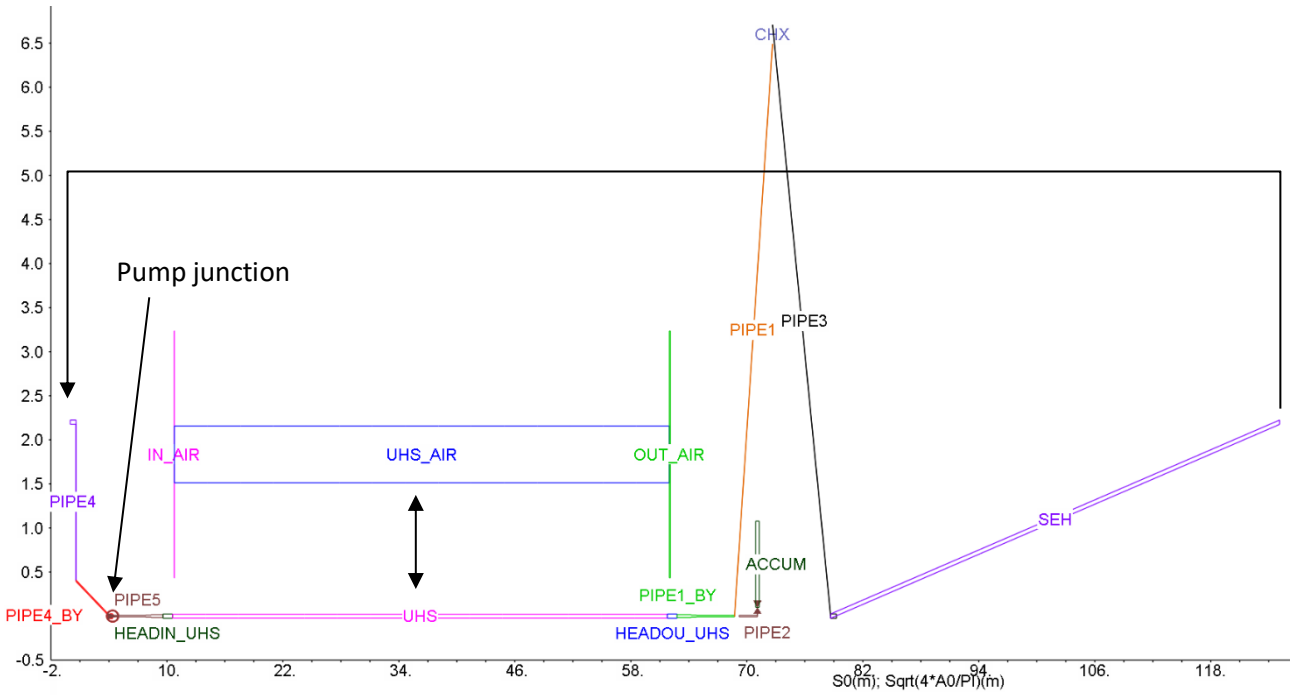

Figure 32 : ATHLET model of the PP circulation loop

Except for the valve at the accumulator inlet and the valves in the bypass, no valve is modelled explicitly, because the other valves are kept in the same position in the investigated time periods in the experiment. Therefore, the form loss coefficient of the valves in the pipes can be directly added to the other form loss coefficients caused by bends and elbows. The boundary conditions which must be specified during the simulation are the volumetric flow rate at the pump inlet, the electrical power of the SEH and the air volumetric flow rate at the outlet of the UHS and air enthalpy at the inlet of the UHS. Details about the boundary conditions are given in the next chapters together with the description of the components.

As it is mentioned in the next subchapter, no air-flow is allowed during the steady state calculation in ATHLET. Additionally, it is challenging to get a convergence of the steady state calculation of the SEH or UHS even with no modelling of the air side. Therefore, the selected approach to start the simulation is that the start point of the simulation will be approached during the transient calculation phase in ATHLET. Thus, the cycle is initialized with a certain pressure and temperature and a zero mass flow rate for all components. In order to have no heat transfer in the UHS, the temperature on the air-side must be the same. In the SEH, the power is set to a value almost equal to zero, to also have no heat transfer there. The value cannot be exactly zero because during the transient calculation the power of the SEH is calculated from this “zero-power” multiplied by a factor which is given via a GCSM signal. The initial pressure and temperature define the fill mass of the cycle. With the known mass in the cycle, either temperature or pressure can be chosen freely and the other parameter is fixed. Since, the temperature of the air-side must also be specified, it is easier to fix the temperature. In order to have a starting point which is far from the critical point for the relevant fill masses, a high starting temperature of 70 °C is selected. A starting point far from the critical point is beneficial because this speeds up the ramp up of the flow rates and power. For various analysis from the same starting point in the experiment also the restart option can be used if this transient has been calculated once. Due to the high

thermal mass of the SEH, it takes a long time to get all parameters stable. In all analysed cases so far, a time of 15000 s was more than sufficient. At the moment, this normally takes only a few minutes in ATHLET.

5.3.3 Ultimate Heat Sink (UHS)

In ATHLET air is available as a non-condensable gas (NCG) but not as a separate working fluid. Therefore, the air side can be modelled by specifying water with 100 % air content as working fluid. However, during the steady state no air flow is allowed. Therefore, the simulation of the heat sink has to start from an isothermal state with no heat transfer. This is also a good option for the whole cycle because as soon as heat transfer to CO_2 is modelled, it becomes challenging to get a steady state solution. This approach will be discussed in more detail in the chapter 7.

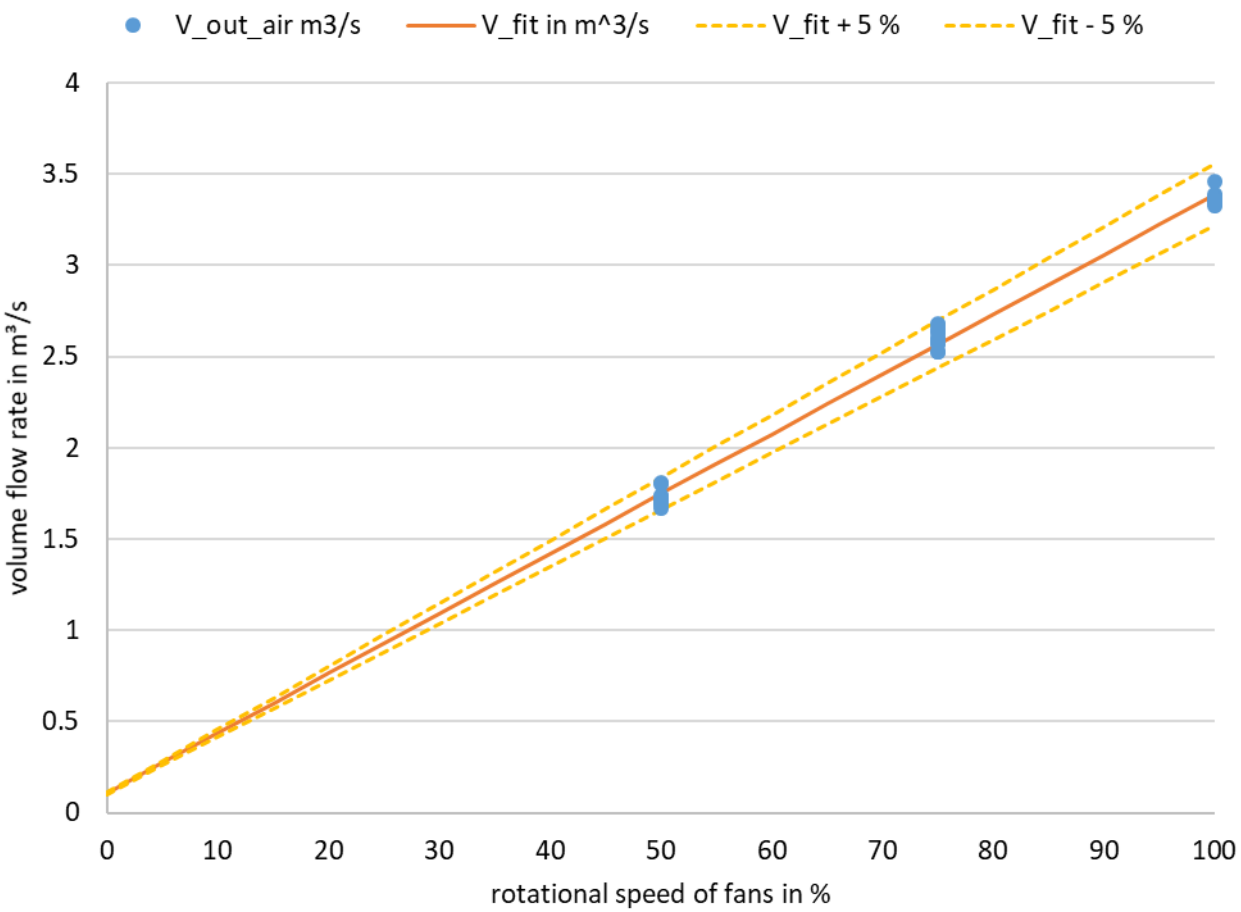

Figure 33 : Linear extrapolation of the outlet volumetric air flow rate as a function of fan speed of one UHS

Geometrically, the UHS is the most complex heat exchanger in the cycle with fins on the air side and a mix of counter-current and cross-flow. However, Vojáček et al. (2019) showed that it is sufficient to model the UHS as counter-current flow arrangement. In his work, heat transfer correlations as well as an experimental and numerical analysis of the heat exchanger is provided. However, the analysis covers only fan speeds from 50 % to 100 % and in the glass model experiments the fan speed is lower most of the time. Since, the volume flow rate at the outlet of the UHS shows a linear dependence on air flow rate, it is extrapolated down to lower fan speeds, as shown in Figure 33. The fit intersects the y-axis at a volumetric flow rate of 0.11 m³/s. This is acceptable because a certain flow will develop at 0 % fan speed due to natural convection. However, it needs

closer evaluation if this value is reasonable. In ATHLET, the air mass flow rate at the inlet of the UHS can be calculated by a multiplication with the outlet density, which can be extracted with a GCSM signal.

In addition to the volumetric flow rate, the heat transfer coefficient needs to be examined. For high fan speeds the equation given by Vojáček et al. (2019) and also by VDI (VDI Wärmeatlas, 2013) is used. It is a Nusselt correlation derived from experimental data for staggered fin arrangement which considers the ratio between the total heat transfer area on the air side and the outer surface of the pipes including the surface which is covered by fins. In a next step a fin efficiency η is considered, which is set to 0.95 in accordance with Vojáček et al. (2019). The Nusselt number and the heat transfer coefficient can be calculated from

$$Nu_d = 0.38 Re_d^{0.6} Pr^{1/3} \left(\frac{A_{total}}{A_{pipes}}\right)^{-0.15} \tag{20}$$

$$\alpha = \frac{Nu_d \lambda}{d_o}\left(1 - (1-\eta)\frac{A_{fins}}{A_{total}}\right). \tag{21}$$

The index “d” means that the Reynolds and Nusselt number are calculated with the outer diameter d_o of the pipes. It is also important to consider the higher air velocity inside the heat exchanger because the flow area is partly blocked by the fins. The equation is valid down to $Re = 1000$. However, at low fan speeds considerably lower Reynolds numbers are reached. First, it was tested down to which Reynolds number the equation still gives good results. For lower Reynolds numbers a cosine shape interpolation, which is by default available in ATHLET, was chosen to interpolate between a constant value and the current value which is provided by the correlation. The interpolation is performed between a Reynolds number of 100 and 350. At lower Reynolds numbers the Nusselt number of 1.3 is kept constant. This lower value and the lower bound of the Reynolds number must be always considered together because the volumetric flow rate at 0 % fan speed determines the minimum Reynolds number. The boundary values for the Reynolds number and the constant Nusselt number were determined to get a good fit of different experiments which are shown later. The resulting air side heat transfer coefficient at the minimum Reynolds number lies slightly below the range of the heat transfer coefficient which can be calculated from a correlation for natural convection (VDI Wärmeatlas, 2013). The heat transfer coefficient for a film temperature of 35 °C and an air outlet temperature of 50 °C is exemplarily shown in Figure 34. The general applicability of the model needs further examination because, like mentioned before, cross-flow influences are not considered in the simulation.

The calculated heat transfer coefficient refers to the total heat transfer area on the air side. In ATHLET, there are no heat conduction objects (HCO) which include fins. Therefore, the air-side heat transfer coefficient must be multiplied by the ratio between the total heat transfer area and the heat transfer area of the HCO. For the UHS the natural selection of the HCO would be a hollow cylinder which corresponds to the pipe wall. However, then the heat transfer area of the HCO is given by the geometry of the pipe. Since, the bends of the pipes are located outside of the air flow almost no heat transfer occurs there. In this case, 44.8 m of one pipe are located inside the air flow and 6.4 m outside. In order to get the correct density distribution in the UHS, these 6.4 m are not added to the ends of the UHS but rather the HCO selection is adapted. A plate shape HCO is chosen because it enables to choose the heat transfer area freely equal to the value of the inner pipe surface area which corresponds to the length of 44.8 m. The thickness of the plate is selected equal to the pipe thickness. In order to get the real transient behaviour of the UHS, the density of the HCO must be artificially adapted to match the real mass of the UHS.

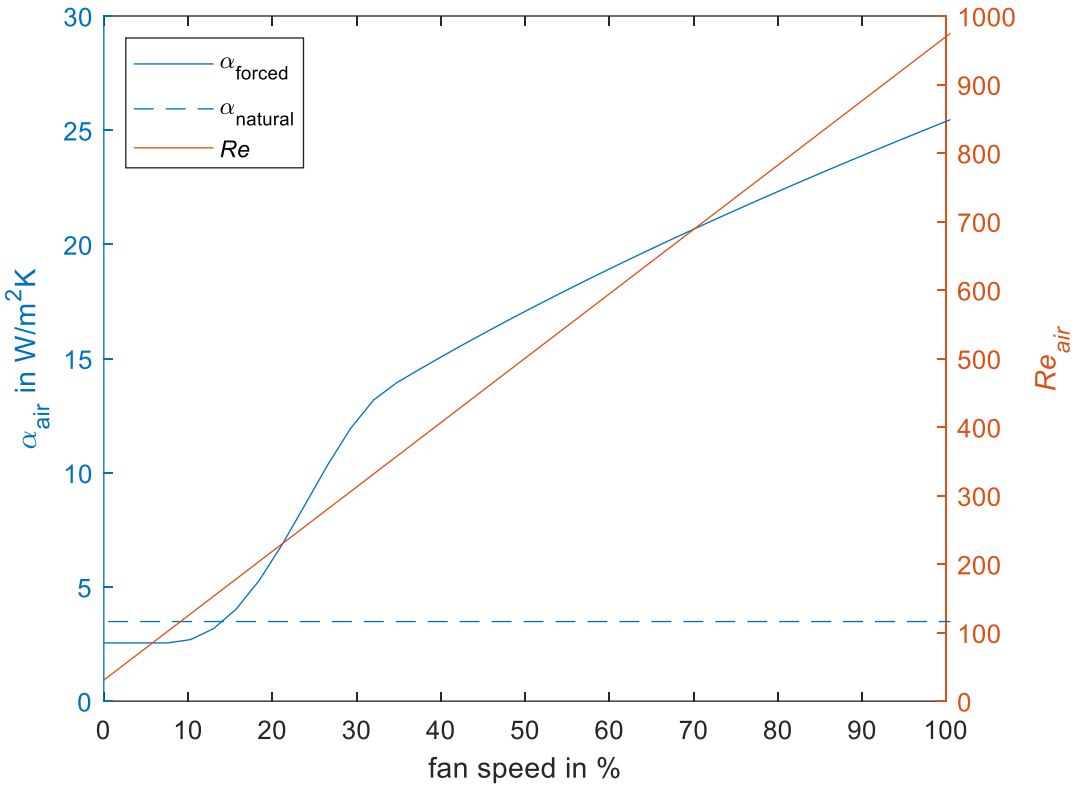

Figure 34 : Heat transfer coefficient on the air side for a film temperature of 35 °C and an air outlet temperature of 50 °C as a function of fan speed

5.3.4 Slave electrical heater (SEH)

Since ATHLET is a one dimensional thermal-hydraulic system code, only a simplified model of the SEH can be applied. In ATHLET, components are composed of thermo-fluiddynamic objects (TFOs) and heat conduction objects (HCOs). The CO_2 flow is modelled with a certain number of TFOs and the wall with HCOs with several layers. In general, the number of TFOs is a trade-off between simulation accuracy and computation time and stability. For the simulation of just one component, the simulation time is no issue. Therefore, a pipe, divided in 50 subvolumes, is selected for these first simulations in order to adequately catch the effect of the varying CO_2 properties close to the critical point. For the cycle calculations the number of subvolumes is reduced to 25 to improve the stability and the calculation time. In ATHLET, it is not allowed that one HCO is connected to several TFOs. In order to consider axial heat conduction in the pipe wall, the heat conduction between adjacent HCOs is switched on. Each TFO is connected to one HCO, which is shaped like a plate and consists of several layers. The plate shape was chosen to receive the same heat transfer area for the inner tube wall and the heating elements since these areas are similar as described above. The plate width is chosen equal to the tube inner perimeter and the length is defined by the number of TFOs. Except for the thickness, each layer has by default the same dimensions. The thickness of the first layer, which represents the pipe, is calculated from the pipe mass, which results in 6.16 mm. The second layer with a thickness of 57.69 mm represents the aluminium and the remaining steel is represented by a layer with a thickness of 11.55 mm. In the last layer, a heat source is added, which represents the electrical power input. This is not completely correct, because the third layers includes all the remaining steel mass and not only the heating elements. Still, this seems to be the best way to model the SEH, because ATHLET only allows three different material layers. In reality, the axial heat conduction, especially in the aluminium, is higher than in the simulation because the SEH is a compact

component, as described before, and not just a long pipe like in the model. In the model the aluminium is stretched over the whole length of the pipe, which is 46.5 m, instead of only the height of the heater, which is 2.2 m. To account for that fact, the thermal conductivity of the aluminium is artificially increased by a factor of 21, which results from dividing 46.5 m by 2.2 m. This reduces also the radial thermal resistance of aluminium. However, the effect on the radial heat transfer is small, because the other thermal resistances, especially the pipe wall and the heat transfer to the fluid, still limit the overall radial heat transfer.

5.3.5 Compact heat exchanger (CHX)

Concerning compact heat exchangers the standard approach for modelling heat exchangers in ATHLET has been selected so far. It implies that only one representative channel pair is modelled and multiplied with the number of channels. To account for the pressure losses in the plenum of the heat exchanger from loss coefficient are added to the inlet and outlet of the channel. The approach was described in more detail and tested successfully by Hofer et al. (2019). In order to simulate the experiments of the glass model, the simulation of NCG and possibly drift flux models must be tested and applied in the future.

5.3.6 Compressor and turbine

The ATHLET version 3.2 contains an axial turbine model which is based on Stodola`s cone law, a helium compressor model and a model for dynamically controlling the speed of the turbomachinery (Austregesilo, et al., 2016). A new model for radial $CO_2$ turbomachinery is described by Hofer et al. (2019) and included in the current developer`s version of IKE. A brief description is presented here, for more details please refer to the cited paper. The basic concept of the model is the same as for the axial turbine model. The lumped parameter model provides the pressure difference Δp and the power P, which are sink or source terms in the momentum and energy conservation equation. The difference to the axial turbine model is that this model uses performance maps, which must be input by the user, to determine Δp and P. In order to account for the real gas behaviour of CO_2, an advanced similarity approach (Pham, et al., 2016) is used in a slightly modified form. The performance map generated from experimental data or CFD simulations is transposed to a dimensionless map. The x- and y-axis are the axial and tangential Mach numbers, given by

$$Ma_a = \frac{\dot{m}}{\rho c D^2} \tag{22}$$

$$Ma_\theta = \frac{ND}{c}, \tag{23}$$

where N is the rotational speed, D the impeller diameter and c the speed of sound. All thermodynamic parameters are determined for the inlet condition. For sCO_2 the speed of sound c should be derived using the entropy

$$c = \sqrt{\left(\frac{\delta p}{\delta \rho}\right)_s} \tag{24}$$

Therefore, the entropy would be required as additional property for CO_2 in ATHLET. Alternatively, the speed of sound can be directly calculated from an equation of state, e.g. if REFPROP is implemented. On the z-axis of the performance map the dimensionless isentropic enthalpy difference $\Delta h_{is}{}^*$ or the corrected pressure

ratio π_c and the efficiency η can be presented. The equation for the dimensionless isentropic enthalpy difference is

$$\Delta h_{is}{}^{*} = \frac{\Delta h_{is}}{c^2}. \tag{25}$$

In the end the pressure difference Δp and the power P, which are required for ATHLET can be calculated. In the future, this model need to be extended to account for leakage losses observed during the experiments. Additionally, the performance maps must be validated and the model needs to be tested together with the dynamic speed control available in ATHLET.

5.3.7 Piston Pump (PP)

In ATHLET one simple and more detailed pump models are available (Austregesilo, et al., 2016). For the simple pump model the pressure difference over the pump is controlled via a GCSM signal and the power of the pump which is added to the fluid is the hydraulic power. The detailed models were developed for centrifugal pumps and need a lot of input data like performance curves. Due to the fact that a PP is used in the experiment, the simple pump model is applied in combination with a PI-controller which is used to keep the volumetric flow rate at the pump inlet constant. Consequently, not the speed of the pump is given as a boundary condition but the volumetric flow rate. For modelling purposes it is important to note that the pump model is a junction model which increases the pressure at the specified junction and adds half of the power to the right and the left subvolume, respectively. To achieve stable and fast simulations, the pump volume should not be modelled explicitly as separate subvolumes but rather added to the related pipes because small subvolumes may lead to problems in the simulation.

5.3.8 Pressure Vessel (PV)

For water different accumulator models are available. They mainly differ in the simulation of the non-condensable gas (NCG) (Austregesilo, et al., 2016). So far, CO_2 cannot be simulated together with NCGs. Therefore, only the accumulator model, where nitrogen is treated as an ideal gas with no heat exchange with the CO_2, can be applied. Due to the common applications in the NPP, this model only allows discharging of the accumulator. Furthermore, the line to the accumulator must be closed by the user with another valve before the accumulator is empty because otherwise the simulation will stop. Possibly, the code of the simple accumulator model can be slightly modified to allow both, filling and discharging. However, first test simulations showed an instable behaviour, when the pressure at the inlet of the accumulator varies slightly around the level of the filling pressure. Therefore, further investigations are required. For the transient part of the benchmark calculation, the discharging option is sufficient because the pressure at the PV inlet is continuously decreasing.

6 Selected simulation results

6.1 CATHARE

6.1.1 CATHARE results for steady state

The results of the CATHARE simulation for flowrate, temperature and pressure are shown in Figure 35, Figure 36 and Figure 37, respectively. The steady state is reached after about 7000 s of physical time.

The first step of the CATHARE simulation is the initialisation. Pressure, temperature and flowrate are imposed on a given node and are propagated on the entire mesh of the circuit. After this step, a transient calculation is performed from this initialisation. It leads to a steady state solution in our case. During the initialisation step, we have performed the assumption that the heat exchange in the SEH and the UHS are not considered. They are reactivated for the transient calculation. This may explain the important difference in the results between the beginning of the simulation and the converged results.

The CHX heat exchanger is disabled as in the experiment. Therefore the input and output temperature are practically similar in Figure 36. The SEH increases the temperature by about 5 °C and decreases pressure by about 0.1 bar because of vertical tube and pressure losses. In our case, the pump increases also the temperature of a few degrees but we have to keep in mind that the modelling of the pump is a limit of our model. Finally, the UHS decreases the temperature by about 10 °C. All along the simulation the flowrate is imposed to a value of 0.31 kg/s by the pump which is a bit overestimated compared to the experimental value. Indeed the calibration of the pump was a difficulty in our model, as previously mentioned.

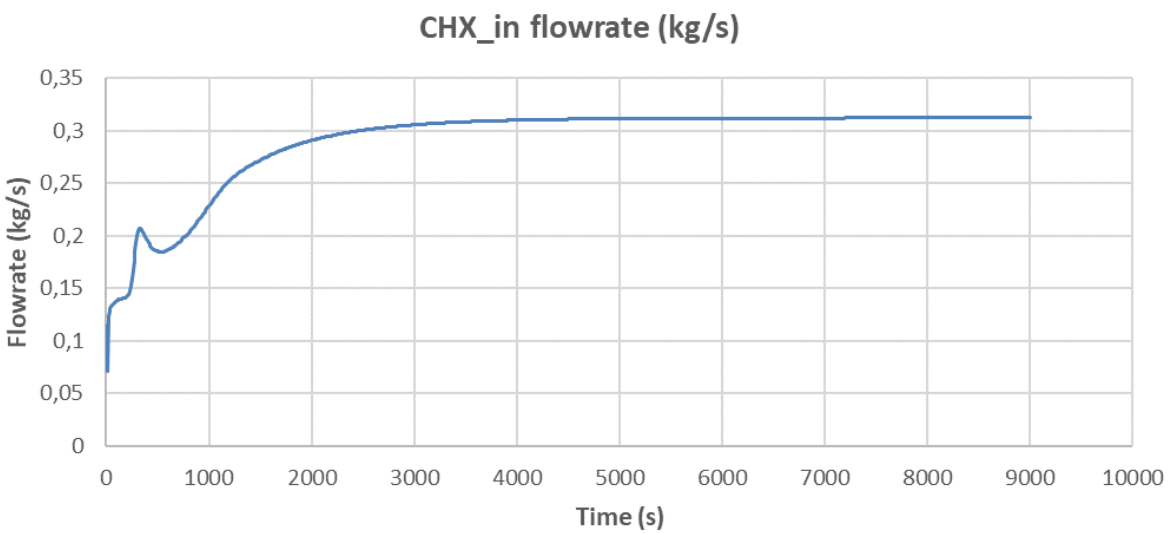

Figure 35: CHX flowrate

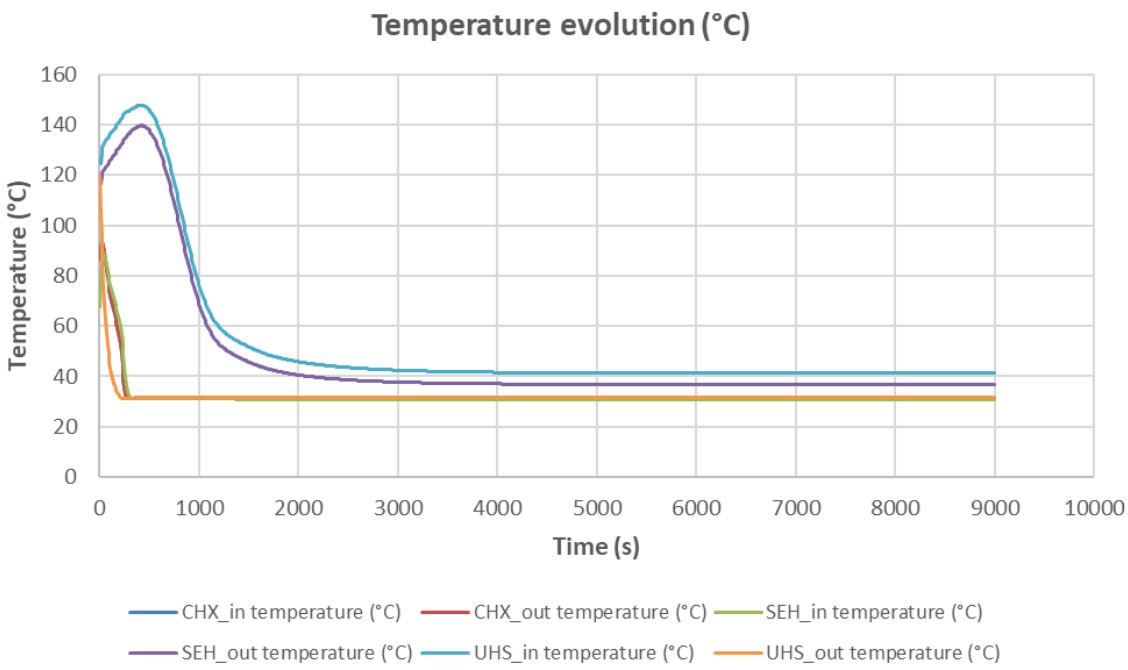

Figure 36: temperature evolution

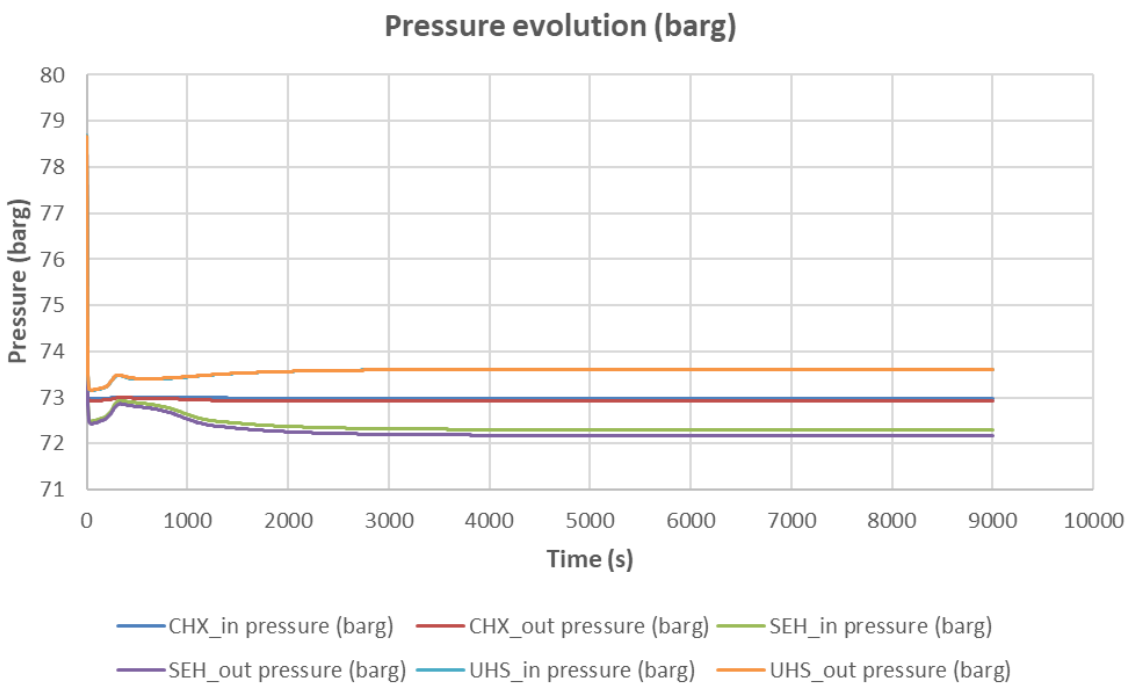

Figure 37: pressure evolution

6.1.2 Results comparison with experimental data for steady state

The CATHARE converged results are now compared to the experimental data for flowrate, temperature and pressure in the Figure 38, Figure 39 and Figure 40 respectively.

The flowrate steady state value from CATHARE is a bit overestimated compared to the experimental value. The pump definition and data setting in CATHARE is not really adapted for imposing a given volumetric

flowrate in the loop (as in the experiments). Therefore, a work has been performed to obtain the nearest flowrate from the experimental one but it should be continued to ameliorate the results.

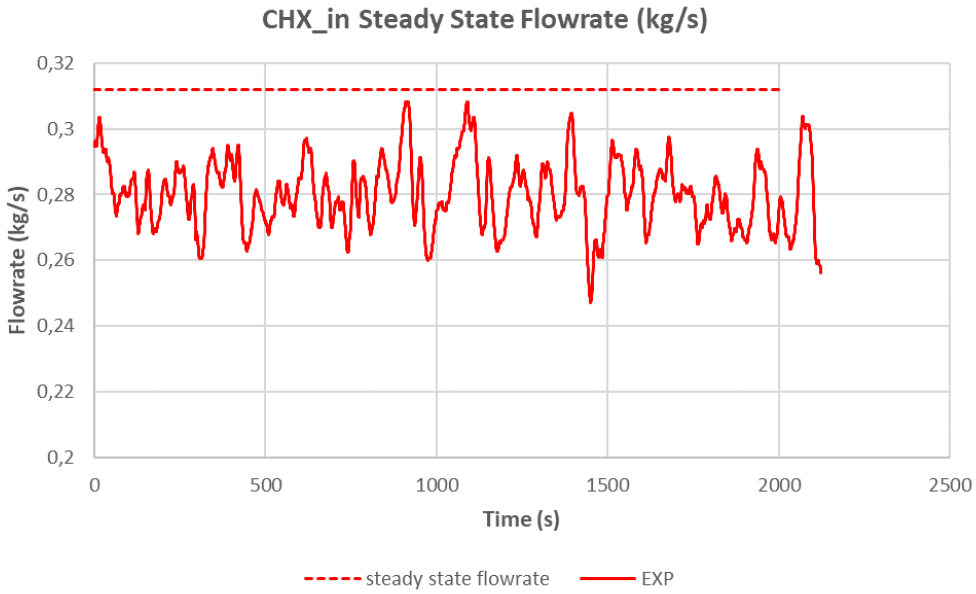

Figure 38: CHX flowrate comparison between CATHARE and experimental results

The simulated values of temperature at steady state for CATHARE in Figure 39 follow the same trend as the experiment. It seems that the cooling of the UHS is too excessive compared to the experiment. The modelling of the UHS in CATHARE is quite simple: the flow in the air loop is not modelled yet and only heat exchange coefficient and air temperature are considered for the heat flux calculation. Although two air temperatures are considered in order to take into account the air warming, it seems to be not sufficient to model accurately the UHS. A future work will be to simulate the air side with CATHARE and let the code calculate the temperature and heat transfer coefficient profiles.

The steady state pressures calculated by CATHARE in Figure 40 follow the same trend than the experimental data. However all the pressures are globally too low. This could be adjusted by changing the location of the pressure boundary condition. Indeed, the pressure boundary condition should be placed before the UHS where measured pressure is the highest of the loop. On the other hand, the improvement of the air side model for the air cooler will certainly help to increase the pressure levels in the circuit. Moreover an improvement on the pressure losses calculation in the loop of the CATHARE simulation should be investigated. Indeed the total pressure losses seem to be underestimated in CATHARE due to a lot of simplifications performed for the loop modelling (no singular losses, etc.). This lack of is particularly an evidence when considering the UHX component.

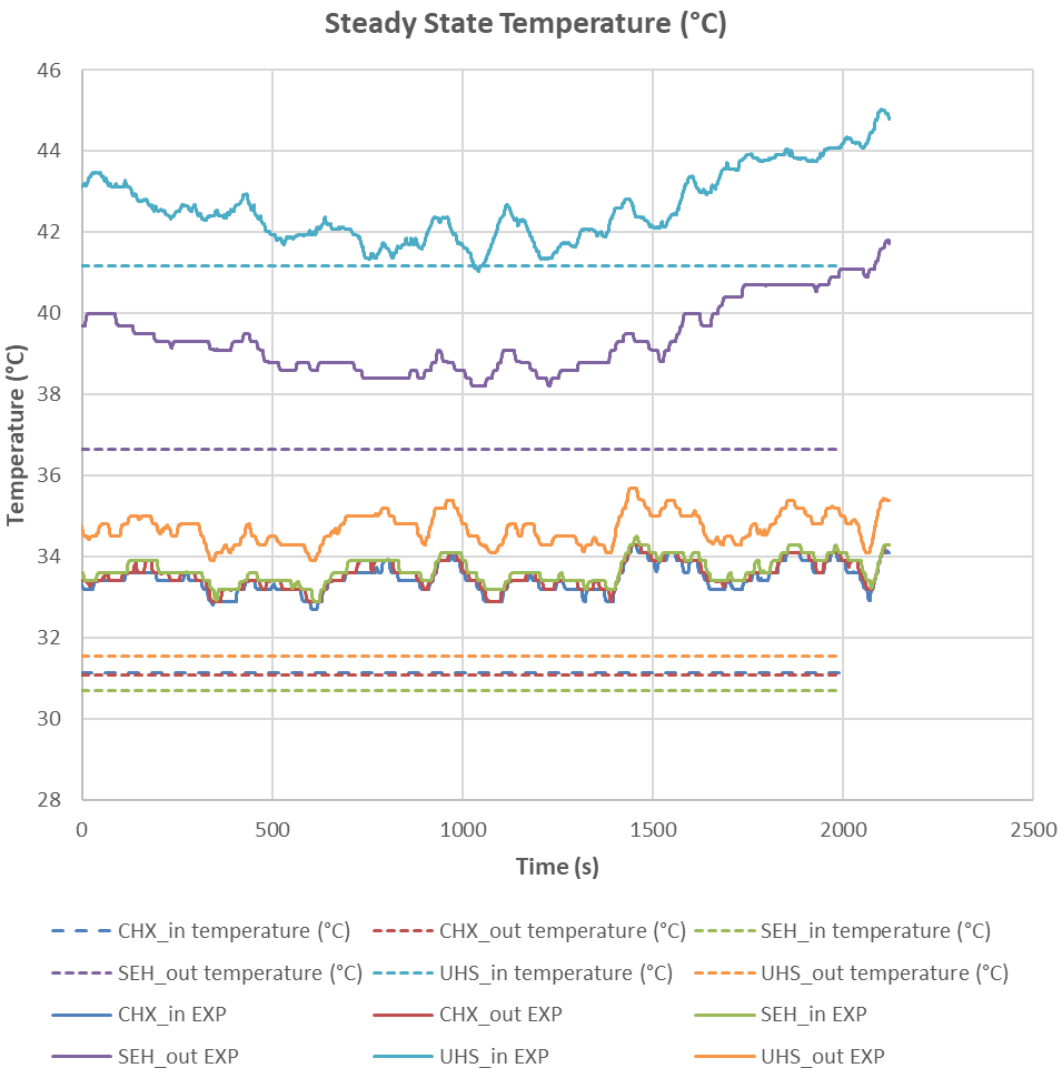

Figure 39: temperature comparison between CATHARE and experimental results

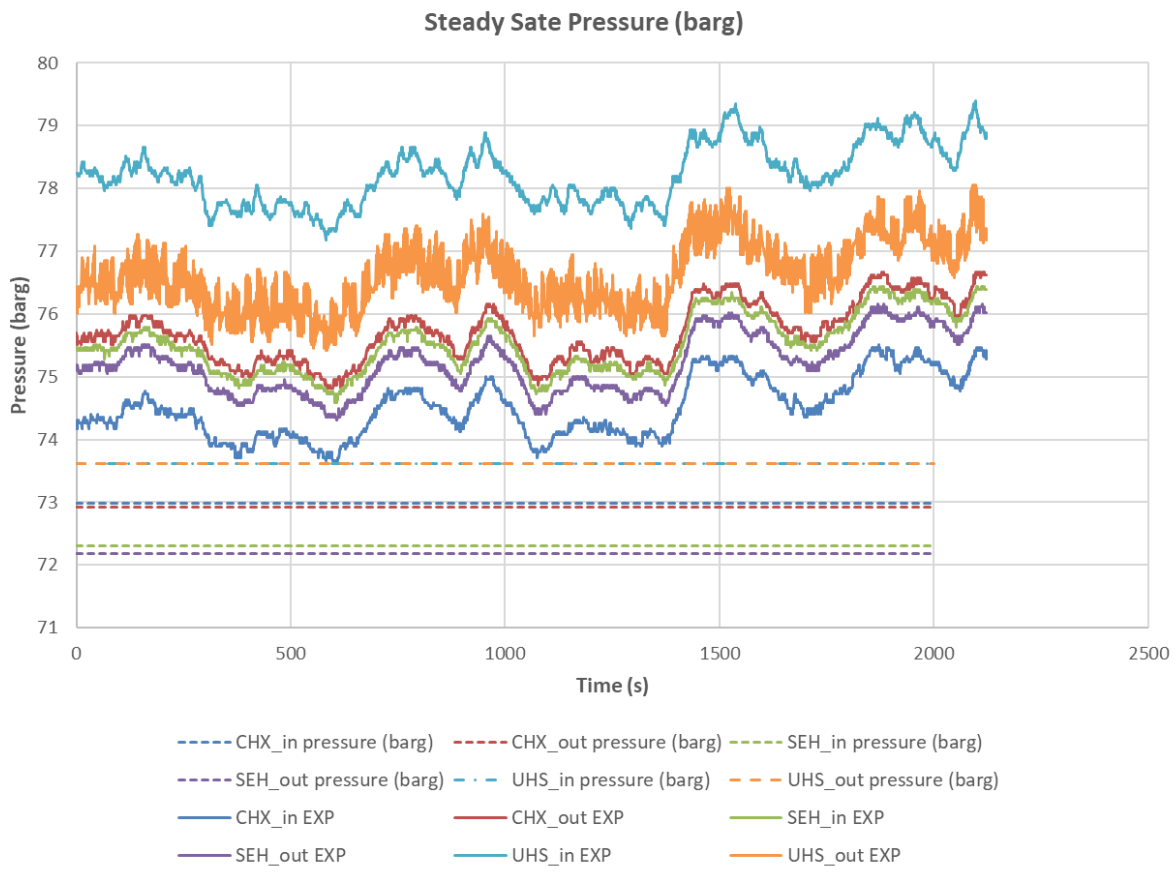

Figure 40: pressure comparison between CATHARE and experimental results

6.2 MODELICA

6.2.1 UHS model and CVR measurement comparison

As a first approximation, a constant value of 20 W/m^{2}K was used for the air side heat transfer coefficient. This UHS model was then compared with the measurement from August 2017 in CVR.

Each of 34 measured states was simulated as steady state in Dymola. Due to discontinuities of the measurements, dynamic behaviour of the UHS model couldn't be simulated. However, the steady state simulation corresponds quite well with the experiment until 50% of the fan speed. The largest deviations are on the CO_2 side (see Figure 42) but the values are within the tolerance given by the measurement uncertainty, which can be seen in Figure 42. The assumption about the constant heat transfer coefficient at the air side is too rough for the low fan speeds so for the future models fan speed shall be taken into account.

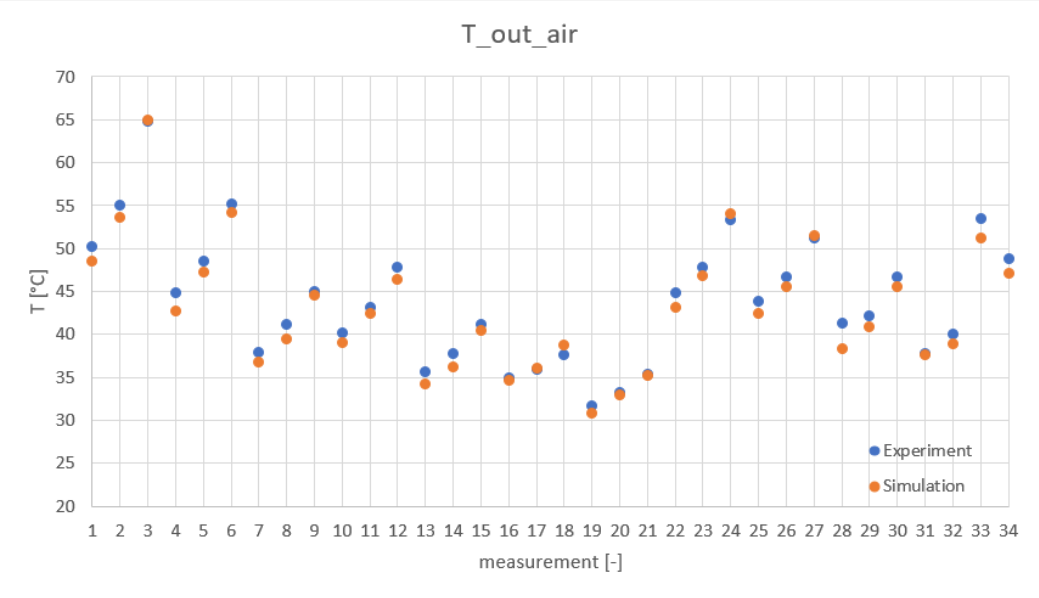

Figure 41**: Comparison of air outlet temperature** (CVR measurement)

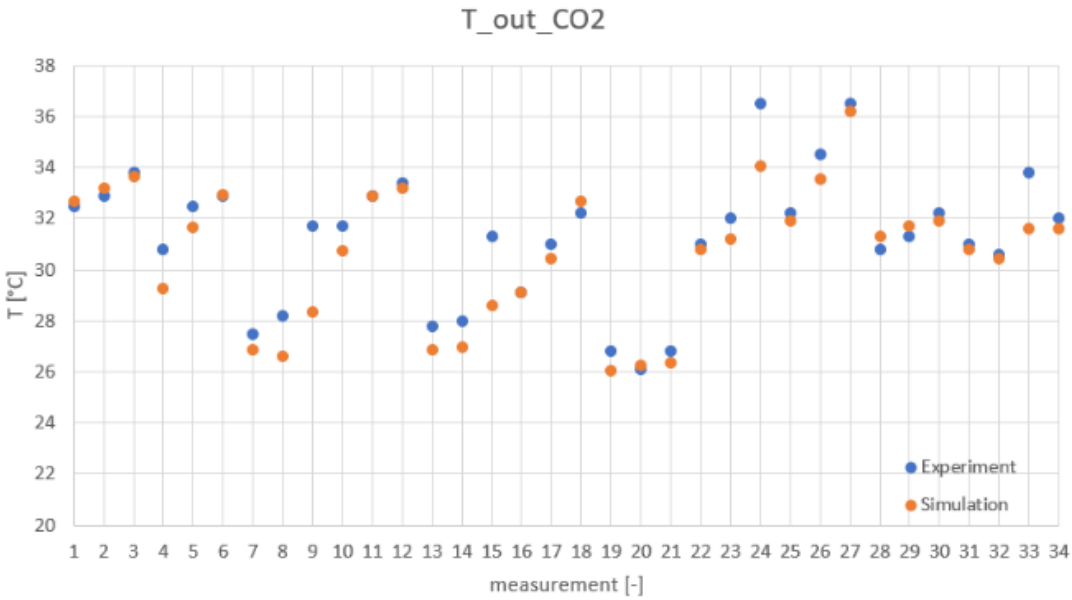

Figure 42**: Comparison of CO_2 outlet temperature** (CVR measurement)

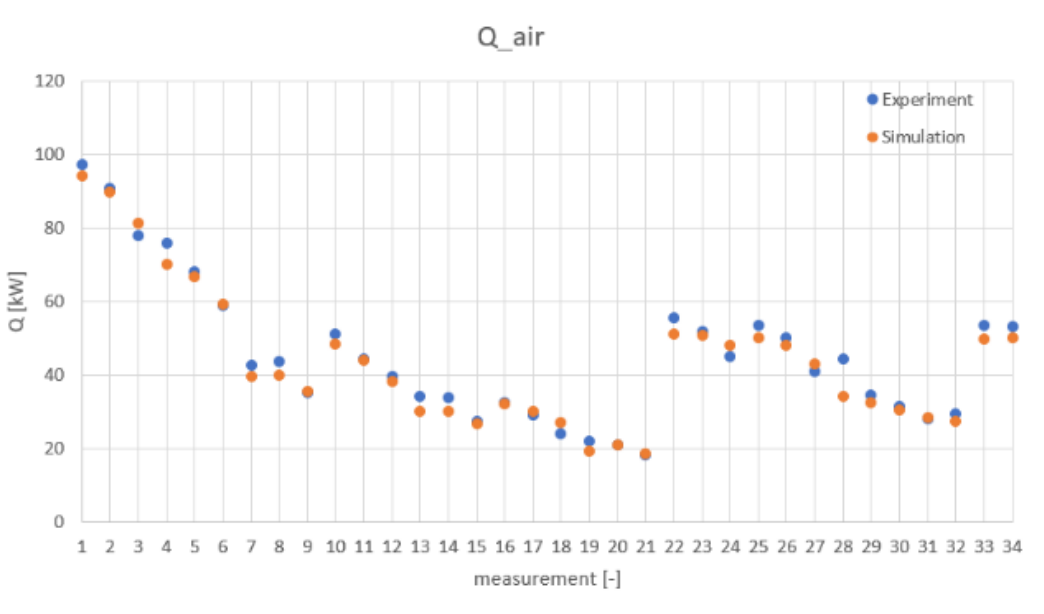

Figure 43**: Comparison of air heat** (CVR measurement)

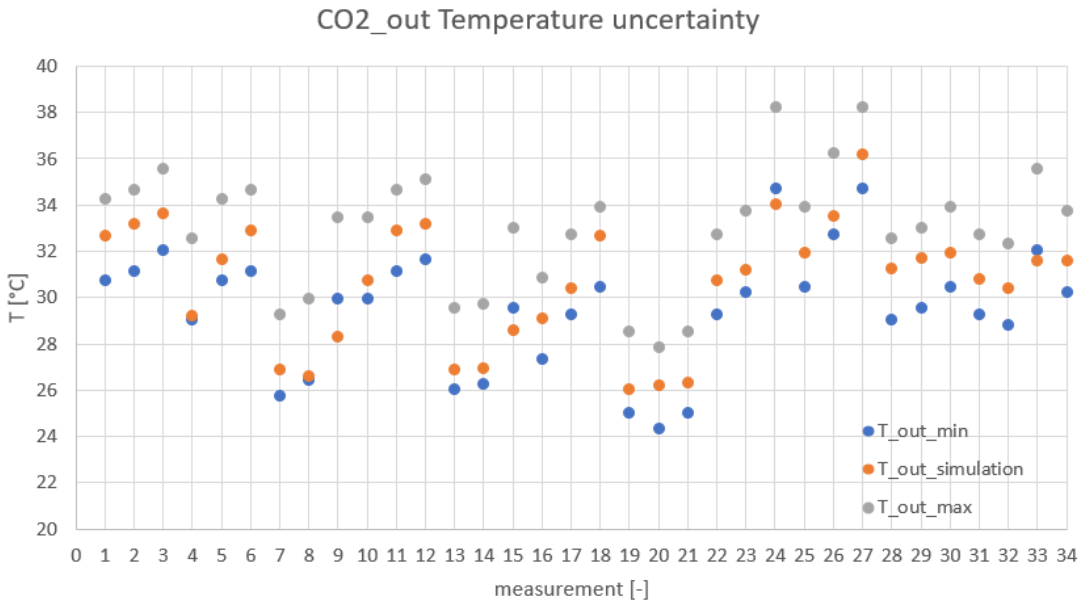

Figure 44**: Measurement uncertainty vs simulation** (CVR measurement)

6.2.2 UHS model for HeRo loop conditions

At the benchmark starting point the difference between air outlet temperature and CO_2 inlet temperature (3.5 °C) is too low - Figure 45. One aspect is probably overestimated heat transfer coefficient at the air side (now taken as a constant 20 W/m^{2}K), but there might be also problem with the air mass flow rate calculation. This was calculated as 1.14 kg/s at transient benchmark start. The uncertainty in the air mass flow calculation is entailed with the fact that ventilator inlet conditions depend not only on UHS air inlet temperature and fan speed, but also on the UHS heat load induced by the hot CO_2 flow.

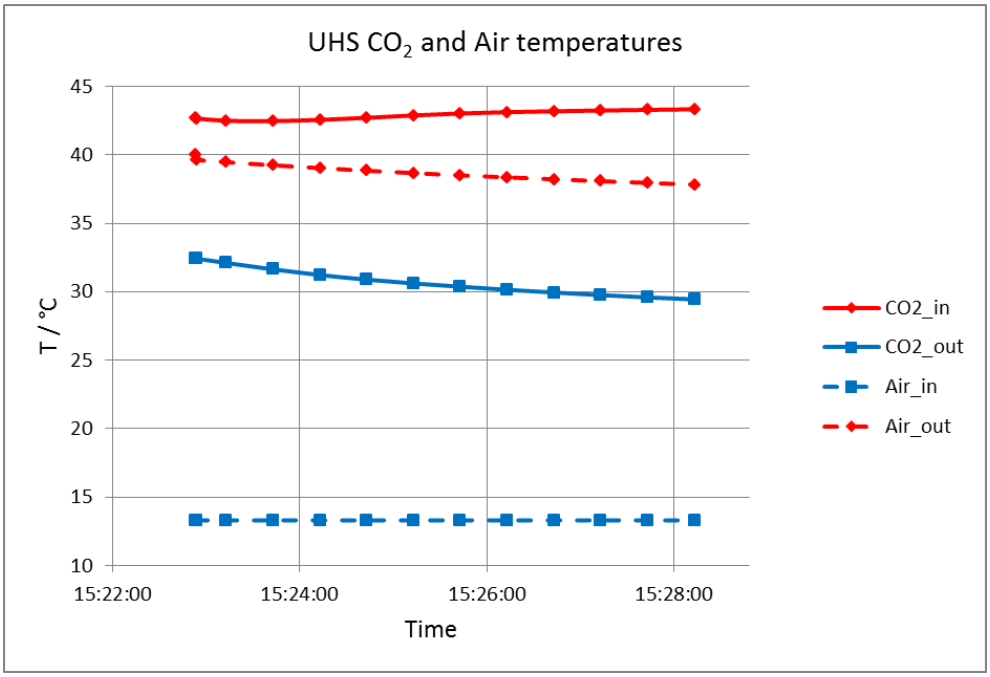

Figure 45: UHS temperatures (MODELICA)

6.2.3 SEH model for HeRo conditions

Below depicted figures show development over time for the SEH temperature, heat transfer coefficient and heat flow to CO_2 as a result of model simulation.

References to these figures are made also in 7.3. In the Figure 46, SEH internal temperatures development over time are visualized for different CO_2 fluid domains. Fluid domain 1 means the first 2.3 m of the CO_2 pipe as measured from the SEH inlet. During the transient inlet temperature falls, but outlet temperature is almost unchanged. This could be possibly explained by the increasing heat flow over time caused partly by increasing heat transfer coefficients within the first half of the SEH pipe (Figure 47) and partly by increased temperature difference between the wall and the fluid mainly at the first half of the heat exchanger. The area where pseudocritical temperature is being crossed is also visible (domains 5, 7, 10).

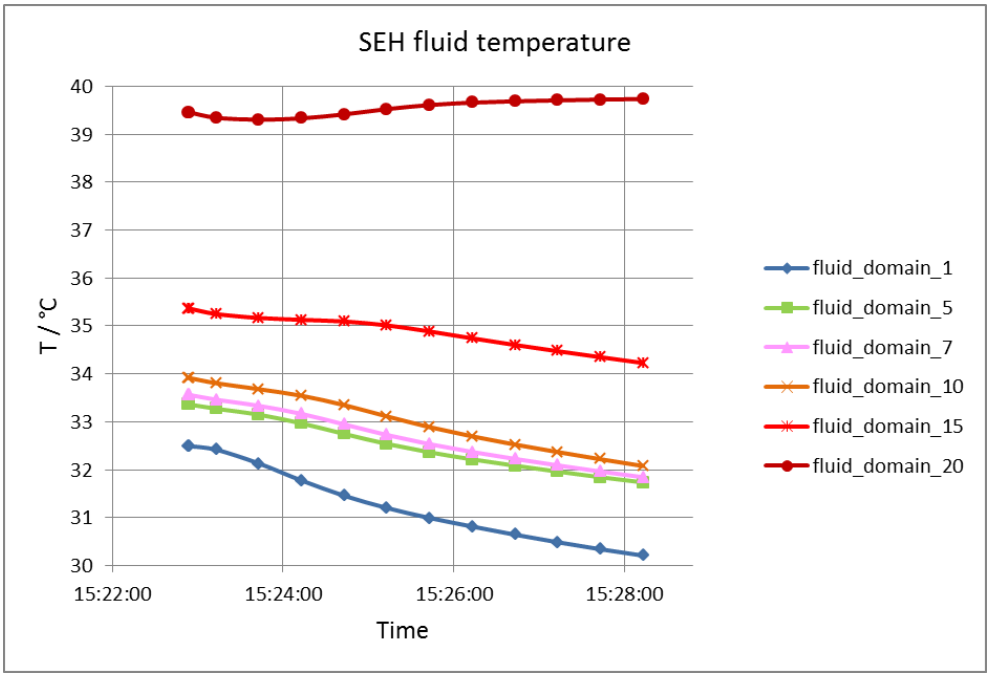

Figure 46: SEH internal temperatures (MODELICA)

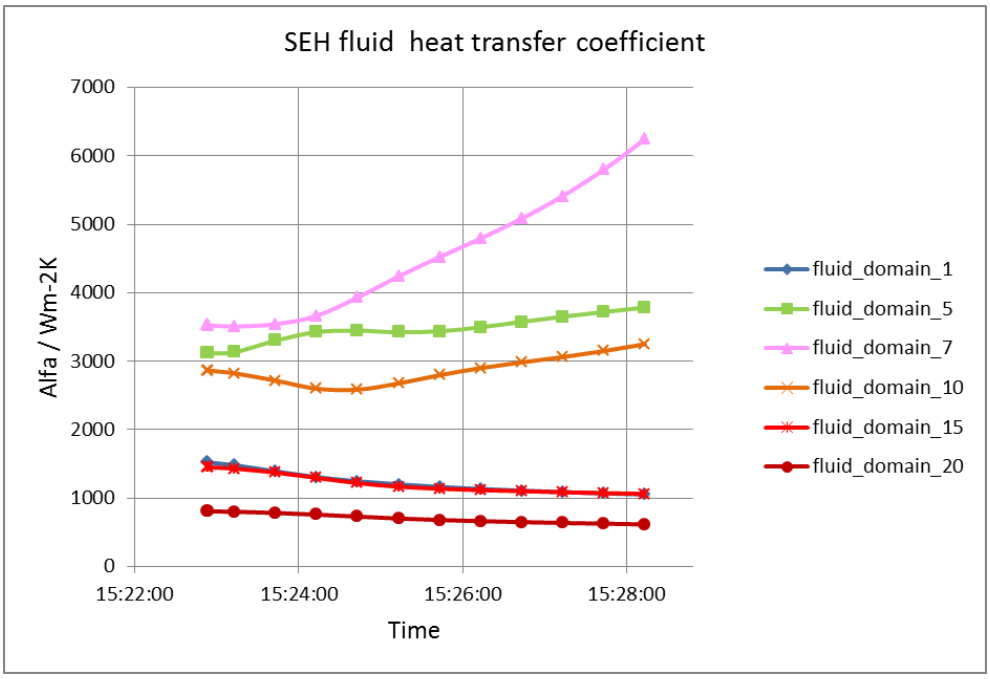

Figure 47: SEH internal heat transfer coefficients (MODELICA)

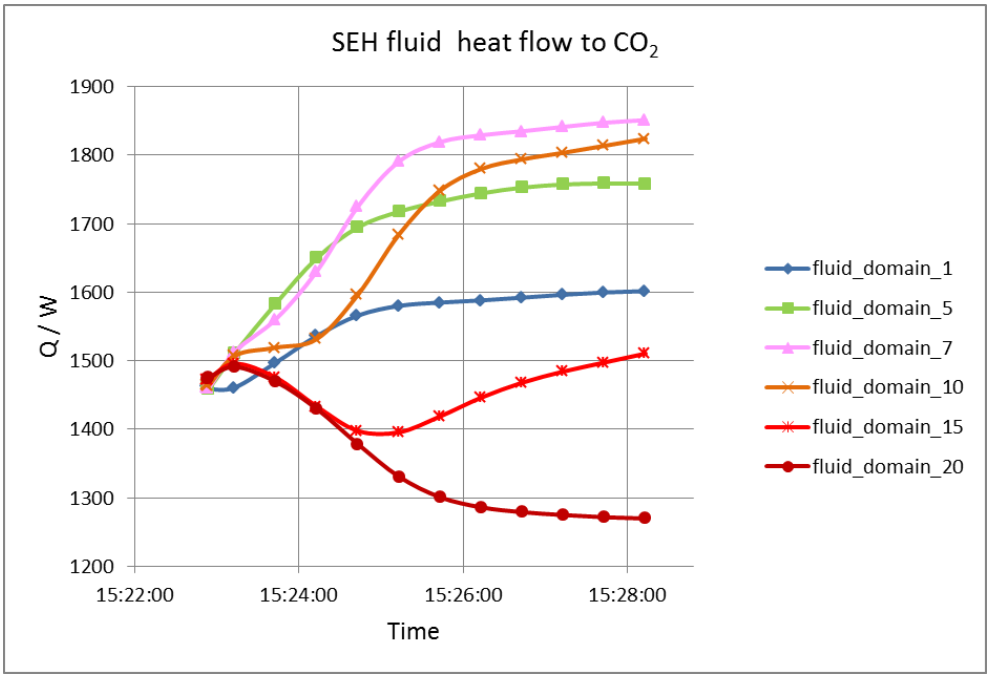

Figure 48: SEH internal heat flows (MODELICA)

6.3 ATHLET

6.3.1 Ultimate Heat Sink (UHS)

The UHS is modelled according to the specifications in chapter 5.3.3. At the CO_2-side the mass flow rate and enthalpy at the inlet and the pressure at the outlet is imposed. On the air side the inlet enthalpy is given, the outlet pressure is set to 1 bar and the inlet mass flow rate is calculated from the specified volumetric flow rate at the outlet of the UHS during the simulation.

As a first step, the transient experiments conducted by Vojáček et al. (2019) where recalculated. These experiments contain fan speeds of 50 %, 75 %, 100 % and 0 % in the end. The results shown in Figure 49 are in good agreement with the experiments. The lower air outlet temperature may be explained by the fact that the fan is not simulated in ATHLET. Thus, calculating the transferred power from the air-side values will overpredict the transferred power. However, in this case it is sufficient to compare the CO_2 outlet temperatures because the temperature difference between inlet and outlet is quite high for the first 1800 s and afterwards the transferred power cannot be determined reliably because the CO_2 outlet lies in the two phase region. The main difference occurs at 0 % fan speed and should be examined in more detail in the future. As mentioned before, the modelling of 0 % fan speed is related to the heat transfer coefficient and the volumetric flow rate occurring during natural circulation. These values may also be effected by other ambient conditions, like wind and humidity.

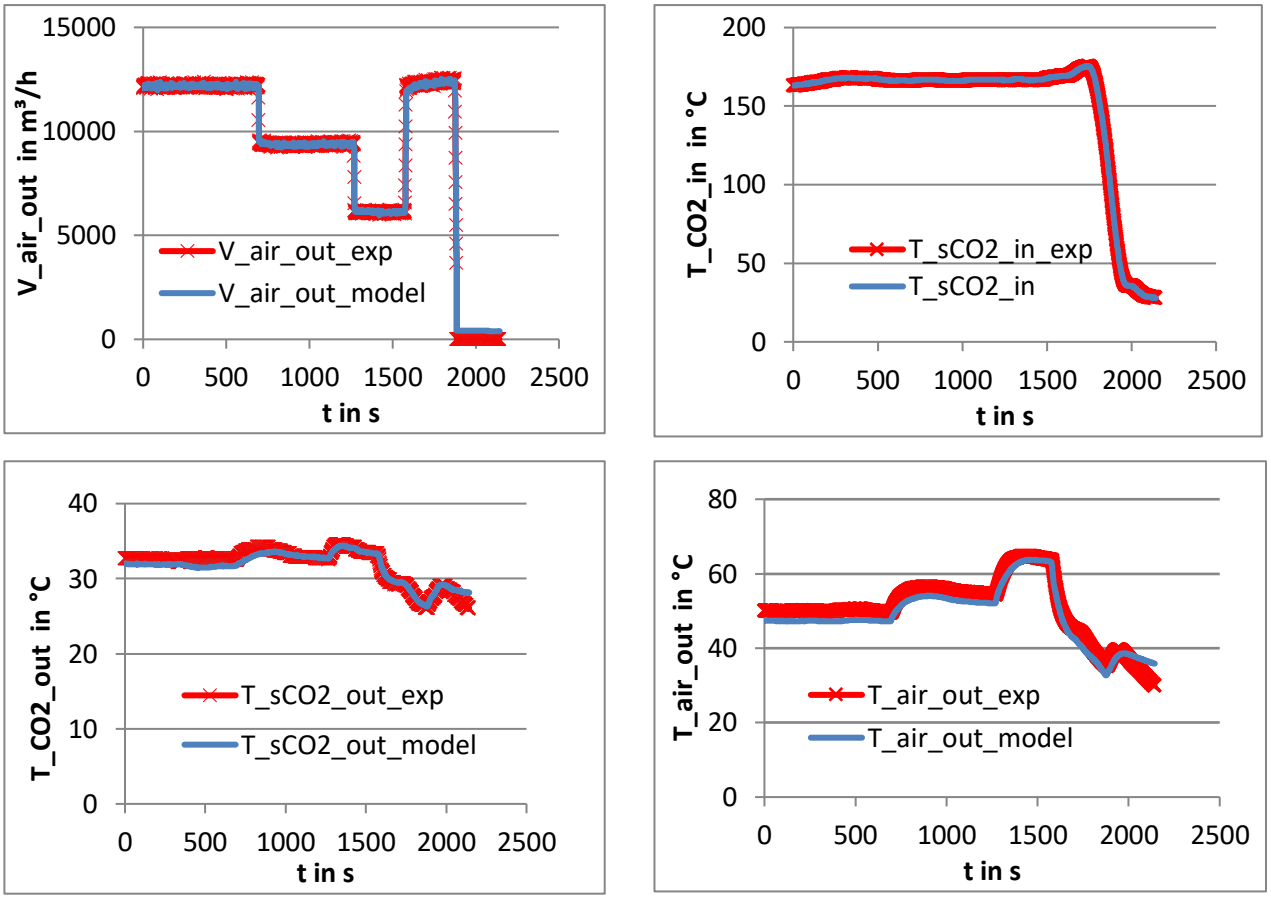

Figure 49 : Simulation of transient UHS experiments conducted by Vojáček at al. (2019) with ATHLET

As a second step, experiments from the glass model are simulated. At the glass model, the air parameters except the air inlet temperature are not measured. Therefore, only the CO_2-side measurements can be used for comparison. Since, the temperature difference between inlet and outlet is relatively low for most of the analysed cases and the outlet temperature may be close to the critical point, the transferred power should also be compared. It can be calculated reliably using the density measurement either at the compressor inlet or the CHX inlet depending on the current flow configuration.

The first experimental data set analysed is from the 14.06.2019 from 12:35 to 12:43. After 128 s the fan speed is increased from 10 % to 20 %. In contrast to the other cases, the CO_2 conditions were supercritical gas like with an inlet temperature between 60 °C and 67 °C. On this day no density measurement was available, however, the CO_2 outlet is not so close to the pseudocritical point, therefore, it is sufficient to compare the outlet temperatures. The temperatures agree very well as it can be observed from Figure 50.

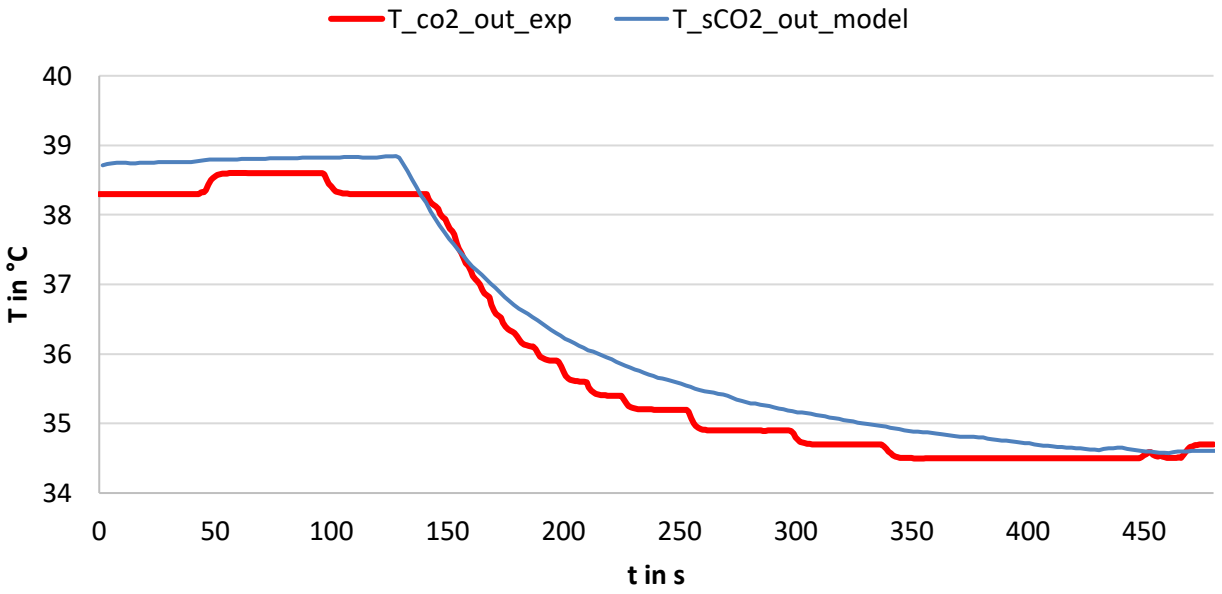

Figure 50 : Simulation of UHS fan speed increase from 10 to 20 %

The second data set is from the 25.09.2019 from 13:50 to 14:30. The fan speed is increased from 10 % to 15 % at 826 s, further increased to 20 % at 1807 s and shortly before the end of the simulation increased to 25 % at 2392 s. The simulation is stopped at 2400 s because the CO_2 pressure drops below the critical pressure. The comparison of the experiment and the simulation is shown in Figure 51. It should be noted that the pressure of the CO_2 ranging from 7.4 to 7.6 MPa is quite close to the critical point. The same holds for the temperature. Therefore, the power calculated from pressure and temperature is not shown because the result is probably very inaccurate. It can be observed that the model agrees well with the simulation except for some small difference in the transferred power during the simulation and a larger difference in the end. This larger difference should be examined further. However, it might be related to the oscillations in the cycle.

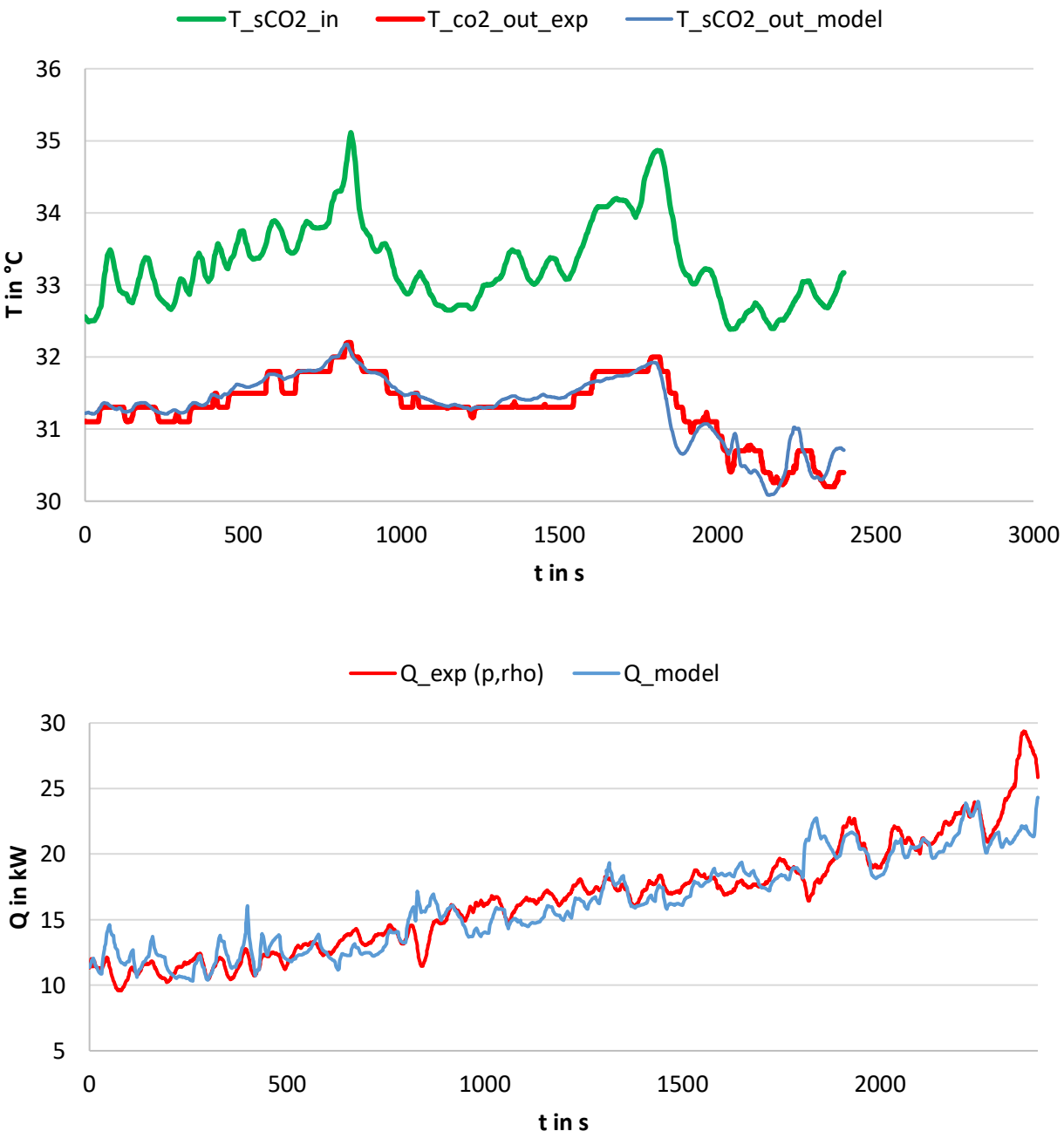

Figure 51 : Simulation of UHS fan speed increase from 10 to 15 % to 20 % (to 25 %), pressure is very close to the critical point

The last data set is the nearly steady state period before the transient part of the benchmark starts from 10.03.2020 from 14:47:30 to 15:22. In this case the fan speed is set to 15 % all the time and the outlet temperature is very close to the pseudocritical temperature. The comparison of the experiment and the simulation is shown in Figure 52. In the beginning the simulation agrees very well with the experiment. However, starting from around 650 s the simulation slightly over predicts the performance of the UHS. To match the starting point of the benchmark, the fan speed was adapted to 14.25 % in the second half of the cycle simulation which is shown in chapter 6.3.3. This small adaption is necessary because otherwise the difference between the simulation and the experiment sums up over time.

It can be concluded that the model agrees well with the simulation most of the time except for some slight inaccuracies. However, further experiments need to be analysed to prove the general applicability of the applied air-side correlation. Especially, experiments with higher fan speeds and fans switched off should be simulated.

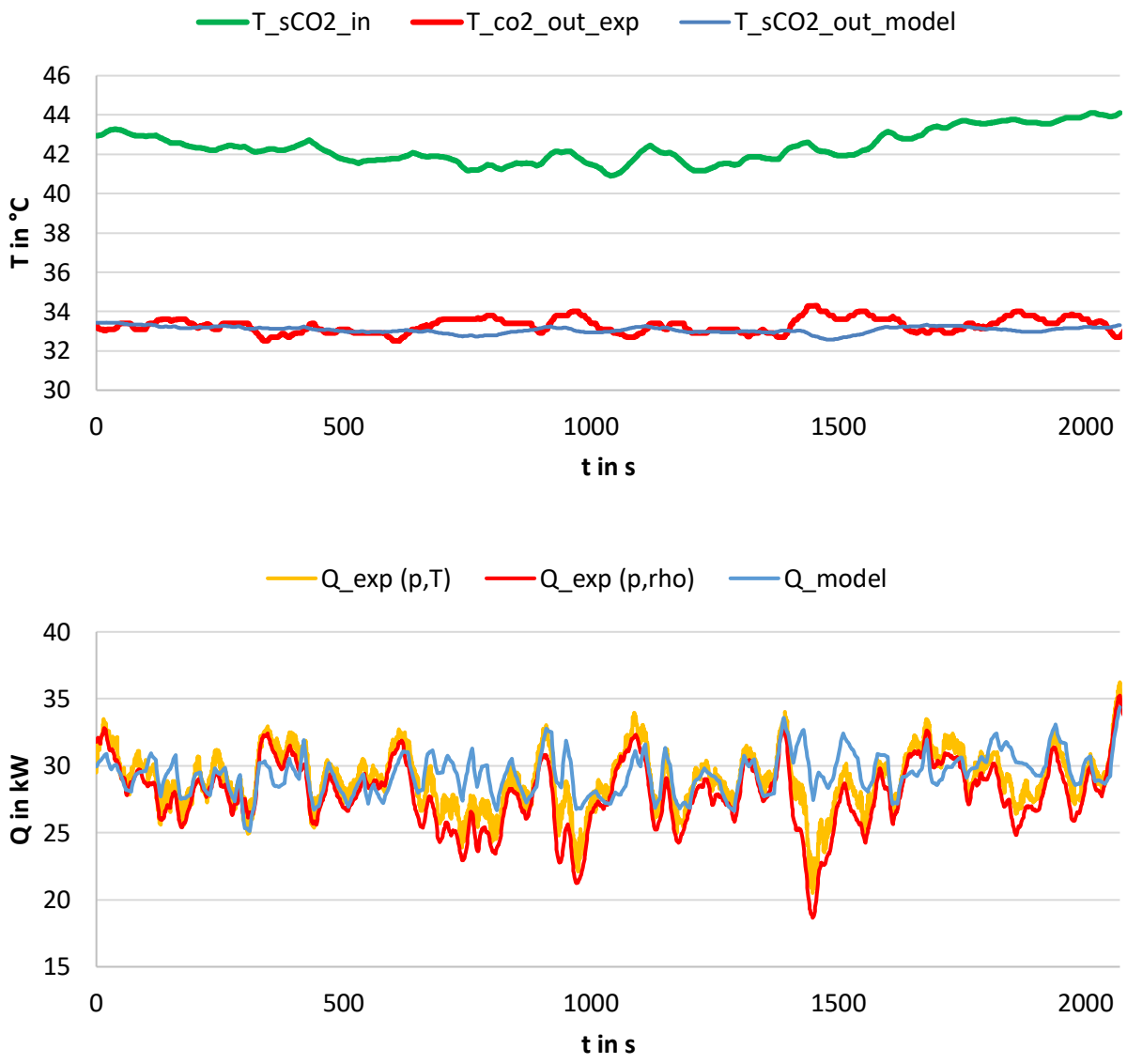

Figure 52 : Simulation of UHS in the time period before the benchmark starts, fan speed at 15 %

6.3.2 Slave electrical heater (SEH)

Due to the large thermal capacity of the SEH, the only real steady state of the SEH is the shutdown condition with two-phase CO_2. In theory, the simulation could start from shutdown, but the initial distribution of the CO_2 is unknown. The liquid CO_2 accumulates at the bottom and the gaseous CO_2 at the top. To circumvent this problem, the simulation is started with supercritical CO_2 during the heat up phase in such a way that the adequate temperature distribution will develop after a short time. This procedure is tested for several heat loads and can be seen in Figure 53 (data from 14.06.2019 from 14:39 to 14:54). Approximately 6 min before the simulation started, the set point of the heater was increased to 35 %, which equals a heating power of 84 kW. From the experimental data it can be calculated that at the start of the simulation a power of 19.3 kW is

transferred to the CO_2. As mentioned before this is no steady state. However, ATHLET requires to start from a steady state. Therefore, in order to match the transient curve, a slightly higher heating power must be specified at the start of the simulation, in this case 19.6 kW. From Figure 53 it can be observed, that the curves deviate only slightly from each other, but they show a slightly different slope during the heat up and cool down. This may indicate that a higher value for the thermal mass of the heater should be specified. However, from a material point of view this seems not realistic, because the mass of the modelled heater is already higher than the approximate mass of 2000 kg.

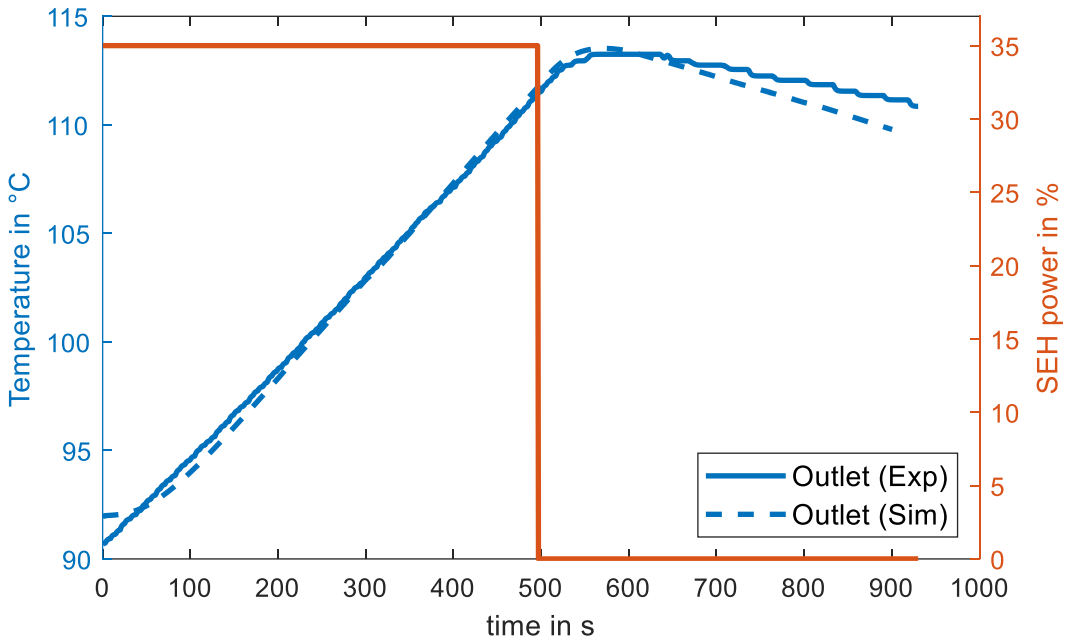

Figure 53: Experimental and simulated outlet temperature of SEH (left axis) and SEH power in % (right axis)

Both, the simulation and the experiment in Figure 53 show a delayed heat up, meaning that the maximum SEH outlet temperature occurs after the heater has already been shut down. This is also a transient effect, because during the heat up, a temperature gradient develops in the material, which causes the delayed heat up. To catch this effect, at least two material layers are required in the model. This first simulation is also used to evaluate the axial heat transfer. At the point where the maximum heat is transferred, the transferred power to the CO_2 is between 350 W and 900 W per subvolume and the encountered transferred power in axial direction inside the aluminium layer is between 1 W and 5 W per subvolume without the artificial increase of the thermal conductivity. The axial heat transfer in the steel is by two magnitudes lower. Including the artificial factor of 21 in the aluminium layer, as mentioned in the modelling section, yields an axial heat transferred of 15 W to 100 W. This is not negligible compared to the heat transferred to the CO_2 and, therefore, it is considered in all simulations.

The next experiment analysed lasted about 2 hrs (data from the 27.09.2019 from 9:47 until 11:57). In this case almost the whole experiment is simulated and not only a short period. Figure 54 shows the experimental SEH inlet and outlet temperature, together with the simulated outlet temperature and the corresponding mean material temperature and on the right axis the SEH power. The start of the simulation is carried out as described above, which explains the deviation between the experiment and the simulation in the beginning. During the heat up, the experimental and simulated curves agree quite well. However, the simulation does not reach the peak of the experimental SEH outlet temperature. After 2500 s, the cool down in the simulation occurs significantly faster than in the experiment. The value of the slope of the simulated outlet temperature

is in between the slope of the experimental curve and the mean wall temperature. The mean wall temperature is derived by calculating the average temperature of all layers and subvolumes for one time step. Comparing to the shape of this temperature curve, gives an indication how uniform the cool down process occurs. In the experiment the cool down of the SEH material is highly non-uniform. In order to reach a high outlet temperature, the temperature in the upper part of the material must remain on a high level. Therefore, the major part of the heat transfer must occur in the lower part of the SEH. This effect can also be seen in the simulation, but less pronounced. In the following, this effect will be explained by using the temperature profile along the length of the SEH.

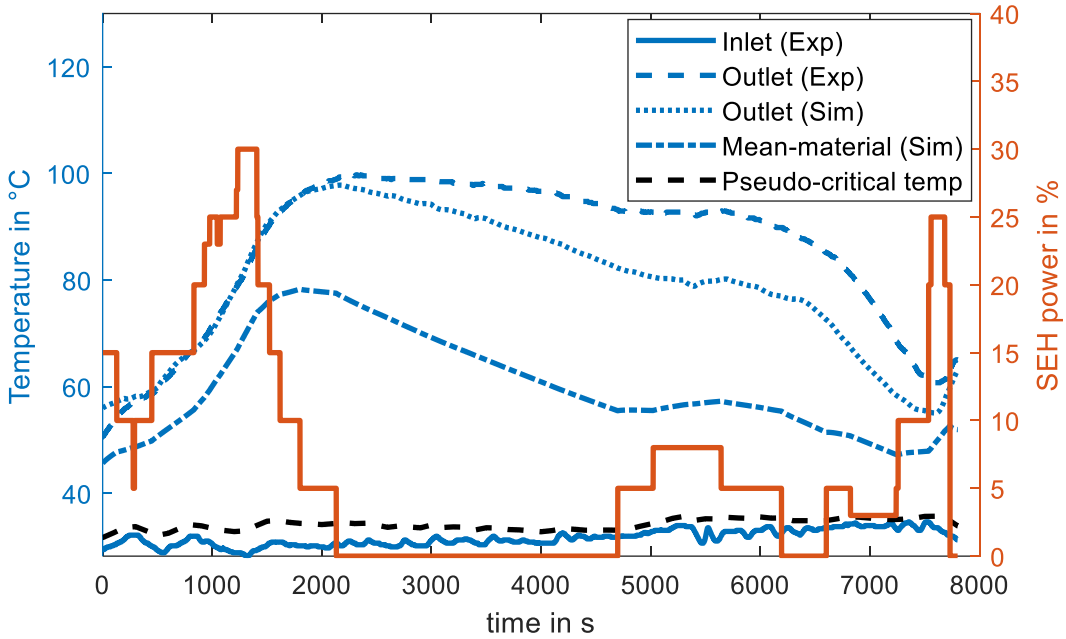

Figure 54: Pseudocritical temperature, experimental SEH inlet and outlet temperature, simulated outlet temperature profile and corresponding mean material temperature (left axis) and SEH power in % (right axis)

In Figure 55 two selected temperature profiles during the simulation are shown, namely during the heat up at the highest heat load at 1400 s on the left side and during the sharp cool down at 7000 s on the right side. During the heat up, a temperature profile in the material develops, which can be seen by comparing the different layer temperatures. During the cool down the temperature differences between the layers slowly vanish again. By comparing both temperature profiles, the mentioned non-uniform cool down of the material can be observed. The inlet temperature of the SEH is close to the pseudo-critical temperature, which can be seen in Figure 54. This leads to high heat transfer coefficients in the lower part of the SEH and causes a cool down starting from the bottom. This results in temperature profiles like shown in Figure 55 on the right. The effect can be described as a cold-front moving from bottom to top. In the beginning, the outlet temperature is only slightly affected because enough heat is stored in the material of the SEH. However, at the end, almost all heat is consumed and the temperature decreases rapidly. Even an increase of the SEH power might not stop a further decrease because it will need some time for the material to heat up again. Checking further experimental data confirmed this effect. As mentioned before, this effect occurs more powerful in the experiment. This suggests that the current general heat transfer correlation is not able to catch this to its full extent. Furthermore, a check of the Jackson criterion (Theologou, Mertz, Laurien, & Starflinger, 2019) indicates that buoyancy effects should be considered. However, it should also be mentioned that some deviations might be related to the modelling of the SEH or the measurement data correction.

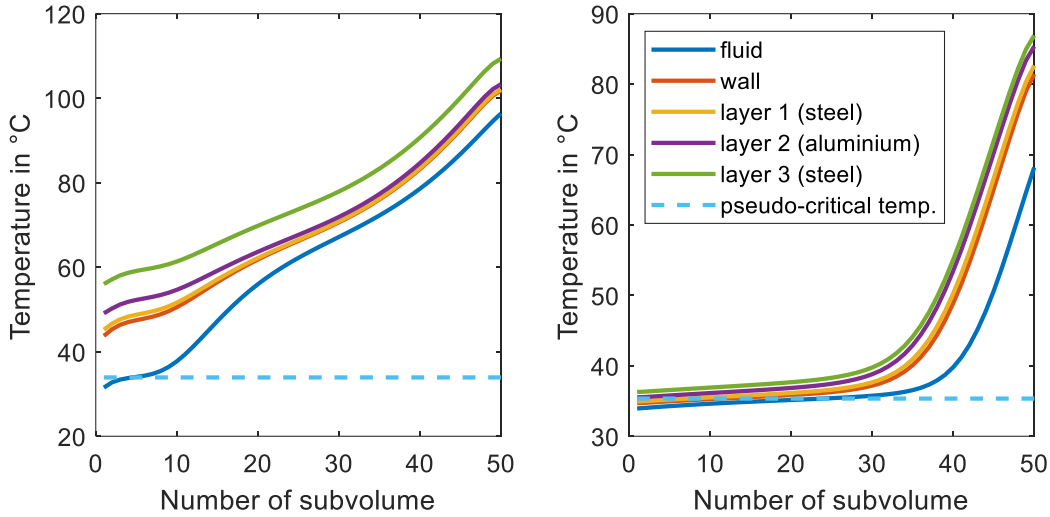

Figure 55: Simulated temperature profiles at a selected time: on the left during the heat up at the highest heat load (1400 s) and during the sharp cool down (7000 s)

6.3.3 Cycle calculations

In this chapter the steady state period (10.03.2020, 14:47:30 to 15:22) before the transient of the benchmark will be analysed. The experimental background for this period is provided in more detail in chapter 7.1. The procedure for the start-up of the simulation is explained in chapter 5.3.2. Since, the fill mass of the cycle is not known exactly and the cycle is also not in a real steady state condition, some parameters must be adjusted iteratively. However, this can be done mostly step by step.

First, the steady state of the cycle is analysed without modelling the heat transfer in SEH and UHS but rather providing the power input as a boundary condition. This simple simulation can be used to adjust the volumetric flow rate at the pump inlet and to check the assumed opening of valves which are in an intermediate position. It should also be checked if the volumetric flow rate of the pump which can be calculated from the pump speed corresponds to the mass flow rate measurement.

Second, the UHS and the SEH should be simulated individually using the experimental input values. Especially, the experimental outlet temperature of the SEH might not agree with the simulation. This indicates that the temperature profile in the SEH is not in steady state. In this case, a check of the control actions in the cycle confirmed that 120 s before the starting point of the analysed time frame the UHS power was increased from 12 % to 15 %. Therefore, the UHS fan speed, which approximately gives in a real steady state in terms of the SEH temperature profile should normally lie in between these two values.

Third, the mass of the cycle needs to be adapted, especially, checking the resulting cycle pressures and the density at the CHX inlet. The initial value for the adaption can either be taken from the experiment (filling and circulation procedure) or from the simple cycle and component simulations conducted in the first two steps.

In the end, this resulted in a fill mass of 70.7 kg, a volumetric flow rate at the pump inlet of 1.3 l and an UHS fan speed of 13 %, which corresponds to an air volume flow rate at the outlet of 0.5335 m^3/s for one UHS. For this simulation no valve opening was adapted, because the intermediate position of valve 24 was not changed during the simulation. Therefore, it is sufficient to increase the form loss coefficient of the related pipe, in this case by 285. This approximately agrees with the expected form loss coefficient from a valve opening of 13.3 % in the experiment (10 % valve opening corresponds to a form loss coefficient of 650 and 20 % opening to 220).

The mass of 70.7 kg includes 2.3 kg of mass in the accumulator. This value is lower than the value calculated in chapter 4.2.5, because adiabatic filling starting from 74 bar instead of 71 bar was accidently assumed. However, for the transient down to 74 bar this should be fine because only the mass that is released during the transient matters. Since, the real UHS fan speed is 15 % in the experiment, the fan speed is increased in accordance with the experiment 120 s before the starting point of the analysed period from 13 % to 15 %. In this way all boundary conditions are in accordance with the experiment at the beginning of the analysed time interval.

The transferred power in the UHS and SEH, as shown in Figure 56, is in good agreement with the experiment. The experimental power shows some fluctuations similar to the other parameters which are shown later. This effect is not caught by the simulation and may be related to resonances in the system, mentioned in chapter 4.2.3. Comparing the transferred power of the SEH to the electrical power input of 24 kW for the first 1195 s and to 28.8 kW for the remaining time (power was increased from 10 % to 12 %), gives the indication that in the first phase the SEH is slightly cooling down and afterwards the SEH is slightly heating up. This can also be confirmed when looking at the outlet temperature of the SEH, which is shown in Figure 57. In terms of the UHS, it was necessary to adapt the fan speed from 15 % to 14.25 % at 650 s to match the starting point of the blind benchmark. The power without adaption and some more explanations are given at the end of chapter 6.3.1. It can also be seen from chapter 5.3.3 that changes in the air flow considerably affect the air-side heat transfer coefficient of the UHS, which is the main limitation for the overall heat transfer.

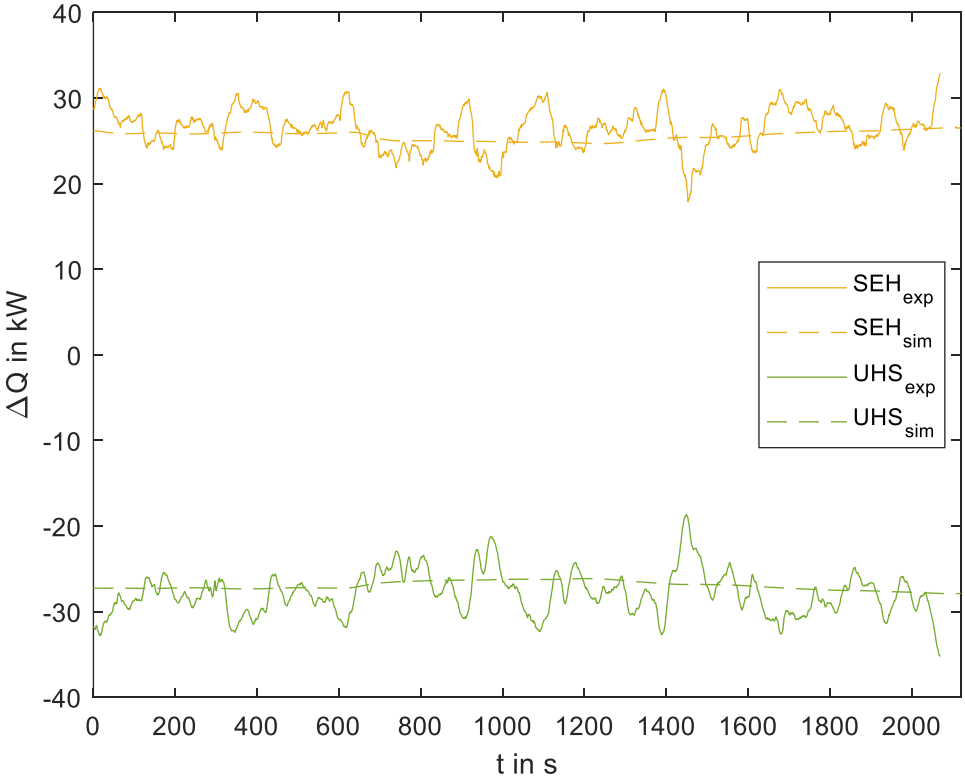

Figure 56 : Simulated and experimental transferred power of the UHS and SEH for the time before the benchmark

In Figure 57, the cycle pressures and temperatures for some measurement points (solid line) are shown together with the simulated value (dashed line). In the cycle, mainly three different pressure levels exist. The lowest pressure occurs at the PP inlet, the highest at the UHS and the pressure level of the SHE, which is almost the same as at the CHX is located in between. In Figure 57 on the left, one reliable sensor of each level is shown

together with the simulation. It can be observed, that in general the simulated pressure levels and trends agree well with the simulation. As mentioned before, the fluctuations in the simulations are considerably smaller. After 650 s the UHS inlet pressure is slightly underestimated. This might be related to the effect mentioned before while discussing the UHS power. In general, the level of the PP inlet pressure can also be matched. However in the middle of the simulation, the experimental pressure goes down approximately 1 bar further. Due to the high form loss coefficient of the partly open valve before this measurement point, only slight changes in the mass flow rate influence the pressure drop significantly. A more detailed discussion about this effect is included in chapter 7.3. In terms of temperature, five levels exist in this experiment, which are the inlet and outlet temperatures of UHS and SEH and the inlet temperature of the PP. Since, the last value is not measured, it is also not included in the diagram. All temperature levels except the UHS inlet temperature agree well with the experiment. The difference might be related to the measurement data correction or on combined effect of the valve and the pump before the UHS. It should also be mentioned that the SEH temperature level might be slightly higher which would affect the following transient due to the higher SEH material temperatures.

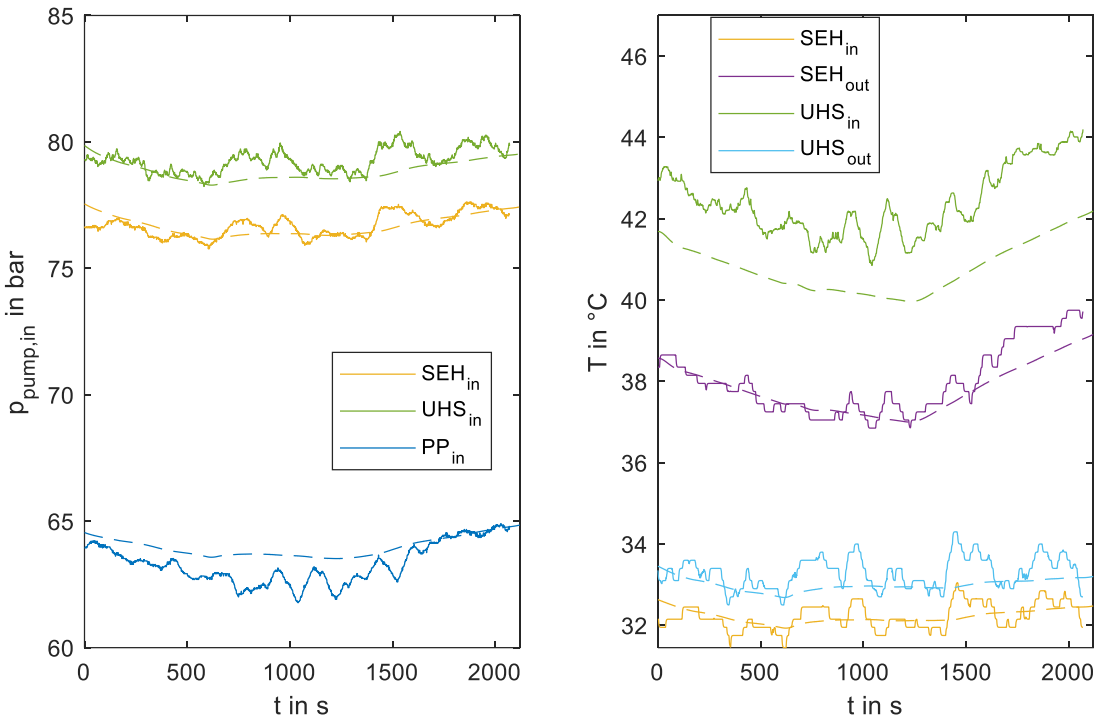

Figure 57 : Simulated and experimental pressures and temperatures for the time before the benchmark (experiment: solid line, simulation: dashed line)

In the density and mass flow measurements, shown together with the simulated values in Figure 58, the oscillations in the experimental values can be observed best. The density oscillates between a value of 470 kg/m³ and 620 kg/m³. The simulated density value only slightly changes but catches the mean trend of the experiment very well. The same behaviour holds for the mass flow rate. Altogether, it can be concluded that the simulation catches the behaviour of the experiment quite well except for the oscillations. The end point of this simulation is directly used to continue into the transient of the blind benchmark.

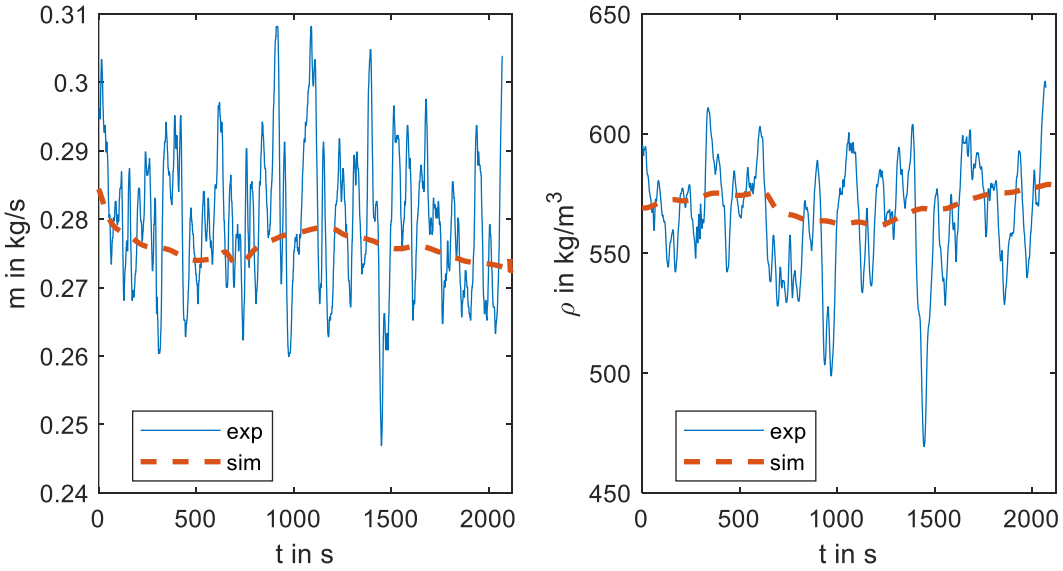

Figure 58 : Simulated and experimental mass flow rate and density for the time before the benchmark

7 Benchmark

7.1 Description

In order to get reproducible and therefore comparable results for all models, a steady state situation regarding input parameters, pressure and temperature, has been prepared at the sCO2-loop. It was the idea to use this state after some minutes to initiate a transient by perturbing the equilibrium of power input and heat removal changing the air flow for the UHS by fan speed.

7.1.1 Preparation of steady state

The reference run for benchmark test data was started in the afternoon of 10th of March 2020. The weather was rainy and windy in the beginning with cold and wet outside conditions, slowly warming up from 10 °C to 14 °C. The loop been circulated and filled up to a CO_2 mass of about 65 kg CO_2 the day before, but the periodically changing density during circulation did not allow a precise estimation of the exact fill mass from the density measurement. Thus, the mass would have to be obtained from the model calculations itself.

To keep external parameters as constant as possible, it was defined to run the PP with a reduced speed of 600 rpm (motor). This value was expected to provide a sufficiently high stable mass flow for pressure drop over components without stretching the motor power limit, pushing the pressure head to the technical limit of 80 bar while keeping the TAC pressure quite below the set-point of the relive valve (~67 bar a). For this, the pressure on suction side of the PP had to be adjusted by the valve TK02 S104 manually. This position had to be changed during heat up from 16.6 % down to 13.3 % because of changing density of the fluid. For the steady state the position was kept constantly at 13.3 % valve stem position.

To get a reliable mass flow information it was decided to shut TK02 S105 completely, hence allowing no bypass flow to the suction side of the PP, with the exception of negligible leakage through check valve TK01 S502 back into TAC.

The fans of the UHS have to be operated at a minimum speed of 10 % (~1/s) for frequency control reasons if running. To establish a steady heat transfer at UHS, it was decided to let the fans run with that speed from the beginning. To heat up the system smoothly, a SEH power of 10 % control input (24 kW of electrical power) was set, enough to bring up the pressure and temperature of the loop slowly towards the critical point. The ramp was initiated at about 13:10, and critical point was passed after about 1 hour.

At approximately 71 bar, a temperature change at inlet of pressure vessel 2 could be observed, indicating some fluid transfer to PV2.

The speed of heat up was continuously decreasing due to the increasing heat removal by the UHS. Reaching the intended pressure of 80 bar at UHS inlet at about 14:40, the speed of UHS fans was increased to 12 %, but had to be increased further to 15 % after some minutes (14:45), because the transient was not ended, and the TAC pressure was approaching the blowout point. At this point (14:43), TK02 S104 was adjusted to 13.3 % stepwise.

With fan speed on 15 %, finally the increase could be stopped, stabilising the UHS inlet pressure at 78 bar g, with only small, long term oscillations of less than 0.5 bar amplitude.

7.1.2 Maintaining steady state

From the review of data in the aftermath, the stability of TK01 P502 at 78.2 +/- 0.2 bar for several minutes after 14:47:30, directly after a ramp down from 80 bar with the new fan speed, was taken as a criterion for steady state. For next 20 minutes, the loop was running without changes of external parameters, except air temperature. Over this period, pressure went down slightly by half a bar, indicating some slight imbalance of power. To find an equilibrium point in a complex system (e.g. determining criticality in a cold nuclear reactor in terms of control rod position), it is sometimes more effective to maintain a slight imbalance in both directions and study the slow pace of change, keeping the system otherwise as stable as possible. Hence, at 15:07:27 the SEH power was increased to 12%, (28.8 kW electrical power). The intension was to increase pressure and temperature slightly to stabilize UHS heat transfer at a higher temperature difference, allowing to determine some effective characteristics for the heat transfer coefficient in terms of ΔT. Indeed, the pressure at UHS inlet stabilized to 78.6 bar +/- 0.5 bar within 5 minutes, and the stable run was continued for 10 more minutes, until 15:22. Again, only small, long-term pressure oscillations of 0.5 bar amplitude were observed at the UHS inlet.

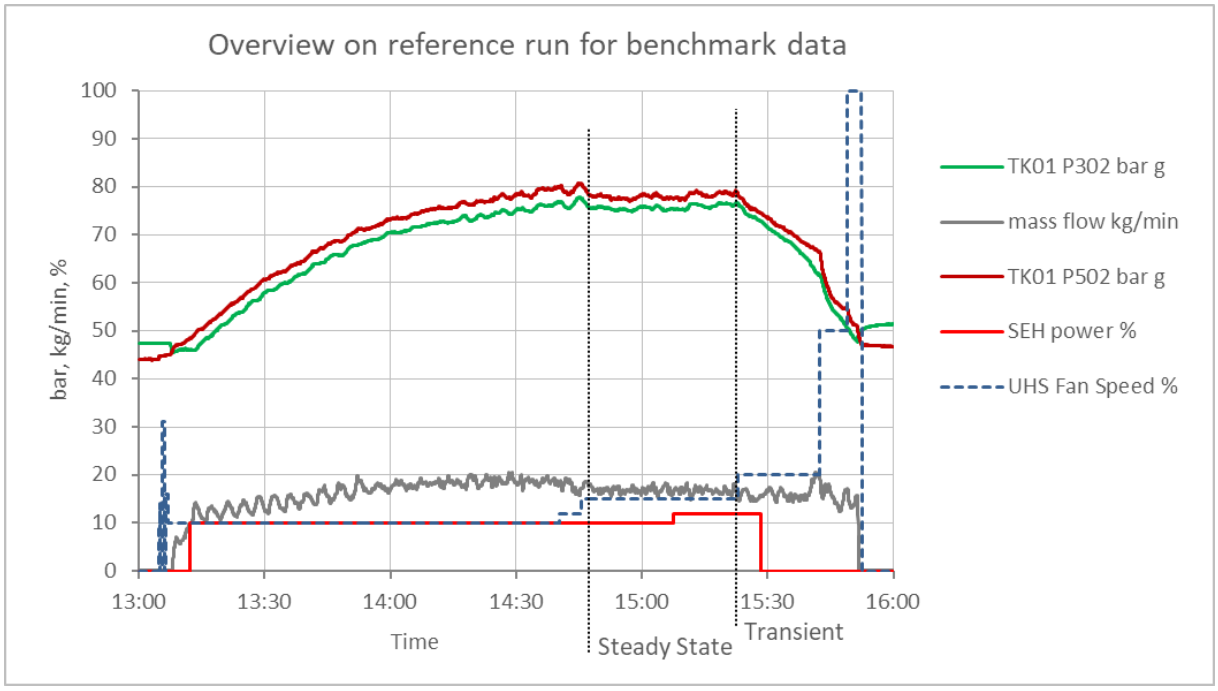

Figure 59 : Pressure and heat balance parameters

7.1.3 Performing the transient

From this stabilized state, at 15:22:53, the fan speed was increased to 20% of full speed.

Pressure measurements and temperatures indicated a fast decrease. Inside the UHS, the critical point of CO_2 was passed about 15:30, when pressure went below 72.8 bar g. Due to the pressure drop, the pressure at the SEH inlet had been subcritical some minutes before (at about 15:28), so that SEH-power was shut off at 15:28:27 to cool down the system and the SEH completely. Consequently, the effective duration for the benchmark transient is at least 5 min, concerning supercritical conditions needed to perform the calculations.

Table 6: Time schedule of actions

Time	Action	Value
13:04:38	Start PP	600 rpm
13:04:50 to 13:06:53	Start-up UHS fans (1 fan stuck, recovered)	10 %
13:08:05	TK02 S104 open (1 round)	16.5%
13:11:04	TK02 S105 closed	
13:12:06	SEH on, begin of heat up	10 %
13:54	PV2 takes fluid	71 bar
13:59	Critical pressure passed at UHS inlet	72.8 bar g
14:16	Critical pressure at SEH inlet	72.8 bar g
14:39	TK01 P502 above 80 bar	
	TK02 S104 reduced	15.2 %
14:40:16	UHS fan speed increased, first step	12 %
14:43:50	TK02 S104 finally reduced	13.3 %
14:45:30	Fan speed increased, final for stabilising	15 %
14:47:30	Begin steady state for open benchmark	
15:07:26	SEH power increased to increase pressure	12 %
15:22:53	End of file for steady state open benchmark	
15:22:54	UHS fan speed increased to initiate transient	20 %
15:22:54	Begin of Blind Benchmark	
15:28	SEH below critical pressure	
15:28:27	End of Blind Benchmark	
15:28:28	SEH shut down	0 %
15:31	UHS below critical pressure	
15:38:21-15:48:37	Gradually open TK02 S104	13 – 100 %
15:42:27	UHS fan speed 50%	50 %
15:49:06	UHS fan speed 100%	100 %
15:51:32	PP off	
15:51:58	TK02 S105 opens	100 %
15:52:36	UHS fans off	

7.2 Results for the starting point

The results for the starting point of the benchmark for the different models are compared to the experiment in Table 7. The boundary conditions of the models and the experiment are given in Table 8. When comparing the experiments to the model, it should be kept in mind that the experiment shows some oscillations as mentioned before. Since, different approaches were chosen in arriving at this starting point and due to the different development and testing status of the models, the results and specifications may differ from the experiments. Graphically, the starting points at the different measurement positions can also be seen in the figures of the next chapter, which shows the transient of the blind benchmark.

How the values for the starting point of the benchmark are determined in **ATHLET**, is explained in chapter 6.3.3 and will only be shortly recapitulated here. Since, the starting point is no real steady state, it is selected to approach the start point by simulating the time period before the start of the benchmark. This especially affects the temperature profile in the SEH because it is a function of the simulation history. Furthermore, not all pressures and temperature are in exact agreement with the experiment because except for a minor adjustment of the UHS fan speed and the fitting of the air-side heat transfer coefficient no parameters were fitted to the experiment in order to avoid overfitting. Since, the relation of the air-side heat transfer coefficient also gives good results for other experiments, as shown in chapter 6.3.1, only the minor adjustment of the fan speed from 15 % to 14.25 % needs to be discussed. As also mentioned in chapter 6.3.1, this might be due to wind or humidity effects or a slight inaccuracy of the prediction of the heat transfer coefficient or the air volume flow rate. The highest difference between the model and the experiment occurs at the inlet of the pressure vessel II. The inlet pressure of the model is too low compared to the experiment. Since this component was added very recently to the model, accidentally the location where the form loss coefficient of pipe 1 is applied was not adapted. This can easily be corrected in the future. For the transient behaviour, this error should be of minor importance, because mainly the pressure difference compared to the start of the simulation matters for the mass injection into the cycle. Altogether, the model agrees quite well with the experiment.

In case of the **MODELICA model**, starting point was understood like stationary state defined by arithmetic average of individual parameters (pressures, temperatures…) over the time spanning from 15:17:00 to 15:22:53, that is the last 6 minutes before the transient benchmark starts (10th of March 2020, Essen time). In this way initial imbalances that are present in the system before the transient benchmark starts are not modelled.

In case of the MODELICA model the starting point was reached by the following procedure:

- Before the transient benchmark starts the model is handled as an open loop.
- Model is tuned so that average starting point values of pressures, temperatures, SEH electrical power input and mass flow obtained from measurement are reached as closed as possible. For this purpose, the SEH outlet temperature artificial control loop is incorporated.
- Because of operating the loop in a close vicinity to critical point, small change of temperature in front of the SEH leads to high change in the SEH electrical power input, making it difficult to tune the loop model.
- The model convergence is also sensitive to discretization. So for example only 20 elements in axial direction were at the end used to discretize the SEH (46.5 m long).
- After the stationary state is reached (please see Table 7 and graphs in section 7.3), the model is switched to a close loop layout and the benchmark may start.

Visualization of some parameters in the CO_2 heat diagram is depicted in Figure 60. Main experiment framework is following: maximum temperature and pressure difference is approximately 16 °C and 15 bar. Mass flow rate and heat flow are approximately 0.26 kg/s and 30 kW.

When comparing the MODELICA and measured starting point following remarks might be considered:

- The UHS heat transfer to CO_2 at the transient beginning is in the model higher compared to that received from measurement (+22 %). The main attention during the stationary state model tuning was payed to the SEH electric power input, which was about 28.8 kW. So the SEH inlet temperature (and thus UHS outlet temperature) in the model was tuned in order to come sufficiently close to the measured value of 28.8 kW. Probably the main influencing factor in power discrepancy between model and measurement at the benchmark beginning is the sensitivity of the SEH CO_2 heat input on the SEH CO_2 inlet temperature. One more influence arise from the fact that SEH is not in stationary conditions at the benchmark starting point. Difference in CO_2 enthalpies (inlet, outlet) for the measurement is 94.8 kJ/kg while for MODELICA model it is 106.1 kJ/kg (+10.5 %). Also the measured mass flow rate 0.256 kg/s is lower compared to that in model 0.276 kg/s (+6.2 %). In terms of power transferred to CO_2 this yields approximately 24 kW for the experiment and 29 kW for the model suggesting that part of the electric power (28.28 kW as measured) is transferred to the SEH walls instead of to CO_2 concerning experiment starting point. If this would be the case for the MODELICA model also then the SEH model inlet temperature might be higher compared to that suggested for the model now.
- Higher than measured UHS heat transfer at starting point is in the model characterized by a high heat transfer coefficient that is at the moment considered as a constant value of 20 W/m^2K.
- Shortcomings in the pressure losses modelling were identified (the total pressure drops are underestimated in the model). More attention shall be payed to the valves models in the future.

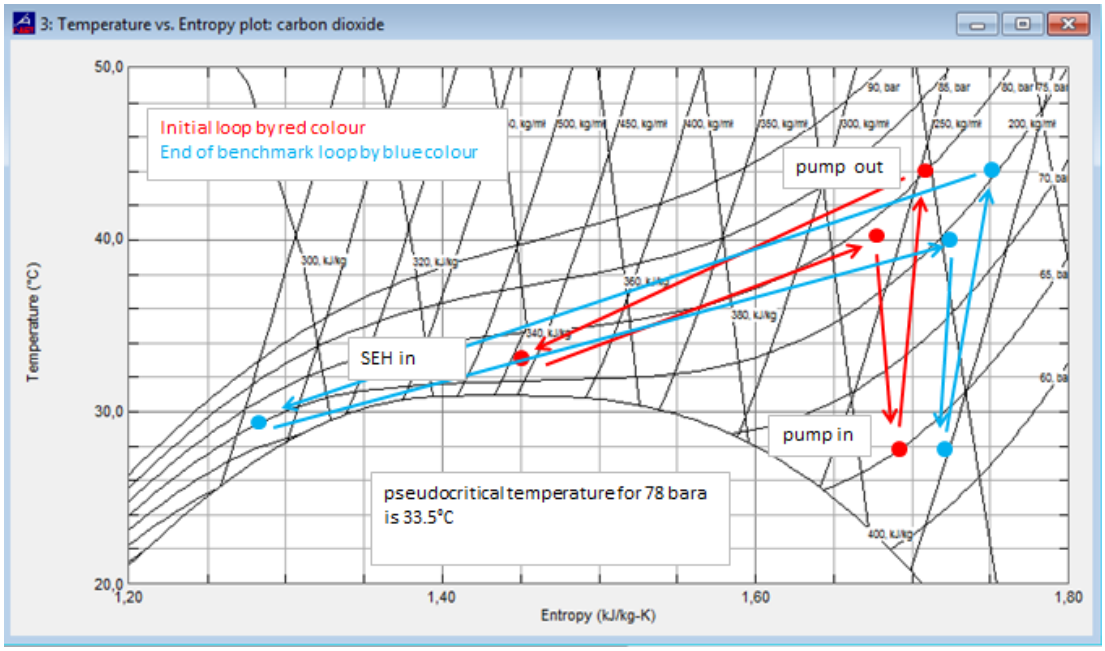

Figure 60: Measured points in T-s diagram

Table 7: Starting point conditions for transient benchmark – Measurements

Name	No. in PID	Variable	Unit	Measure-ments	MODELICA	ATHLET	CATHARE
UHS - Inlet pressure	TK01 P502	p	bara	79.6	79.8	79.4	74.6
UHS - Inlet temperature	TK01 T502	T	°C	44.6	42.9	42.1	41.2
UHS - Outlet pressure	TK01 P101	p	bara	79.7	79.1	79.1	74.6
UHS - Outlet temperature	TK01 T101	T	°C	34.0	32.3	33.2	31.5
UHS - Transferred heat		Q	kW	25.1	31.7	27.6	
PP - Inlet pressure	TK02 P101	p	bara	65.2	64.9	64.7	
PP - Inlet temperature		T	°C		27.8	29.2	
CHX - Inlet pressure	TK01 P202	p	bara	77.8	78.2	77.4	74.0
CHX - Inlet temperature	TK01 T202	T	°C	32.9	32.0	32.5	31.1
CHX - Inlet density	TK02 M201	ρ	kg/m³	533.9	627.8	577.4	
CHX - Inlet mass flow	TK01 F201	$\dot{m}$	kg/s	0.26	0.28	0.27	0.31
CHX - Outlet pressure	TK01 P301	p	bara	77.6	78.1	77.3	73.9
CHX - Outlet temperature	TK01 T301	T	°C	33.0	32.0	32.4	31.1
SEH - Inlet pressure	TK01 P302	p	bara	77.5	78.2	77.4	73.3
SEH - Inlet temperature	TK01 T302	T	°C	32.8	32.0	32.5	30.7
SEH - Outlet pressure	TK01 P401	p	bara	77.4	78.1	77.3	73.2
SEH - Outlet temperature	TK01 T401	T	°C	40.4	39.5	39.1	36.6
SEH - Transferred heat		Q	kW	24.0	29.3	26.2	18.6
PV I - Inlet Pressure	TK06 P101	p	bara	78.6	no model	no model	
PV II - Inlet Pressure	TK06 P201	p	bara	79.4	no model	77.9	
Air - UHS inlet temp.	TK04 T201	T	°C	13 - 13.6	13.3	13.6	
Air - UHS outlet temp.		T	°C		40.0	34.1	

Table 8: Starting point conditions for transient benchmark – Specifications

Name	No. in PID	Variable	Unit	Measure-ments	MODELICA	ATHLET	CATHARE
UHS - Rated fan Speed (Unit 1)	TK01 B501		%	15	15.8	14.25	
UHS - Rated fan Speed (Unit 2)	TK01 B501		%	15	15.8	14.25	
SEH - Rated electrical power	TK01 B301		%	12	12.2	12	
PP - Rated speed	TK02 D102		%	83.3	63	65	
Valve 2 - Position	TK01S102		%	100	100	via ξ	
Valve 4 - Position	TK01 S202		%	100	100	via ξ	
Valve 10 - Position	TK02 S101		%	4	no model	via ξ	
Valve 11 - Position	TK06 S101		%	101	no model	via ξ	
Valve 15 - Position	TK06 S201		%	100	no model	100	
Valve 24 - Position	TK02 S104		%	13	22	17 (via ξ)	
Valve 27 - Position	TK02 S105		%	0	no model	0	
CO_2 filling			kg	~ 65	~ 67	70.7	

7.3 Transient results

In this chapter the transient benchmark results of the models are compared with the experiment. When evaluating the differences, it should be kept in mind that some conditions during the benchmark are very close to the critical point of CO_2 and others not. Therefore, also a comparison of the transferred power in UHS and SEH is shown. Furthermore, some uncertainties remain due to the measurement data correction and the accuracy of the measurement. Additionally, it should be stated that it is quite challenging to perform simulations so close to the critical point due to the high gradients in the thermodynamic properties and special effects in terms of pressure drop and heat transfer. In the following the different measurement positions and components are examined always comparing the measurements with the models in one diagram.

The pressures, temperatures and the power of the UHS are shown in Figure 61 to Figure 64. For the correction of the air inlet temperature only a temperature range has been determined so far. Therefore, the upper and lower bound of the corrected air temperature are shown in the diagram. For ATHLET the upper bound was selected because with lower air temperatures the performance of the UHS would be overestimated in the simulation. The pressures and the transferred power agree well with the experiment except for the trend of the transferred power in the end of the simulation. Such a different trend at the end of the simulation can also be observed in some other parameters below. The reason might be related to the fact that the cycle is quite close to the critical point, where special physical effects may occur or numerical instabilities, as will be discussed later. In terms of temperature, the inlet of the UHS considerably deviates from the measurement. At the beginning, it rather looks like the constant offset which can already be observed from Figure 57 and results from the starting point. However, after approximately 3 min the difference starts to increase. It is believed that this results from the behaviour of the SEH. This is discussed further together with the SEH measurements below.

Concerning the **MODELICA** model for the transient benchmark, following initial and boundary conditions were used:

- Initial conditions defined by the average starting point state
- During the transient development
    - The SEH electrical power input is kept constant at 29.28 kW (+1.7 % with respect to the measurement)
    - The PP speed is kept constant at 63 % (-24 % with respect to the measurement)
    - The fan speed was increased from 15.8 % to 21% during the 1st second of the transient experiment (measurement: from 15 % to 20 %)

Air inlet temperature to the UHS is kept constant at 13.3 °C (this is not the case in reality).

Some remarks about the MODELICA simulation results follow. The difference between UHS average pressure obtained from model and UHS average pressure obtained from measurement depends on how close to reality the pressure losses are modelled mainly with respect to reduction valve number 24. In terms of equations this might be described as follows.

The pressure equation for the loop model (elevation differences and momentum changes during the transient neglected):

$$P_{PP_{in}}^{model} + \Delta P_{24}^{model} = P_{UHS}^{model} - \Delta P_{loop}^{model} \tag{26}$$

Here the first parameter is PP inlet pressure, second is reduction valve pressure drop, third is average UHS pressure and forth is loop pressure drop.

Similar equation might be written for experiment pressures as follows:

$$P_{PP_{in}}^{experiment} + \Delta P_{24}^{experiment} = P_{UHS}^{experiment} - \Delta P_{loop}^{experiment} \tag{27}$$

When combined together and when considering that PP inlet pressure in MODELICA model corresponds to that obtained from measurement during the transient, this yields:

$$P_{UHS}^{model} - P_{UHS}^{experiment} = (\Delta P_{24}^{model} - \Delta P_{24}^{experiment}) + (\Delta P_{loop}^{model} - \Delta P_{loop}^{experiment}) \tag{28}$$

These equations nevertheless do not satisfy the mass conservation in the loop as this would require that temperatures are also taken into account.

In this way it seems that the reason for the pressure discrepancy between the model and measurement is related to shortcomings in pressure loss modelling. But more thorough analysis would be needed.

Temperature at UHS inlet is influenced by the temperature at SEH outlet, the throttling process in the reduction valve 24 and by PP power input. As SEH outlet temperature is almost constant, pressure drop over valve 24 changes within 10 % over the time in the model and PP power input is relatively small and changes over 10 % in the model. Also the UHS inlet temperature changes only slightly.

Temperature development at the UHS outlet is not monotonic in the experiment, but it slows down and then stays 2 minutes (15:25÷15:27) constant and then continues to decrease. In the MODELICA model this is not observed. One of the reasons might be the fact that in MODELICA, the CO_2 mass flow rate does not experience such an increase compared to experiment at that time.

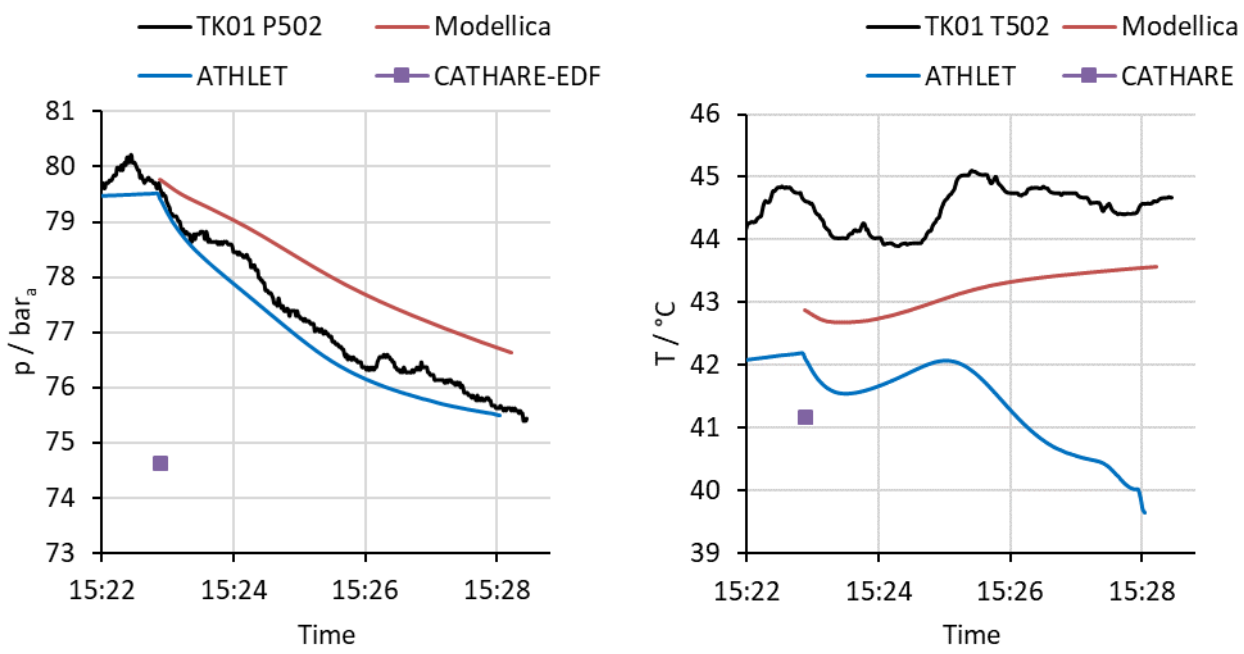

Figure 61: UHS – CO_2 inlet (p, T)

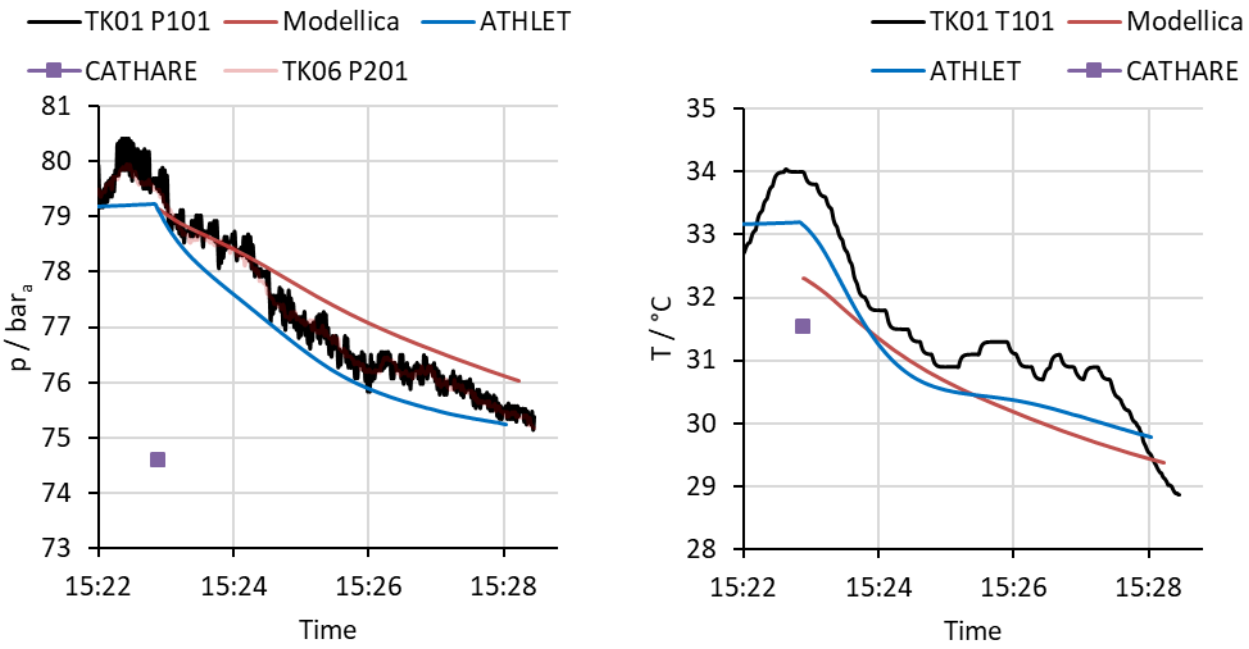

Figure 62: UHS – CO_2 outlet (p, T)

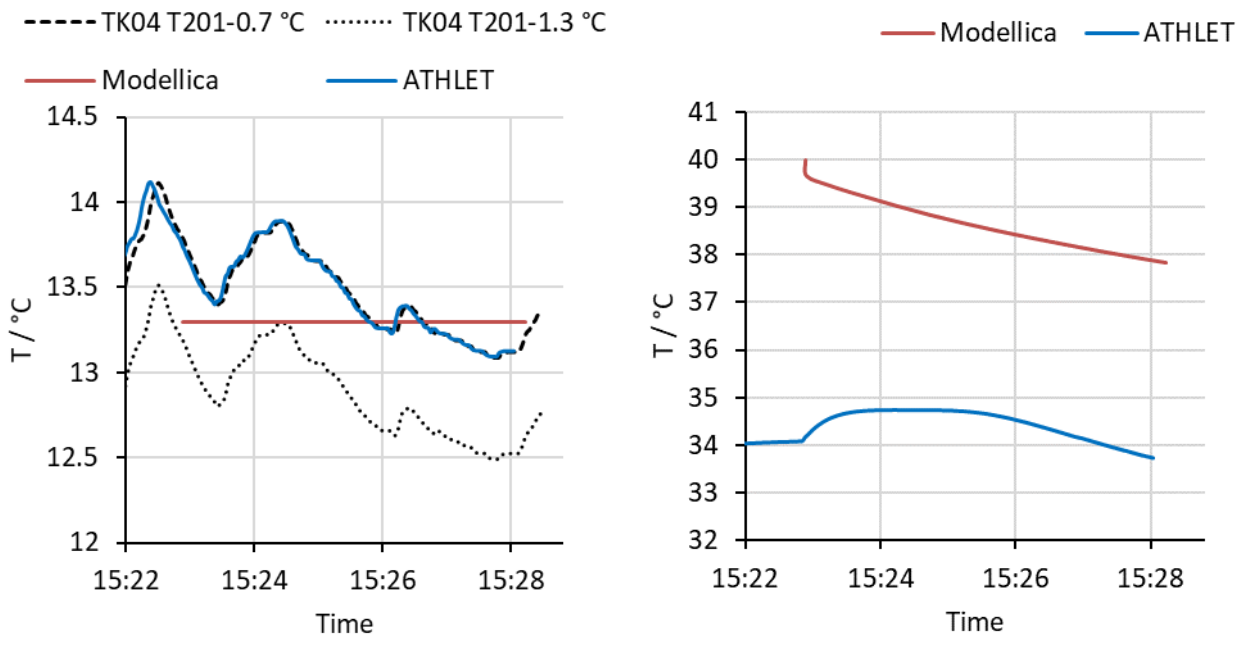

Figure 63: UHS – Air side (T_{in}, T_{out})

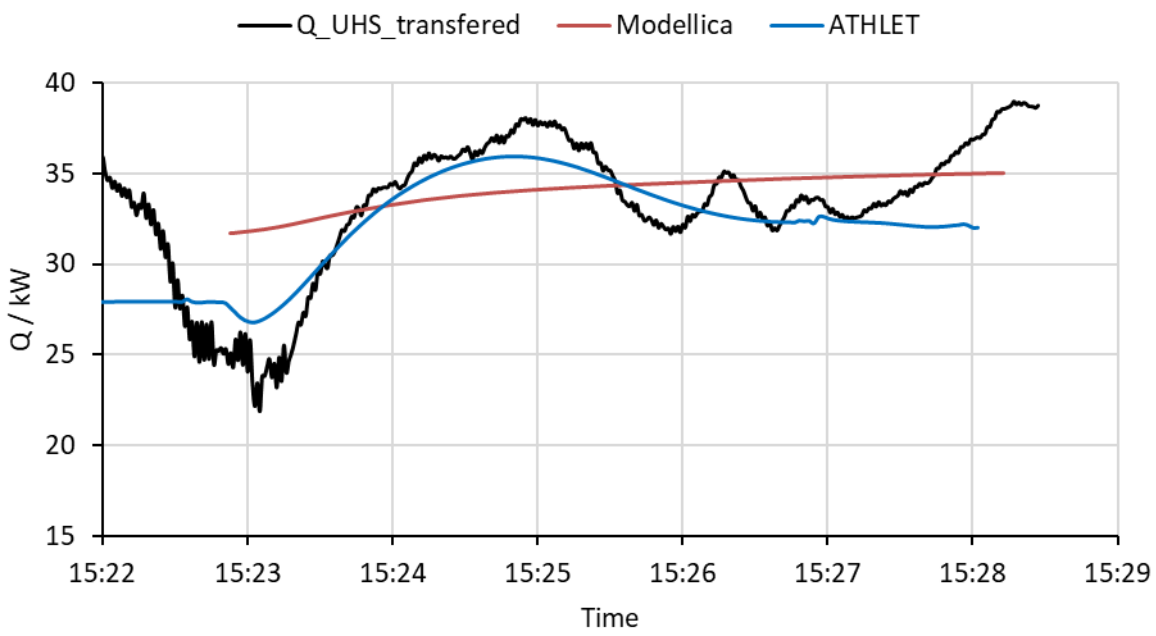

Figure 64: UHS – Transferred heat (Q)

In Figure 65 to Figure 67, the measurements and the simulation results of the CHX are shown including the mass flow rate and the density at the CHX inlet. Since, the glass model is not under operation no heat transfer occurs over the CHX in this experiment. Therefore, the temperatures are mainly a result of the UHS outlet temperature only a slight drop can be observed caused by the pressure losses is the long line between CHX and UHS. For ATHLET all parameters agree well with the experiments except for a different trend at the end of the simulation, as already discussed before. For MODELICA density at CHX inlet is higher by 19 % compared to measurement. This is caused by the lower temperature at UHS outlet compared to measurement. The reason for this behavior was described earlier.

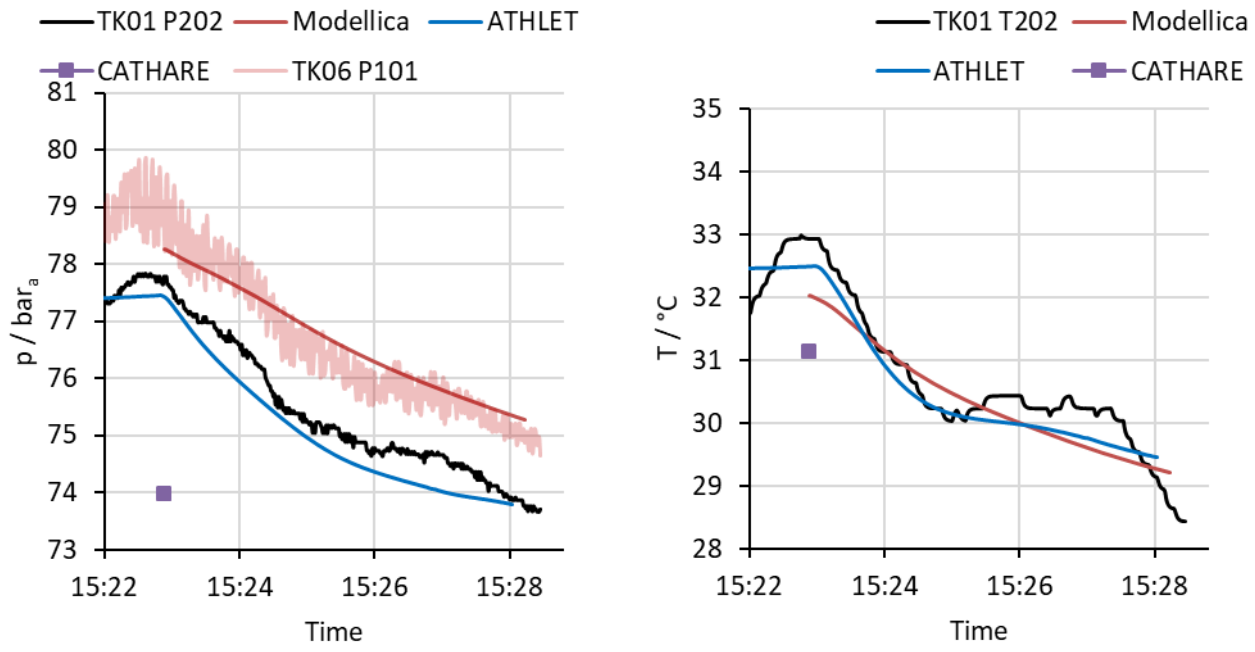

Figure 65: CHX – Inlet (p, T)

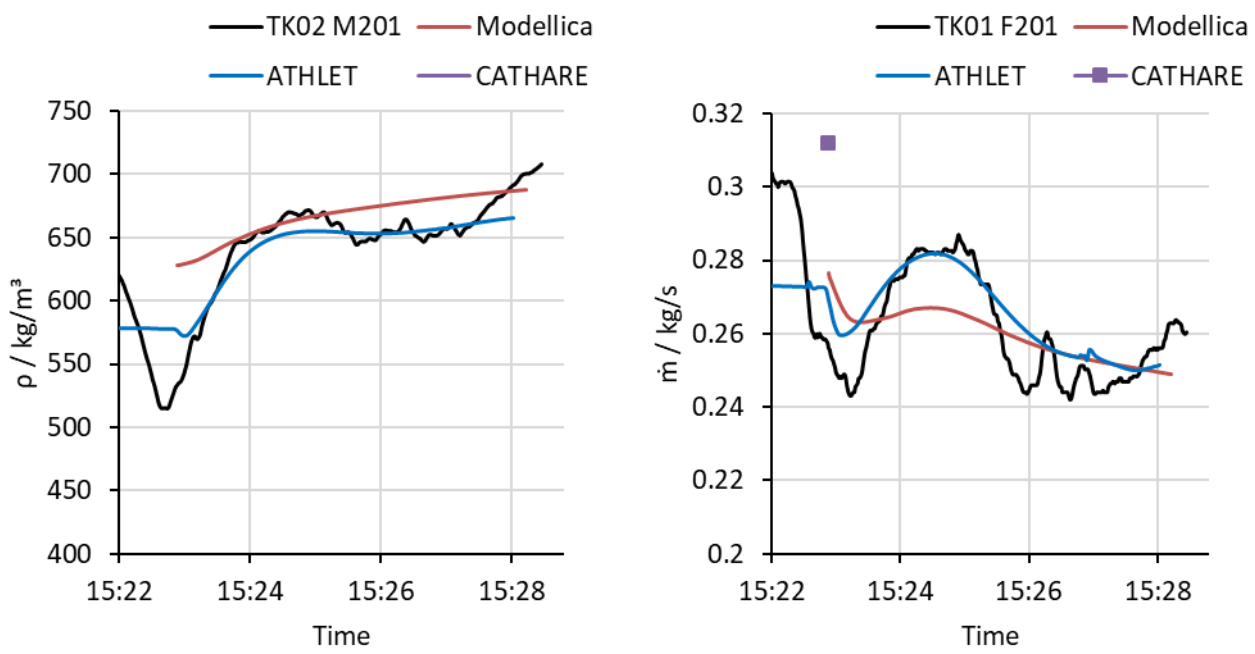

Figure 66: CHX – Inlet (ρ, ṁ)

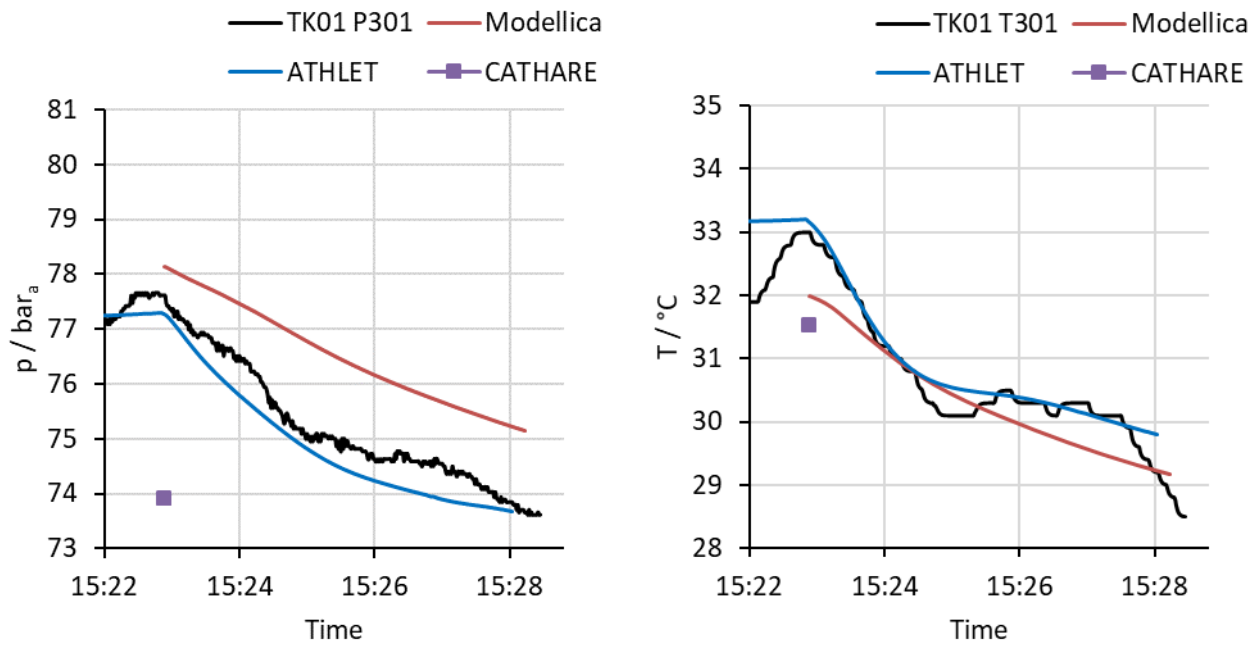

Figure 67: CHX – Outlet (p, T)

In Figure 68 to Figure 70, the measurements and the simulation results of the SEH are shown including the transferred power. It should be mentioned that the actual transferred power is higher than the electrical power input to the SEH by up to 7 kW. This results from the heat which is stored in the material of the SEH.

The ATHLET results agree well with the experiments except for the SEH outlet temperature but including the SEH power which is interesting at first glance. At 15:25, when the difference between the temperature measurement and the simulation starts to get higher, the pressure in the experiment and the simulation has already decreased to 75 bar and 74.5 bar, respectively. Since, the temperature at the SEH inlet is slightly below

the pseudo-critical temperature the pseudo-critical point is crossed inside the SEH. This means that most of the heat is transferred at an almost constant temperature and the heating of the fluid occurs just right before the outlet of the SEH. The CO_2 temperature profile looks qualitatively similar to the temperature profile shown in Figure 55. The material temperature profile is different because the SEH power is still at 10 %. However, this discussion is mainly focused on the fluid. From 15:25 to 15:28, the enthalpy difference between SEH inlet and outlet slowly increases from 124 kJ/kg to 131 kJ/kg in the experiment and stays nearly constant at 123 kJ/kg in the simulation. The inlet enthalpy is nearly the same with approximately 293 kJ/kg. The outlet temperature of the SEH is already considerably higher than the pseudocritical temperature. Therefore, the temperature is increasing steeply with an increase in enthalpy. A difference of 8 kJ/kg results in a temperature difference of more than 2 K. Decreasing the pressure by 1 bar at this point would also decrease the temperature by approximately 1 K. Altogether, this can explain the difference in the outlet temperature. The reason for the increasing difference may be related to heat transfer effects close to the critical point, as already discussed in chapter 6.3.2. Another explanation is that this effect is due to the slight over prediction of the mass flow rate, shown in Figure 66, or the fluid storing capacity of the SEH. A slightly lower mass flow rate at the exit of the SEH would result in a higher outlet temperature. This slightly lower mass flow rate would also be in accordance with the PP results presented below. However, in the future the overall behaviour of the SEH should be examined in more detail.

Concerning SEH and MODELICA results the general trend in CO_2 temperature development follows the experiment, but the wavy character is not captured as it was the case for the UHS outlet temperature. The main observation is that while the SEH inlet temperature in the experiment and model differs over time by 3.9 °C and 2.7 °C, (Figure 68), at the outlet of SEH temperature changes only slightly over time (Figure 69). This could be possibly explained by the increase in heat flow to the CO_2 during the transient (Figure 48) influenced by increased heat transfer coefficient at CO_2 side (Figure 47) and by the presence of thermal energy reservoir in the form of the SEH hot metal.

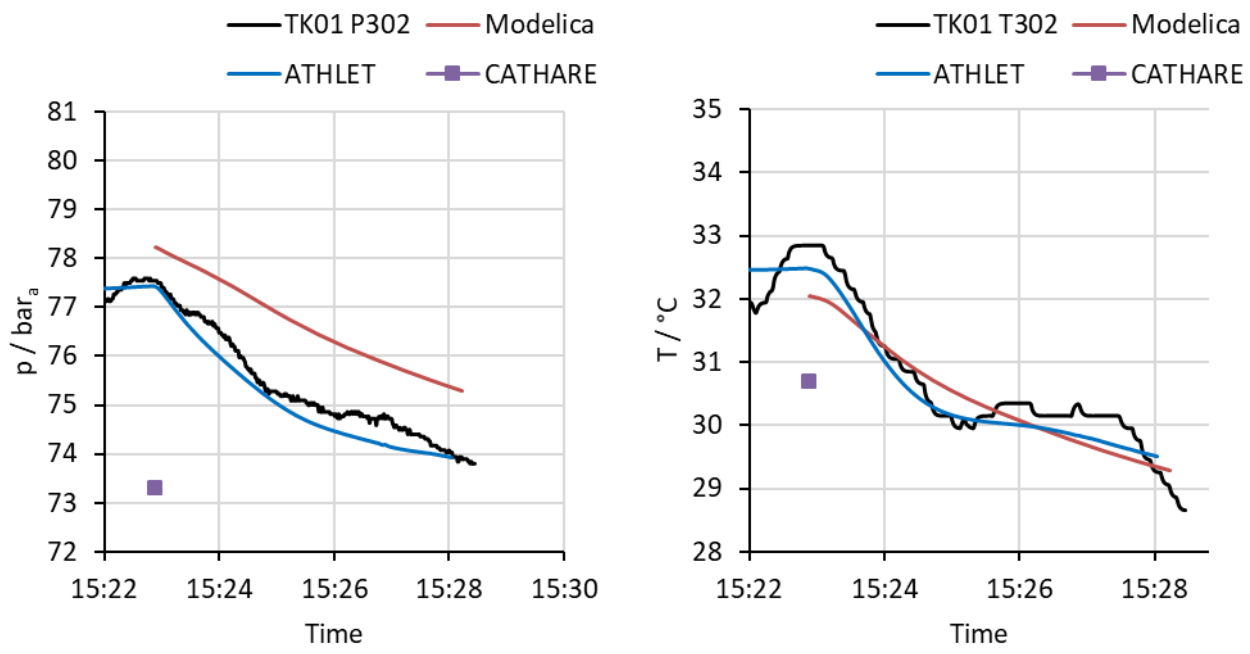

Figure 68: SEH – Inlet (p, T)

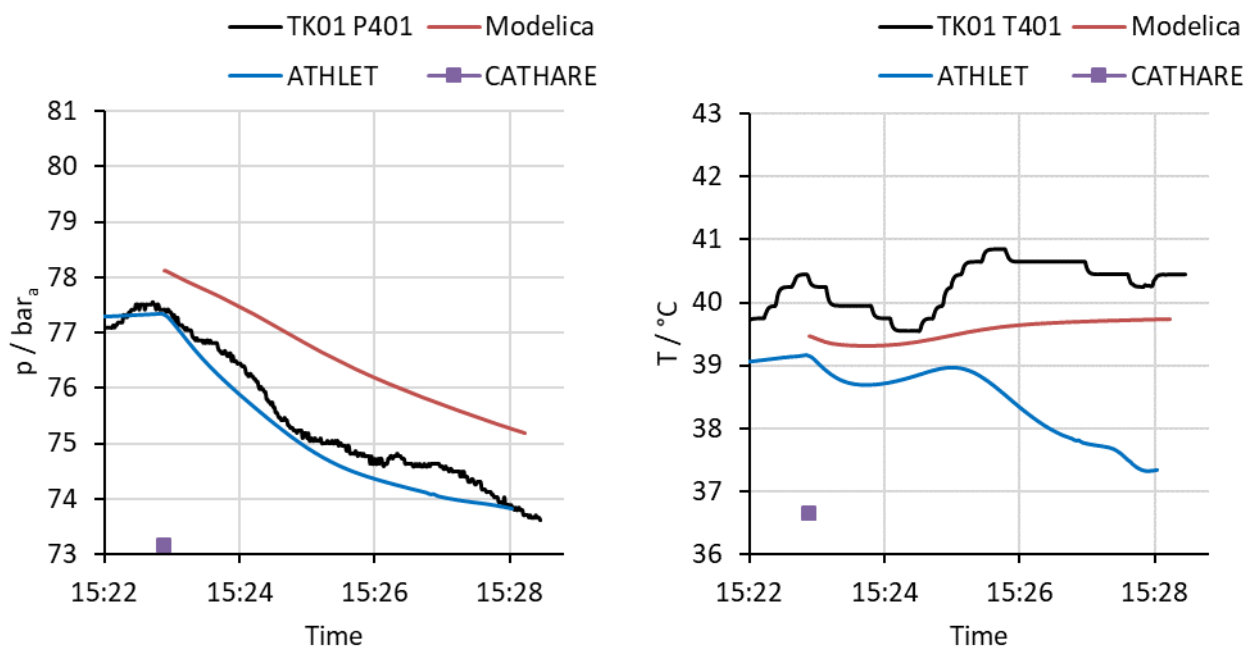

Figure 69: SEH – Outlet (p, T)

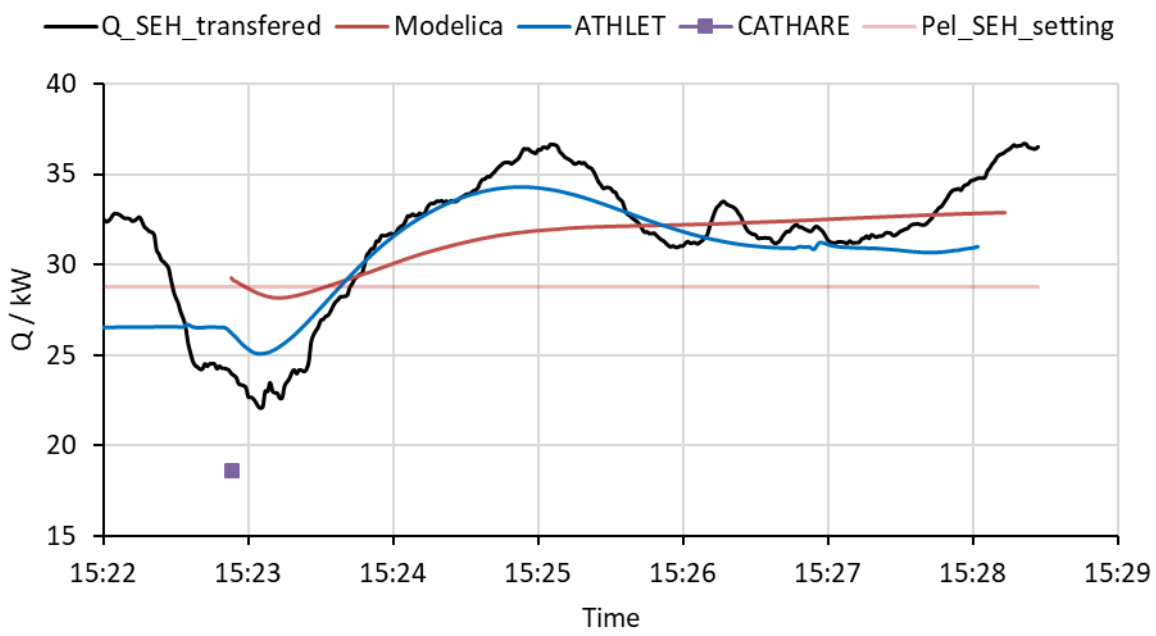

Figure 70: SEH – Transferred heat (Q)

In Figure 71, the inlet pressure and temperature for the PP are shown. Inlet temperature was not measured, therefore, only the models are shown in the right diagram.

For ATHLET, the profile of the PP inlet temperature is again directly related to the SEH outlet and therefore not further discussed here. Compared to the experiment, ATHLET shows a lower inlet pressure. Since, the valve before the PP is strongly throttled, the form loss coefficient is quite high. This means that only a slight change in the mass flow rate will influence the pressure drop and therefore the inlet pressure of the PP decisively. For the difference of about 1 bar, only a change of 0.01 kg/s is needed. This means that the slight

differences, shown in Figure 66, can easily explain the lower pressure. Moreover, it might be possible that during the transient the SEH partly functions like a mass storage due to the high density gradients close to the pseudo-critical point.

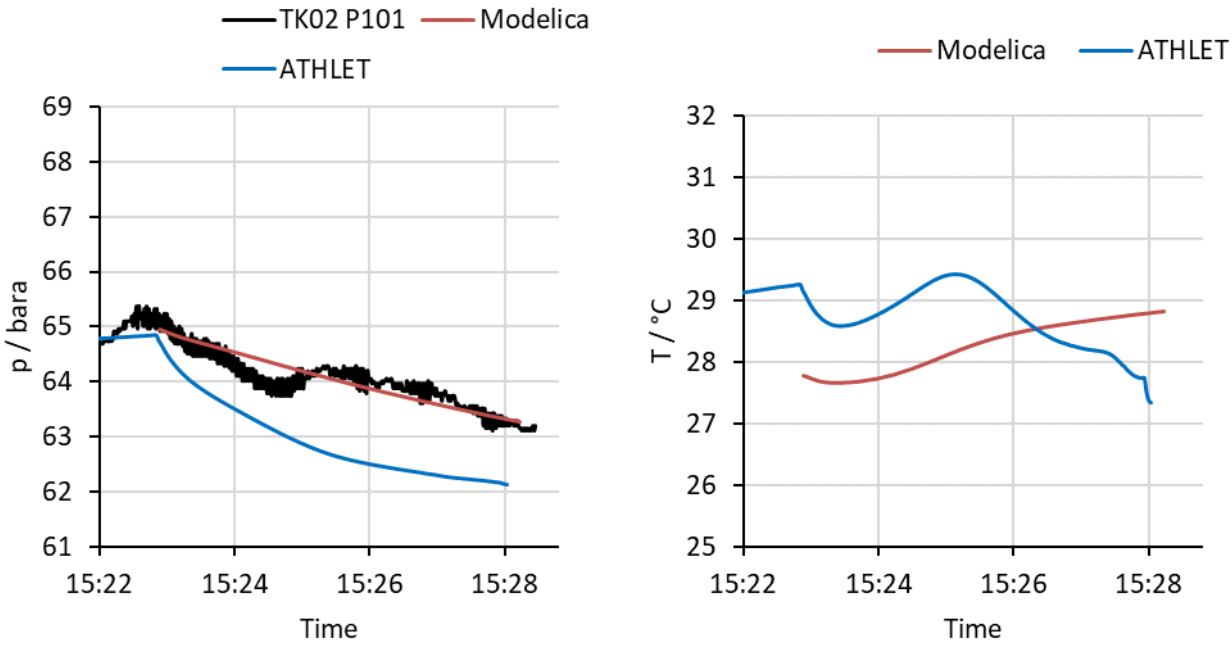

Figure 71: PP – Inlet (p, T)

In conclusion, ATHLET captures the experimental behaviour of the loop quite well except for the oscillations occurring in the experiment and maybe some minor effects concerning the SEH. However, due to numerical instabilities close to the critical point, it was not possible to continue the simulation. Therefore, the recent implementation of the thermodynamic properties for subcritical pressures and the transition to supercritical pressures needs to be improved and tested further. Fortunately, the main operation points of the sCO2-HeRo loop at NPP scale will be located considerably above the critical pressure. Thus, this problem will only important concerning some off-design operational states.

In conclusion, MODELICA follows the general trends compared to measurement, but the wavy character of the transient is captured only moderately.

8 Conclusion

The objective of the work presented in this report is to provide the validation status of the sCO2-HeRo loop for each code used in the sCO2-4-NPP project (CATHARE, ATHLET, and MODELICA).

Reference data for the benchmark could be provided from the sCO_2-loop at the Simulator centre in Essen. From thorough analysis temperature related deviations in pressure measurements could be corrected widely, as well as deviations in the temperature measurement. Long-term oscillations with about 280s period hampered the effort to get a stable steady state to provide an initial state for the blind benchmark. Oscillations with a higher frequency than sampling rate could be observed, too. The mechanism behind both kinds of oscillations needs further studies to be avoided in future installations.

For now, only the calibration of experimental data with CATHARE has been performed for the steady state. The simulation of the transient with CATHARE needs further work as multiple divergence issues occurred when varying the air temperature and heat exchange coefficient during the calculation. The next step is to model the entire sCO_2 loop. A significant work has to be performed on the turbomachinery modelling in CATHARE. The compressor and the turbine must be added in the loop. The modelling work will require the support of the code development team as the data setting is quite complex and the divergence issues are numerous for this recent application with supercritical CO_2.

The benchmark cycle has been modelled and simulated successfully with the help of ClaRaPlus MODELICA library within Dymola environment. This model includes the UHS, SEH, PP, valves and interconnecting piping. Simulation results for transient benchmark are presented in this report. General agreement between simulation and measurement is observed, but also several shortcomings (e.g. valve modelling, UHS heat transfer coefficient at air side modelling, air mass flow rate calculation) were identified. Elimination of these shortcomings and continuation in modelling of the other still missing components shall be part of the future CVR effort.

With ATHLET the benchmark cycle has also been modelled and simulated successfully. Similar to CATHARE, instability issues were observed, but most of them were solved except the transition to subcritical states close to the critical point. Due to the detailed modelling of the SEH and UHS, the results are in good agreement with the measurements. The remaining deviations might be related to the oscillations in the cycle or to special heat transfer effects close to the critical point. In the future, the modelling and validation efforts must be continued to especially improve the recently developed turbomachinery and compact heat exchanger models.

By the validation of the simulations presented in this deliverable D1.2, the implementation of supercritical CO_2 in the codes ATHLET, CATHARE and MODELICA moved a big step ahead. Therefore, the confidence level for designing and simulating the heat removal cycle for the nuclear power plant is gradually increased and the goals of deliverable D1.2 are attained.

9 References

Austregesilo, H., Bals, C., Hora, A., Lerchl, G., Romstedt, P., Schöffel, P., . . . Weyermann, F. (2016). *ATHLET Models and Methods.* GRS, Garching.

Barre F., B. M. (1990, December). The CATHARE code strategy and assessment. *Nuclear Engineering and Design, 124*(3), 257-284. doi:https://doi.org/10.1016/0029-5493(90)90296-A

Benra, F.-K., Brillert, D., Frybort , O., Hajek, P., Rohde , M., Schuster, S., . . . Starflinger, J. (2016). A supercritical CO2 low temperature Brayton-cycle for residual heat removal. *The 5th International Symposium - Supercritical CO2 Power Cycles.* San Antonio, USA.

Dostal, V., Goettelt, F., Melichar, T., Rohde, M., & Vojacek, A. (2019). Performance test of the air-cooled finned-tube supercritical CO2 sink heat exchanger. *Journal of Thermal Science and Engineering Applications, 11(3)*, pp. 1-11.

Faydide, B., & Rousseau, J. (1980). Two-phase flow modeling with thermal and mechanical non equilibrium. *European Two Phase Flow Group Meeting*. Glasgow.

GFHC. (2018). *Güntner Fluid Cooler.* https://www.guentner.eu/fileadmin/literature/europe/condensers_drycoolers/GFHC/Guentner_GCHC_GCVC_GGHC_GGVC_GFHC_GFVC_Info_EN.pdf.

Guelfi, A., Bestion, D., Boucker, M., Boudier, P., & all. (2007). NEPTUNE: A New Software Platform for Advanced Nuclear Thermal Hydraulics. *Nuclear Science and Engineering, 156*(3), 281-324. doi:https://doi.org/10.13182/NSE05-98

Hacks, A., & Hecker, F. (2019). *Data on behaviour of the sCO2 HeRo loop and the glass model. Deliverable 1.1.*

Hacks, A., Freutel, T., Strätz, M., Vojacek, A., Hecker, F., Starflinger, J., & Brillert, D. (2019). Operational experiences and design of the sCO2-HeRo loop. *3rd European Conference on Supercritical CO2 (sCO2) Power Systems*, (pp. 125-137). Paris, France.

Hofer, M., Buck, M., & Starflinger, J. (2019). ATHLET extensions for the simulation of supercritical carbon dioxide driven power cycles. *Kerntechnik, 84*(5), 390-396.

Hofer, M., Buck, M., Strätz, M., & Starflinger, J. (2019). INVESTIGATION OF A CORRELATION BASED MODEL FOR SCO2 COMPACT HEAT EXCHANGERS. *3rd European supercritical CO2 Conference*, (pp. 1-9). Paris.

IAEA. (2001). *Safety Report on Accident Analysis for Nuclear Power Plants.* Nuclear Energy Agency of the OECD (NEA).

Ishii, M. (1975). *Thermo-fluid dynamic theory of two-phase flow.* Eyrolles.

Kunick, M. (2017). *Fast Calculation of Thermophysical Properties in Extensive Process Simulations with the Spline-Based Table Look-Up Method (SBTL).* VDI, Görlitz.

Lerchl, G., Austregesilo, H., Schöffel, P., von der Cron, D., & Weyermann, F. (March 2016). *ATHLET 3.1A User's Manual.* GRS-P-1/Vol. 1 Rev. 7, Gesellschaft für Anlagen- und Reaktorsicherheit (GRS) gGmbH.

Liu, Y., Wang, H., Zhao, W., Qin, H., & Fang, X. (2016). Thermal-Performance Instability in Piezoresistive Sensors: Inducement and Improvement. *Sensors*.

Mauger, G., Tauveron, N., Bentivoglio, F., & Ruby, A. (2019, February). On the dynamic modeling of Brayton cycle power conversion systems with the CATHARE-3 code. *Energy , 168*, 1002-1016. doi:https://doi.org/10.1016/J.ENERGY.2018.11.063

Miettinen. (2008). Nuclear power plant simulators: Goals and evolution. *Proceedings of seminar on transfer of competence, knowledge and experience gained through CSNI activities in the field of thermal-hydraulics (THICKET),.* Pisa, Italy.

Müller, C. (1991). *Entwicklung schneller Stoffwertpakete zur Beschleunigung des ATHLET-Codes.* GRS, Garching.

National Institute of Standards and Technology,. (s.d.). NIST Standard Reference Database 23, Reference Fluid Thermodynamic and Transport Properties (REFPROP), version 9.0, National Institute of Standards …. Récupéré sur https://pages.nist.gov/REFPROP-docs/

P. Emonot, A. S. (2011, November). CATHARE-3: A new system code for thermal-hydraulics in the context of the NEPTUNE project. *Nuclear Engineering and Design, 241*(11), 4476-4481. doi:https://doi.org/10.1016/j.nucengdes.2011.04.049

Pham, H., Alpy, N., Ferrasse, J., Boutin, O., Tothill, M., Quenaut, J., . . . Saez, M. (2016, 10). An approach for establishing the performance maps of the sc-CO2 compressor: Development and qualification by means of CFD simulations. *International Journal of Heat and Fluid Flow, 61*, 379-394.

Span, R., & Wagner, W. (1996). A new equation of state for carbon dioxide covering the fluid region from the triple-point temperature to 1100 K at pressures up to 800 MPa. *Journal of Physical and Chemical Reference Data, 25*(6), 1509-1596.

Strätz , M., Mertz, R., & Starflinger, J. (2018). Design of a compact heat exchanger and heat transfer investigation of a scaled down sCO2-HeRo system. *International Congress on Advances in Nuclear Power Plants.* Charlotte, USA.

Strätz, M., Starflinger, J., Mertz, R., Seewald, M., Schuster, S., & Brillert, D. (2017). Cycle calculations of a small –scale heat removal system with supercritical CO2 as working fluid. *14th International Conference on Nuclear Engineering.* Shanghai, China.

Theologou, K., Mertz, R., Laurien, E., & Starflinger, J. (2019). An Assessment of the criteria for the onset of heat transfer deterioration with supercritical CO2 in vertical heated sigle circular tubes. *3rd European supercritical CO2 Conference*.

VDI Wärmeatlas. (2013). *VDI Wärmeatlas.* Berlin, Heidelberg,: Springer.

Vojáček, A. (2017). *Delivery of sink HX performance maps.*

Vojáček, A., Dostal, V., Goettelt, F., Rohde, M., & Melichar, T. (2019). Performance Test of the Air-Cooled Finned-Tube Supercritical CO2 Sink Heat Exchanger. *Journal of Thermal Science and Engineering Applications*.

Appendix A Scheme of the glass model with sCO2-HeRo

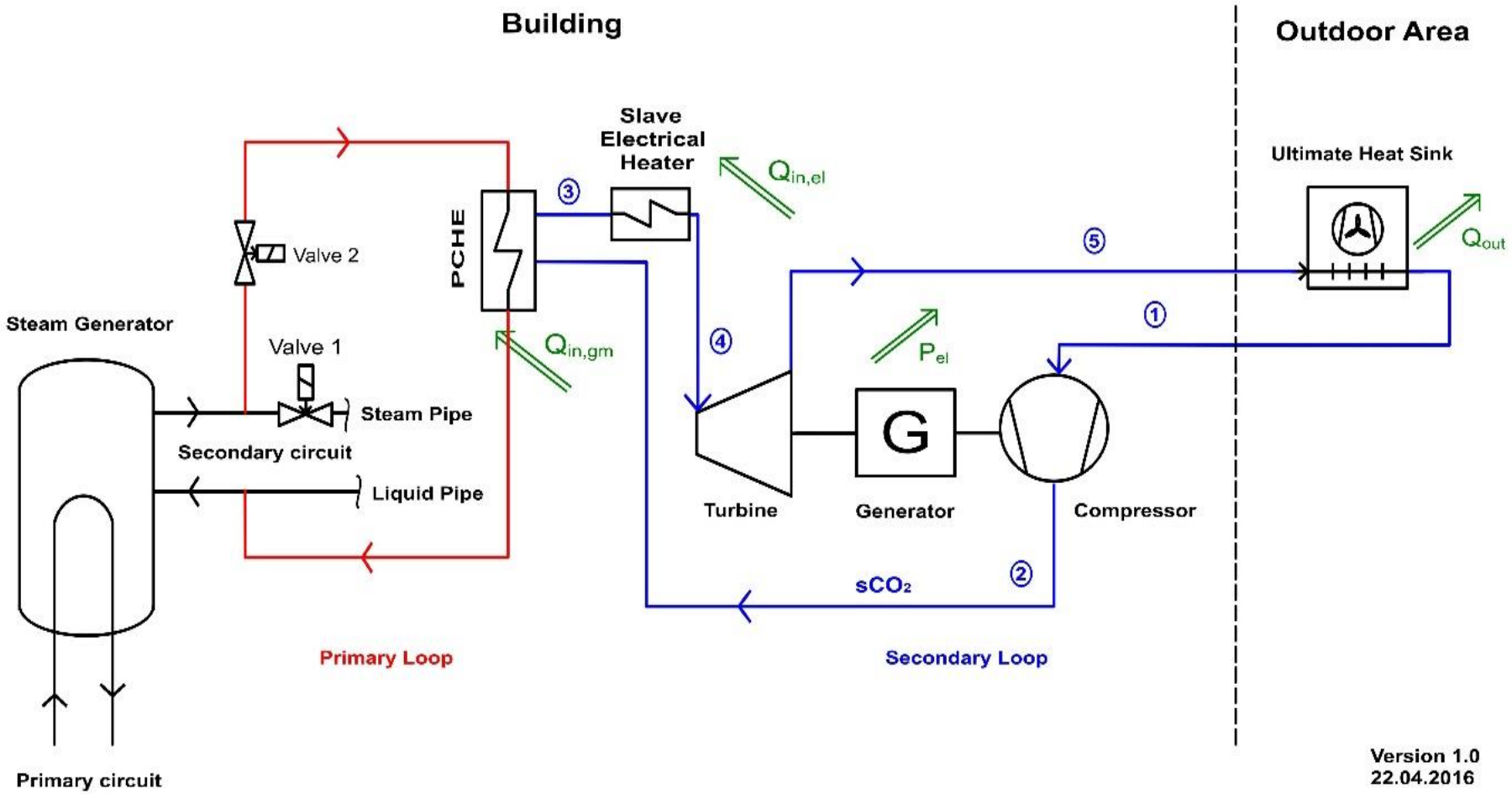

Figure 72 : Scheme of the glass model with sCO2-HeRo (Strätz, et al., 2017)

Appendix B Complete P&I diagram of the HeRo cycle

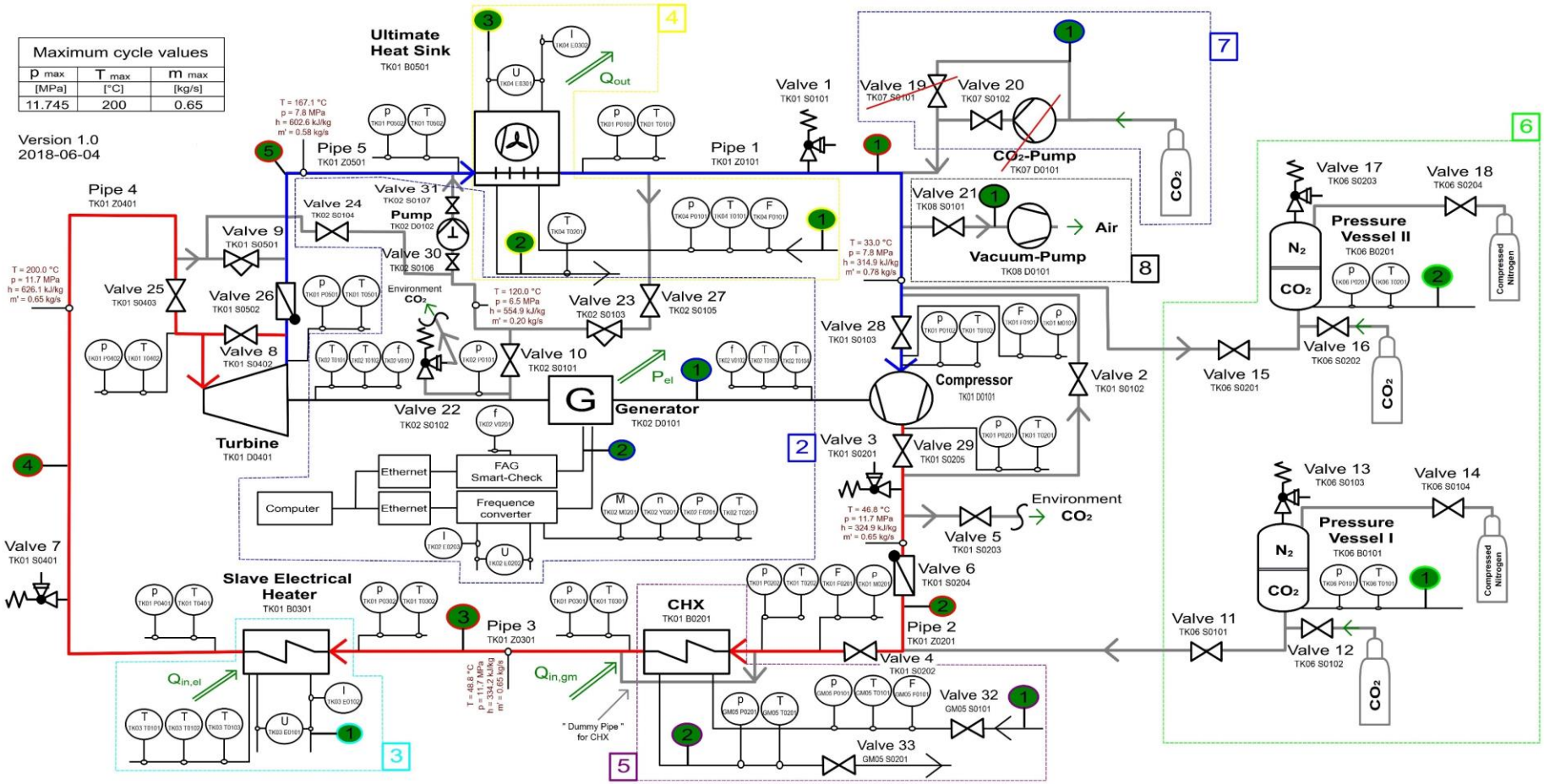

Figure 73 : P&I diagram of the sCO2-HeRo cycle